Fakultät für Maschinenwesen

Lehrstuhl für Aerodynamik und Strömungsmechanik

Smoothed particle hydrodynamics for fluid and solid dynamics

Chi Zhang

Vollständiger Abdruck der von der Fakultät für Maschinenwesen der Technischen Universität München zur Erlangung des akademischen Grades eines

Doktor-Ingenieurs

genehmigten Dissertation.

Vorsitzender:	Prof. Dr.-Ing. Micheal W. Gee
Prüfer der Dissertation:	1. Priv.-Doz. Dr.-Ing. habil. Xiangyu Hu
	2. Prof. Dr.-Ing. Nils Thuerey

Die Dissertation wurde am 16.10.2019 bei der Technischen Universität München eingereicht und durch die Fakultät für Maschinenwesen am 28.01.2020 angenommen.

Declaration of Authorship

I hereby declare that except where specific reference is made to the work of others, the contents of this dissertation are original and have not been submitted in whole or in part for consideration for any other degree or qualification in this, or any other university. This dissertation is my own work and contains nothing which is the outcome of work done in collaboration with others, except as specified in the text and Acknowledgements.

Chi Zhang
October 10, 2019

c.zhang@tum.de

Released October 10, 2019
Typesetting LaTeX

To my parents Zhang Guangxin and Wen Juan, and my wife Ding Yi
To those who inspired it and will not read it *Chi Zhang*

目击众神死亡的草原上野花一片
远在远方的风比远方更远

远方只有在死亡中凝聚野花一片
明月如镜高悬草原映照千年岁月

我的琴声呜咽 泪水全无
只身打马过草原

--海子

Abstract

This cumulative thesis is devoted to the modeling and simulation of fluid and solid dynamics, where violent events such as impact and breaking of free surface or large deformation of structure are involved, using the smoothed particle hydrodynamics (SPH) method. In particular, a low-dissipation weakly-compressible SPH (WCSPH) method based on Riemann solver is developed for free-surface flows, a simple and efficient weighted essentially non-oscillatory (WENO) reconstruction is proposed to increase the accuracy of the proposed method through decreasing numerical dissipation and a generalized transport-velocity formulation is developed to tackle the tensile instability problem of the SPH method.

Simulating time evolution of free-surface flows exhibiting violent events such as impact and breaking is a challenging task due to the complex topology changes, which poses a serious accuracy and efficiency limitation for traditional WCSPH method. The first part of this thesis contributes to developing low-dissipation WCSPH method with significantly improved robustness and accuracy. The key idea is to modify a Riemann solver which determines the particle interaction by a simple limiter to decrease the intrinsic numerical dissipation. Unlike using explicit diffusive terms, the present method regularizes the density profile implicitly by the Riemann solver. In addition, a wall boundary condition based on the one-sided Riemann solver is developed to handle violent breaking-wave impact. To test the robustness and accuracy of the low-dissipative Riemann solver, a number of two and three-dimensional tests, including the Taylor–Green vortex and several dam-break problems, are carried out and the results are compared to analytical and previous results.

The second part of this thesis considers to improve the accuracy of the WCSPH method based on Riemann solver by employing a WENO reconstruction. The key idea is to construct, along each interacting particle pair, a 4-point stencil and to apply a WENO reconstruction for determining the particle interaction with a Riemann solver. The construction is applied to the aforementioned low-dissipation Riemann-based WCSPH method. The proposed WENO construction does not apply multi-dimensional candidate stencils. Rather it operates in a one-dimensional fashion along each interacting particle pair, similarly as that used for monotonic upwind scheme for conservation laws (MUSCL) reconstruction. Several numerical examples on Taylor-Green vortex flow, dam break and non-linear liquid sloshing demonstrate that the method preserves the capability of producing smooth and accurate pressure fields of the original method and now achieves also very small numerical dissipation.

The third part of this thesis aims at eliminating the long-standing issue, e.g., tensile instability, of SPH method. In fluid-dynamics simulations this instability leads to particle clumping and void regions when negative pressure occurs. In solid-dynamics simulations, it results in unphysical structure fragmentation. We proposed a generalized transport-velocity formation for providing a solution of this problem. Other than imposing a global background pressure, a variable background pressure is used to modify the particle transport velocity and eliminate the tensile instability completely. Furthermore, such a modification is localized by defining a

shortened smoothing length. The results of extensive numerical tests on both fluid and solid dynamics problems indicate that the new method provides a unified approach for multi-physics SPH simulations.

Acknowledgements

First and foremost, I would like to express my sincere gratitude to Prof. Nikolaus A. Adams and PD Dr. Xiangyu Hu for their kindness, patience, continuous guidance and suggestions, and warm encouragement during my PhD study. I am very grateful to Xiangyu who has advised this work thoroughly, inspired me with new ideas, and encouraged me when I was frustrated. I greatly appreciate Prof. Adams for providing feedback and inspiring suggestions of study progress through weekly group meeting, for carefully revising our papers. I have been fortunate to benefit from their great visions of research, passions in science, and deep understanding of fluid mechanics.

It is always a pleasure to work with my collaborators in the Chair of Aerodynamics and Fluid Mechanics, Technical University of Munich, including Shucheng Pan, Jianhang Wang, Massoud Rezavand, Lin Fu, Xiuxiu Lyv, Yujie Zhu, Yuxuan Zhagn, Luhui Han, and Ji Zhe. In addition, I truly enjoyed my time as a PhD candidate in this chair, and interact with friendly and talented people here. I wish to extend my gratitude to other members of our chair for their interesting discussions and accompany during my PhD study : Ludger Pähler, Dr. Xin Bian, Dr. Stefan Adami, Zheng Fang, Zhaoguang Wang, Dr. Rongzhong Huang and many others. Particularly, I would like to than staff members in our chair, Angela Grygier, Hua Liu, and Li Su, for their kind services. I am deeply indebted to the Chinese Scholarship Council for providing the financial support of my research in Technical University of Munich.

A very special acknowledgement goes to Prof. Decheng Wan, my master supervisor at Jiaotong University, Shanghai, China. Thank you for convincing me to study computational fluid dynamics, supervising my Master thesis, and being the enlightener of my scientific research.

In the end, I am thoroughly grateful to my parents and my wife to whom I dedicate this dissertation. Without their endless love, encouragement and understanding during my study, this thesis would never has been completed.

Contents

List of Symbols

CFD	computational fluid dynamics
FDM	finite difference method
FEM	finite element method
SPH	smoothed particle hydrodynamics
MPS	moving particle semi-implicit
DEM	discrete element method
$WCSPH$	weakly-compressible SPH
$MLSPH$	moving-least-square SPH
$WENO$	weighted essentially non-oscillatory
$MUSCL$	monotonic upwind scheme for conservation laws
$MOOD$	multidimensional optimal order detection
MLS	moving least squares
EoS	equation of state
dp	particle spacing
h	smoothing length
W	kernel function
t	time
N	number of particles
n	index of time steps
p	pressure
μ	viscosity
δ	Dirac-delta function
ρ	mass density
Δt	time step size
$\mathbf{r}$	location of a particle in the domain
$\mathbf{n}$	normal direction
$\mathbf{u}$	velocity vector
$\mathbf{g}$	gravity vector

Chapter 1

Introduction

1.1 Numerical methods for fluid and solid dynamics

Fluid and solid dynamics problems, in particular those corresponding to free-surface flows where violent impact and breaking events are involved, structure analysis with crack propagation and large deformation, and the coupling of fluid-rigid structure interactions, are often encountered in the areas of science and engineering. Typical examples include wave breaking, wave impact on structure, sloshing phenomena, high-velocity impact and soft material deformation as shown in Fig. 1.1. Numerical simulations of these problems play a valuable role in examinations and demonstrations for theories, offer insights to new physical phenomena and provide assistance in the industrial design [1]. However, computational modeling of these problems is highly challenging due to the intrinsic complexity of topological changes during the surface or interface evolution.

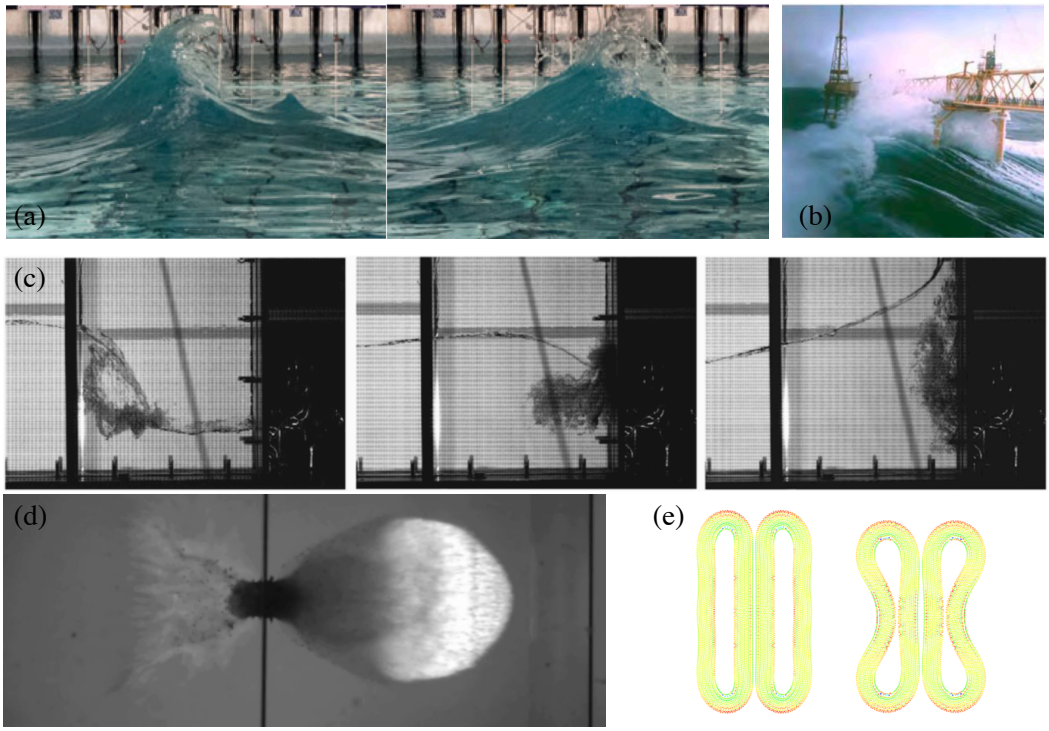

FIGURE 1.1: Typical examples of fluid and solid dynamics : (a) break of Draupner wave (reproduced from Ref. [2]), (b) rogue wave impact on offshore structure (reproduced from Ref. [3]), (c) impact event in sloshing phenomena (reproduced from Ref. [4]), (d) high velocity impact (reproduced from Ref. [5]) and (d) collision of rubber rings with Poisson ratio $\nu = 0.49$ (reproduced from Ref. [6]) .

Mesh-based approaches, such as the Finite Difference Method (FDM) [1] and the Finite Elements Method (FEM) [7], encounter difficulties for simulating the aforementioned applications with complex topological changes. The major issues of mesh-based numerical methods are inherited from the use of mesh, where computational rather expensive process of high quality mesh generation/regeneration is essential. As a consequence, the mesh-based methods encounter difficulties in handling with problems corresponding to wave breaking and impact (for FDM), and large structure deformation (for FEM) which are in the main scope of this thesis.

As an alternative, meshfree methods are expected to be superior to mesh-based FDM and FEM methods, and have received significant interest in the past decades. Meshfree numerical methods, which use a set of arbitrarily distributed particles to represent the computational domain and its boundaries, establish a system of governing equations for the whole problem domain without the use of a predefined mesh. Since no information is required on the relationship between the particles for the interpolation or approximation of the unknown functions of field variables, these methods are attractive in dealing with problems which are difficult for mesh-based methods. Another worth-noting feature of meshfree methods is that it is easy to obtain the time history of the field variables at a given material point as the particle following the moving material point. Also, mesh-free methods have advantage when dealing with multi-physics problems [21] as different materials in a system can be defined by their own sets of particles.

Recently, several meshfree methods, e.g. the smoothed particle hydrodynamics (SPH) method [8, 9], the moving particle semi-implicit method (MPS) [10] and the discrete element method (DEM) [11], are proposed for analyzing fluid and solid dynamics. This thesis will be focusing on the SPH method due to its fully Lagrangian features and well-established theory and fundamentals.

1.2 Review on SPH

As a fully Lagrangian meshfree method, the SPH method has been widely studied as a promising tool in computational modeling of fluid and solid dynamics. The theory, fundamentals and applications are addressed in comprehensive review articles [12, 13, 14]. As the SPH method is the main focus of the present thesis, here we will briefly review the SPH method.

As a meshfree Lagrangian approach, the SPH method was first proposed by Lucy [8] and Gigold and Monaghan [15] for astrophysical applications. In the SPH method, the computational domain is represented by a set of arbitrarily distributed particles and this principle determines its meshfree nature. The partial differential equations (PDE) are expressed in integral form and the integral representation method is used for function approximation which is called kernel approximation. Having the computational domain discretized by particles, the kernel approximation is further approximated, which is known as particle approximation. It is done by replacing the integration in the integral representation, using finite summations over the corresponding values of all neighboring particles in the support domain as shown in Figure 1.2. Here, we refer to Section 2.2 for more details of the theory and fundamentals of the SPH method. The particle approximation is performed every time step, and depends on the local distribution of particles. As the local distribution of particles depends on the nature and the features of the corresponding problem, the SPH method adapts to the simulated problem. As a result, the SPH method is especially suited for problems with large deformations, such as free-surface flows,

complex moving interface and large material deformation, offering a good performance in the problems addressed in this thesis. The SPH method has been success-

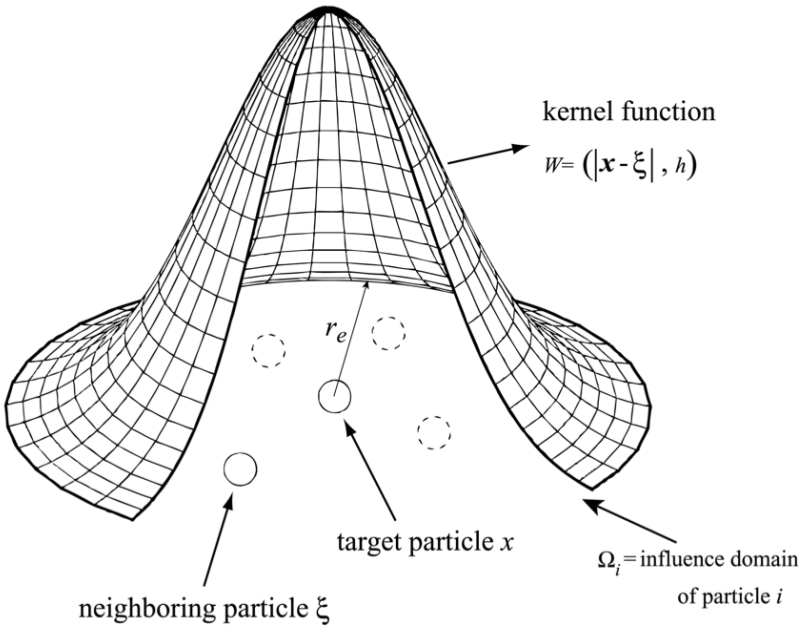

FIGURE 1.2: Particle interaction and the kernel function.

fully extended to a wide range of problems in solid mechanics, e.g. Refs. [16, 17, 18], fluid dynamics, e.g. Refs. [19, 20, 21, 22, 23] and fluid-structure interactions [24]. Many researchers have conducted investigations on the SPH method on the numerical aspects, e.g. accuracy, stability, convergence and efficiency [25].

Despite the aforementioned developments, there are several issues of SPH method to be addressed. Concerning the modeling of fluid dynamics, in particular the free-surface flows where violent events such as impact and breaking are involved, the weakly-compressible SPH (WCSPH) method exhibits spurious pressure oscillations as shown in Figure 1.3 and the inherited numerical instability. A Neumann–Richtmeyer type artificial viscosity has been proposed by Monaghan [26] to dampen the pressure oscillations. However, this explicit artificial viscosity may lead to excessive dissipation which effects the physical flow characteristics. Instead of using the explicit artificial viscosity, the WCSPH method based on Riemann solver introduces implicit numerical dissipation by solving Riemann problem along interacting particles. However, they are generally more dissipative than those based on artificial viscosity. Ferrari [27] proposed to add an artificial diffusion into the continuity equation. Although this method is able to recover violent free-surface flows reasonably, it is not compatible with the hydrostatic solution, which results in unphysical free-surface motion and expansion as shown in Figure 1.4. Another well-known issue of the SPH method is that it suffers from tensile instability. This instability leads to particle clumping in the simulation of fluid dynamics problems, and results in unphysical structure fragmentation in the simulation solid dynamics problems as shown in Figure 1.5.

1.3 Aims and objectives

The fundamental objective of the present thesis is to address the aforementioned issues of the SPH method for fluid and solid dynamics.

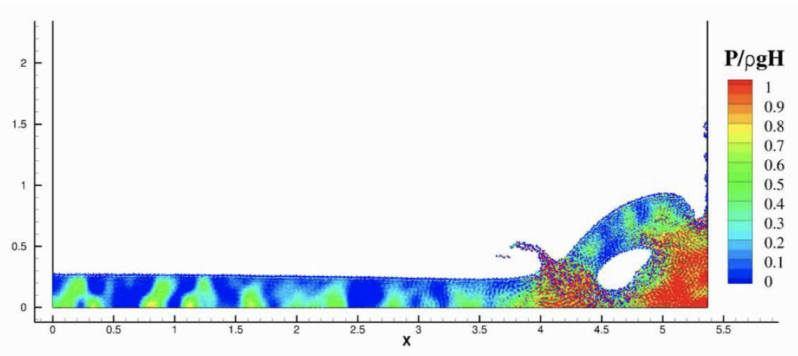

FIGURE 1.3: Pressure oscillations in the simulation of two dimensional dam break flow. Note that the artificial viscosity [26] with $\alpha = 0.01$ is also applied.

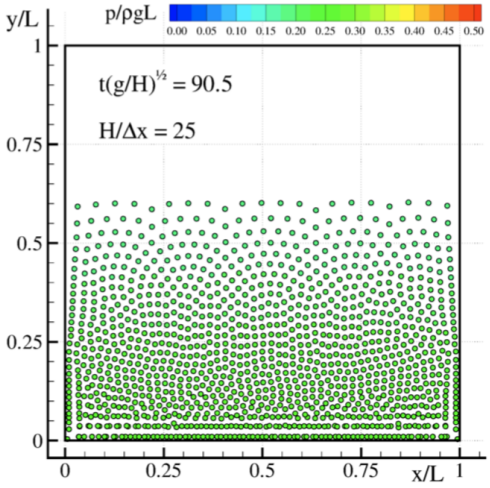

FIGURE 1.4: Hydrostatic test with the artificial diffusion term proposed by Ferrari [27] (Reproduced from Ref. [28]).

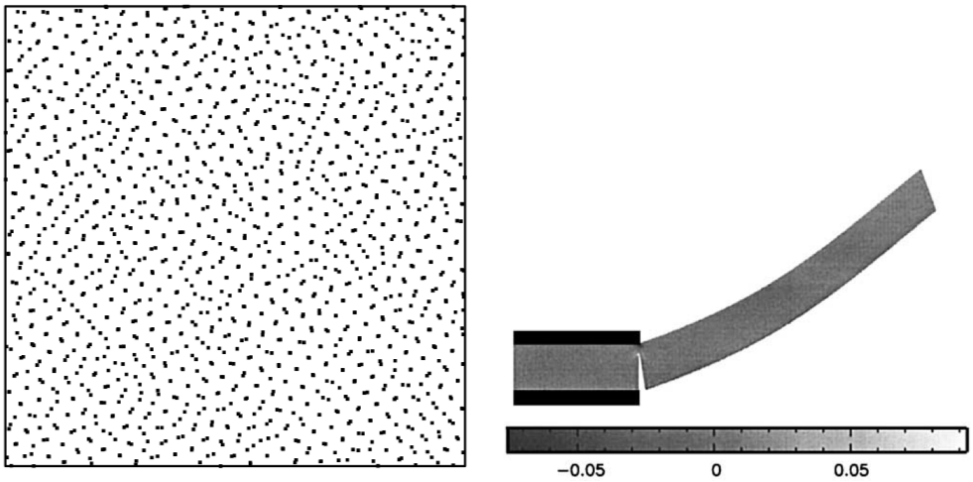

(A) Particle clumping (B) Unphysical fracture

FIGURE 1.5: The tensile instability of SPH method for fluid and solid dynamics (Reproduced from Ref. [17]).

Concerning the simulation of fluid dynamics, in particular the examples exhibit violent events such as impact and breaking, we present a WCSPH method based on a low-dissipation Riemann solver. The key idea is to modify a Riemann solver which determines the interaction between particles by a simple limiter to decrease the intrinsic numerical dissipation. In the proposed method, the modified Riemann solver is also extended for imposing wall boundary conditions. The proposed method is expected to be compatible with hydrostatic solution, and able to resolve the violent free-surface flows with sufficient accuracy. This work is detailed in Paper I [29]

- C. Zhang, X. Y Hu, N. A. Adams, A weakly compressible SPH method based on a low-dissipation Riemann solver. *J. Comput. Phys*. **335**, 605-620, 2017

which has been attached in Appendix A.1.

As the method proposed in Paper I [29] is based on the Godunov's scheme which is a 1st-order construction, therefore, further improvement is expected if a high-order reconstruction scheme is exploited. The next objective is to develop a high-order reconstruction scheme to increase the accuracy of WCSPH method based on Riemann solver by decreasing the numerical dissipation. The key idea is to construct along each interacting particle pair a 4-point stencil and to apply a WENO reconstruction for determining the particle interaction with the proposed low-dissipation Riemann solver [29]. The proposed method achieves second-order accuracy and exhibits very small numerical dissipation. This work is detailed in Paper II [68]

- C. Zhang, G. M. Xiang, B. Wang, Xiangyu Y. Hu, Nikolaus A. Adams, A weakly compressible SPH method with WENO reconstruction. *J. Comput. Phys*. **392**, 1-18, 2019

which is attached in Appendix A.2.

The last but not least objective of the thesis is to address the long-standing problem of the SPH method, e.g., tensile instability. This tensile instability leads to particle clumping and void regions when negative pressure occurs in modeling fluid dynamics, and results in unphysical structure fragmentation in simulating solid dynamics where structures experience large deformation. The transport-velocity formulation of Adami et al. [30] is generalized to provide a solution for this long-standing problem. Other than imposing a global background pressure, a variable background pressure is used to modify the particle transport velocity and eliminate the tensile instability completely. Also, such a modification is localized by defining a shortened smoothing length. The generalized formulation is suitable for fluid and solid materials with and without free surfaces. This work is detailed in Paper III [6]

- C. Zhang, X. Y Hu, N. A. Adams, A generalized transport-velocity formulation for smoothed particle hydrodynamics. *J. Comput. Phys*. **337**, 216-232, 2017

which is attached in Appendix A.3.

1.4 Outline

The following is the structure of the remainder of the present thesis. Chapter 1 provides an introduction to the theory and fundamentals of the SPH method, the SPH discretization of the conservation equations of fluid and solid dynamics, the SPH method based on Riemann solver and the corresponding high-order reconstructions and the generalized transport-velocity formulation. Equation of state and time integration scheme and treatment of wall boundary condition of WCSPH method are

also discussed. Particularly, as detailed in Chapter 3, a low-dissipation WCSPH method based on Riemann solver is proposed, a simple WENO reconstruction is developed to improve the accuracy of WCSPH method based on Riemann solver and a generalized transport-velocity formulation is presented for eliminating the tensile instability. Finally, in Chapter 4 the conclusions are summarized and recommendations for future work are given.

Chapter 2

Governing equations and methods

In this chapter, we briefly summarize the governing equations of fluid and solid dynamics, and introduce the theory and fundamentals of the SPH method. Then the traditional SPH method, the SPH method based on Riemann solver and the corresponding high-order reconstruction and the generalized transport-velocity formulation are reviewed. Finally, the equation of state, the treatment of boundary condition and the time integration of WCSPH are also discussed.

2.1 Governing equations

The governing equations for continuum mechanics in a Lagrangian reference frame include the equations for conservation for mass and momentum. The mass-conservation equation is

$$\frac{\mathrm{d}\rho}{\mathrm{d}t} = -\rho\nabla\cdot\mathbf{v}, \tag{2.1}$$

and the momentum-conservation equation is

$$\frac{\mathrm{d}\mathbf{v}}{\mathrm{d}t} = \frac{1}{\rho}\nabla\cdot\boldsymbol{\sigma} + \mathbf{g}. \tag{2.2}$$

Here, ρ is the density, $\mathbf{v}$ the velocity, t the time, $\mathbf{g}$ the body force, $\boldsymbol{\sigma}$ the stress tensor and

$$\frac{\mathrm{d}(\bullet)}{\mathrm{d}t} = \frac{\partial(\bullet)}{\partial t} + \mathbf{v}\cdot\nabla(\bullet), \tag{2.3}$$

refers to the material derivative. Note that Eqs. (2.1) and (2.2) allow a common description of both fluid and solid dynamics.

For elastic solid materials, the stress tensor $\boldsymbol{\sigma}$ can be decomposed into isotropic and deviatoric parts

$$\boldsymbol{\sigma} = -p\mathbf{I} + \boldsymbol{\sigma}', \tag{2.4}$$

where p is the hydrostatic pressure, $\mathbf{I}$ identity matrix and $\boldsymbol{\sigma}'$ the deviatoric stress. Using Jaumann's formulation of the Hooke's law, the rate of change of the deviatoric stress can be described as

$$\frac{\mathrm{d}\boldsymbol{\sigma}'}{\mathrm{d}t} = 2G(\boldsymbol{\epsilon} - \frac{1}{3}\boldsymbol{\epsilon}\cdot\mathbf{I}) + \boldsymbol{\sigma}'\cdot\boldsymbol{\Omega} + \boldsymbol{\Omega}\cdot\boldsymbol{\sigma}', \tag{2.5}$$

where G is the shear modulus, $\boldsymbol{\epsilon}$ is the strain tensor

$$\boldsymbol{\epsilon} = \frac{1}{2}\Big(\nabla\otimes\mathbf{v} + (\nabla\otimes\mathbf{v})^T\Big), \tag{2.6}$$

and $\mathbf{\Omega}$ is the rotation tensor

$$\mathbf{\Omega} = \frac{1}{2}\Big(\nabla \otimes \mathbf{v} - (\nabla \otimes \mathbf{v})^T\Big). \tag{2.7}$$

For a weakly-compressible or incompressible fluid, the deviatoric stress vanishes and a viscous force is added to the stress tensor:

$$\sigma = -p\mathbf{I} + 2\eta\nu, \tag{2.8}$$

where ν is the dynamic viscosity.

2.2 Theory and fundamentals of the SPH method

Before introducing the discretizations of the governing equations, we first summarize the theory and fundamentals of the SPH method.

2.2.1 Integral interpolation and particle approximation

Using the definition of unconnected and arbitrarily distributed computation points, any quantity can be calculated by the following equation

$$f(\mathbf{r}) = \int_\Omega f(\mathbf{r}^{'})\delta(\mathbf{r} - \mathbf{r}^{'})d\mathbf{r}^{'}, \tag{2.9}$$

where $\mathbf{r}$ is the spatial coordinate, $f(\mathbf{r})$ an arbitrary function of $\mathbf{r}$, $\delta(\mathbf{r} - \mathbf{r}^{'})$ the Dirac delta function and Ω the volume of the integral domain. This integral interpolation re-produces the quantity of $f(\mathbf{r})$ exactly as the Dirac delta function is applied. However, Eq. (2.9) can't be used to establish a discrete model as the Dirac delta function is only supported by a point. Gingold and Monaghan [9] and Lucy [8] defined a kernel approximation of the function f by introducing a smoothing kernel

$$\widehat{f(\mathbf{r})} = \int_\Omega f(\mathbf{r}^{'})W(\mathbf{r} - \mathbf{r}^{'}, h)d\mathbf{r}^{'}, \tag{2.10}$$

where $\widehat{f(\mathbf{r})}$ is the kernel approximation of $f(\mathbf{r})$, W the smoothing kernel with h being the smoothing length which determines the effective width of the smoothing kernel.

If the computational domain is discrete by a set of N particles (points) $\mathbf{r}_1, \mathbf{r}_2, \cdots \mathbf{r}_N$, and the value of $f(\mathbf{r})$ is only known at particles, the approximation of $f(\mathbf{r})$ can be written as

$$f(\mathbf{r}) = \sum_{i=1}^{N} f(\mathbf{r}_i)W(\mathbf{r} - \mathbf{r}_i, h)dV_i, \tag{2.11}$$

where the notation $f(\mathbf{r})$ is used instead of $\widehat{f(\mathbf{r})}$, the index i denotes the particle label and the particle has the mass m and the density ρ at $\mathbf{r}$ position, and dV denotes the differential volume element around the particle. If we use $\frac{m_i}{\rho_i}$ to express the differential volume element dV_i, then the approximation of $f(\mathbf{r})$ can be written as

$$f(\mathbf{r}) = \sum_{i=1}^{N} \frac{m_i}{\rho_i} f(\mathbf{r}_i)W(\mathbf{r} - \mathbf{r}_i, h). \tag{2.12}$$

This summation is over particles which lie within a circle of radius kh centered at particle i with position $\mathbf{r}$ as shown in Figure 2.1.

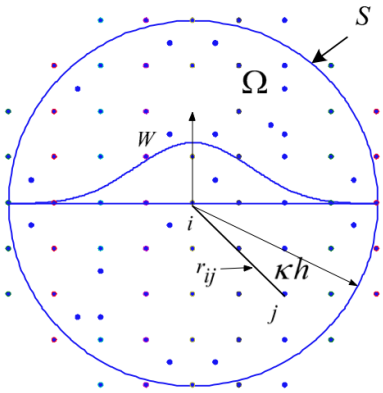

FIGURE 2.1: Sketch of particle approximation of SPH method. Here kh presents the support length of the smoothing kernel W.

Using the SPH kernel approximation defined in (2.10), the gradient of a scalar function f can be rewritten as

$$\bigtriangledown f(\mathbf{r}) = \int_{\Omega} \bigtriangledown f(\mathbf{r}^{'}) W(\mathbf{r}-\mathbf{r}^{'},h) dV(\mathbf{r}^{'}). \tag{2.13}$$

The right hand of Eq. (2.13) can be Integrated by parts, and then applying Gauss theorem gives

$$\bigtriangledown f(\mathbf{r}) = \int_{\partial\Omega} f(\mathbf{r}^{'}) W(\mathbf{r}-\mathbf{r}^{'},h)\mathbf{n} dS(\mathbf{r}^{'}) - \int_{\Omega} f(\mathbf{r}^{'}) \bigtriangledown W(\mathbf{r}-\mathbf{r}^{'},h) dV(\mathbf{r}^{'}), \tag{2.14}$$

where $\partial\Omega$ denotes the domain surface and $\mathbf{n}$ the corresponding outward normal. If we assume that a particle located at $\mathbf{r}$ which is entirely inside the computational domain, for example the distance from the boundary is much larger than the support length kh of the smoothing kernel W, then the first term in the right hand of Eq.(2.14) can be ignored. In this case, the gradient of a function f can be approximated as

$$\bigtriangledown f(\mathbf{r}) = -\int_{\Omega} f(\mathbf{r}^{'}) \bigtriangledown_{\mathbf{r}'} W(\mathbf{r}-\mathbf{r}^{'},h) dV(\mathbf{r}^{'}) \tag{2.15}$$

$$= \int_{\Omega} f(\mathbf{r}^{'}) \bigtriangledown_{\mathbf{r}} W(\mathbf{r}-\mathbf{r}^{'},h) dV(\mathbf{r}^{'}) \tag{2.16}$$

Applying particle approximation, described by Eqs. (2.10 - 2.12), Eq. (2.15) can be rewritten in SPH form as

$$\bigtriangledown f(\mathbf{r}_i) = \sum_{j=1}^{N} \frac{m_j}{\rho_j} f(\mathbf{r}_j) \bigtriangledown_i W(\mathbf{r}_i - \mathbf{r}_j, h). \tag{2.17}$$

where $\nabla_i W(\mathbf{r}_i - \mathbf{r}_j, h) = \nabla_i W_{ij} = \frac{\mathbf{e}_{ij}}{r_{ij}} \frac{\partial W_{ij}}{\partial r_{ij}}$ with $\mathbf{e}_{ij} = \frac{\mathbf{r}_i - \mathbf{r}_j}{|\mathbf{r}_i - \mathbf{r}_j|}$.

Similarly, the SPH approximation of divergence of a vector function $\mathbf{F}(\mathbf{r})$ can be derived as

$$\begin{aligned}
\bigtriangledown \cdot \mathbf{F}(\mathbf{r}) &= \int_{\Omega} [\bigtriangledown_{\mathbf{r}'} \cdot \mathbf{F}(\mathbf{r}')] W(\mathbf{r}-\mathbf{r}', h) dV(\mathbf{r}') \\
&= \int_{\partial\Omega} \mathbf{F}(\mathbf{r}') W(\mathbf{r}-\mathbf{r}', h) \mathbf{n} dS(\mathbf{r}') - \int_{\Omega} \mathbf{F}(\mathbf{r}') \cdot \bigtriangledown W(\mathbf{r}-\mathbf{r}', h) dV(\mathbf{r}') \qquad (2.18) \\
&= -\int_{\Omega} \mathbf{F}(\mathbf{r}') \cdot \bigtriangledown_{\mathbf{r}'} W(\mathbf{r}-\mathbf{r}', h) dV(\mathbf{r}') \\
&= \int_{\Omega} \mathbf{F}(\mathbf{r}') \cdot \bigtriangledown_{\mathbf{r}} W(\mathbf{r}-\mathbf{r}', h) dV(\mathbf{r}') \\
&= \sum_{j=1}^{N} \frac{m_j}{\rho_j} \mathbf{F}(\mathbf{r}_j) \bigtriangledown_i W_{ij}. \qquad (2.19)
\end{aligned}$$

2.2.2 The smoothing kernel

In the SPH method, the smoothing kernel determines consistency and accuracy of kernel and particle approximations. Therefore, it is of utmost importance to choose an appropriate function in SPH simulations. According to Liu and Liu [31] and Monaghan [12], the smoothing kernel must be normalized over its support domain

$$\int_{\Omega} W(\mathbf{r}-\mathbf{r}', h) d\mathbf{r}' = 1, \qquad (2.20)$$

and also should be compactly supported

$$W(\mathbf{r}-\mathbf{r}') = 0, \text{for} |\mathbf{r}-\mathbf{r}'| > kh. \qquad (2.21)$$

Here, k is the smoothing factor, $|\mathbf{r}-\mathbf{r}'| \leq \kappa h$ defines the support domain. Besides, the smoothing kernel must satisfy the symmetry condition which is crucial for the conservation property, and behave as a delta function as the smoothing length approaches zero. We refer to Ref. [32] for more details.

As various smoothing kernels have been proposed for SPH method [15, 33, 34, 12, 32, 31], the most commonly used smoothing kernels are briefly summarized in the following. In the original SPH paper [8], Lucy used a bell-shaped kernel which take the form

$$W(\mathbf{r}-\mathbf{r}', h) = \alpha_d \begin{cases} (1+3q)(1-q)^3 & \text{if } q \leq 1 \\ 0 & \text{if } q > 1 \end{cases}, \qquad (2.22)$$

where $q = |\mathbf{r}-\mathbf{r}'|/h$ and the constant α_d is equal to $5/4h$, $5/\pi h^2$ and $105/16\pi h^3$ in one, two and three dimensions, respectively.

In another original SPH calculation of Gingold and Monaghan [15], the Gaussian kernel was applied to simulate the non-spherical stars and it takes the form

$$W(\mathbf{r}, h) = \alpha_d exp(-q^2), \qquad (2.23)$$

where α_d is equal to $1/\pi^{1/2}h$, $1/\pi h^2$ and $1/\pi^{3/2}h^3$ in one, two or three dimensions, respectively. The Gaussian kernel is sufficiently smooth even for high orders of derivatives and regards as a "gold" selection since it is very stable and accurate especially for disordered particles. However, the interpolation of the Gaussian kernel extends across the entire computation domain due to the fact that it does not have

a compact support. In the fact, the relative contribution from neighboring particles quickly become negligible as the distance increase. Therefore, this disadvantage makes it a poor choice for practical applications [35].

Monaghan and Lattanzio [33] proposed the cubic spline kernel, which has similar shape with Gaussian kernel but with compact support, to improve the computational efficiency. This cubic spline kernel reads

$$W(\mathbf{r}-\mathbf{r}^{'},h)=\alpha_d\begin{cases}\frac{2}{3}-q^2+\frac{1}{2}q^3 & \text{if } 0\leq q\leq 1\\ \frac{1}{6}(2-q)^3 & \text{if } 1\leq q\leq 2\\ 0 & \text{if } 2\leq q\end{cases}, \tag{2.24}$$

where α_d is equal to $1/h$, $15/7\pi h^2$ and $3/2\pi h^3$, in one, two and three dimensional space, respectively. As it resembles a Gaussian kernel while having a narrow compact support, the cubic spline kernel has been widely used in the SPH literatures. However, this kernel may leads to the so-called tensile instability.

Wendland [36] proposed a class of smoothing kernels for SPH method to address the issue of particle clustering and numerical instability. A fifth-order Wendland kernel reads

$$W(\mathbf{r}-\mathbf{r}^{'},h)=\alpha_d\begin{cases}(1+2q)(2-q)^4 & \text{if } 0\leq q\leq 2\\ 0 & \text{if } 2\leq q\end{cases}, \tag{2.25}$$

where the constant α_d is equal to $7/64\pi h^2$ and $21/256\pi h^3$ in two or three dimensions, respectively.

2.3 SPH method for fluid and solid dynamics

In this part, the SPH method will be implemented for hydrodynamics and the appropriate discretized form of the governing equations of fluid and solid dynamics will be derived.

2.3.1 The continuity equation

Using the summation equation given by Eq. (2.12), the SPH calculation of density for particle can be derived straightforwardly as [14]

$$\rho_i=\sum_{j=1}^{N}m_jW_{ij}, \tag{2.26}$$

where $W_{ij}=W(\mathbf{r}_{ij},h)$. The density summation equation shows good performance when dealing with the problems involve two or more fluids with large density ratio [37]. Alternatively, the density can be evaluated from its rate of change in time. Following the work of Monaghan [12], the continuity equation can be written as

$$\frac{d\rho}{dt}=-\rho\bigtriangledown\cdot\mathbf{v}. \tag{2.27}$$

Using the Divergence theorem, the $\bigtriangledown\cdot\mathbf{v}$ term in the right hand of Eq. (2.27) can be re-written as

$$\bigtriangledown\cdot\mathbf{v}=\frac{1}{\Phi}[\bigtriangledown\cdot(\Phi\mathbf{v})-\mathbf{v}\cdot\bigtriangledown\Phi]. \tag{2.28}$$

Following Ref. [34], Substituting Eq. (2.28) into Eq. (2.27) with the assumption $\Phi = 1$ gives

$$\frac{d\rho}{dt} = -\rho[\bigtriangledown \cdot (\mathbf{v}) - \mathbf{v} \cdot \bigtriangledown 1]. \tag{2.29}$$

Using the previous SPH approximations, we have

$$\frac{d\rho_i}{dt} = \rho_i \sum_{j=1}^{N} \frac{m_j}{\rho_j} (\mathbf{v}_i - \mathbf{v}_j) \cdot \bigtriangledown_i W_{ij}. \tag{2.30}$$

Eq. (2.30) has been widely used in the simulation of free-surface flows where violent events such as impact and breaking are involved.

2.3.2 The momentum equation

The SPH discretization of the momentum equation can be derived by using Lagangian mechanics. For the non-dissipative motion of a fluid without considering potential, the Lagrangian L is defined as [38]

$$L = \int (\frac{1}{2}\rho|\mathbf{v}|^2 - \rho e) d\mathbf{r}, \tag{2.31}$$

where e is the internal energy. Following the work of Monaghan [39, 12], the SPH form of Eckart's Lagrangian can be re-written as

$$L = \sum_{j=1}^{N} m_j \left[\frac{1}{2}|\mathbf{v}|^2 - e(\rho)\right]. \tag{2.32}$$

For particle i, the Lagrange's equation satisfies

$$\frac{d}{dt}\left(\frac{\partial L}{\partial \mathbf{v}_i}\right) - \frac{\partial L}{\partial \mathbf{r}_i} = 0. \tag{2.33}$$

Then we can find

$$\frac{\partial L}{\partial \mathbf{r}_i} = \sum_{j=1}^{N} \left(\frac{\partial e(\rho_j)}{\partial \rho_j}\right) \frac{\delta \rho_j}{\delta \mathbf{r}_i}, \tag{2.34}$$

where δ is the change of the Lagrangian. Following first law of thermodynamics with the assumption of no heat exchange, we have

$$\frac{de}{d\rho} = \frac{p}{\rho^2}. \tag{2.35}$$

By differentiating the SPH summation of density Eq. (2.26), we have

$$\delta\rho_j = \rho_j \sum_{k=1}^{N} \frac{m_k}{\rho_k} (\delta\mathbf{r}_j - \delta\mathbf{r}_k) \bigtriangledown_j W_{jk}. \tag{2.36}$$

By using the Kronecker delta δ_{ij} which is 1 if $i = j$ and zero otherwise, Eq. (2.36) can be rewritten as

$$\frac{\delta\rho_j}{\delta\mathbf{r}_i} = \rho_j \sum_{k=1}^{N} \frac{m_k}{\rho_k} (\delta_{ji} - \delta_{ki}) \bigtriangledown_j W_{jk}. \tag{2.37}$$

Substituting Eq. (2.37) into Eq. (2.34) gives

$$\begin{aligned} m_i \frac{d\mathbf{v}_i}{dt} &= -\sum_j \sum_k \frac{m_j m_k}{\rho_j \rho_k} p_j (\delta_{ji} - \delta_{ki}) \bigtriangledown_j W_{jk} \\ &= -\frac{m_i}{\rho_i} \left(p_i \sum_k \frac{m_k}{\rho_k} \bigtriangledown_i W_{ki} + p_j \sum_j \frac{m_j}{\rho_j} \bigtriangledown_j W_{ji} \right) \end{aligned} \tag{2.38}$$

Then Eq. (2.38) can be re-written as [12]

$$\frac{d\mathbf{v}_i}{dt} = -\sum_{j=1}^{N} m_j \left(\frac{p_i + p_j}{\rho_i \rho_j} \right) \bigtriangledown_i W_{ij}. \tag{2.39}$$

If a viscous fluid is taken into account, the viscous terms could be estimated directly using the SPH approximation as [12]

$$\Pi_{ij} = -\frac{\zeta \mu}{\rho_i \rho_j} \frac{\mathbf{v}_{ij} \cdot \mathbf{r}_{ij}}{r_{ij}^2}, \tag{2.40}$$

where Π_{ij} represents the viscous force between interacting particles, μ the dynamic viscosity and ζ an arbitrary positive parameter. Hu and Adams [40] proposed that $\zeta = d + 2$ with d denotes the spatial dimension. Then, the momentum equation of a viscous fluid can be written as

$$\frac{d\mathbf{v}_i}{dt} = -\sum_{j=1}^{N} m_j \left(\frac{p_i + p_j}{\rho_i \rho_j} + \Pi_{ij} \right) \bigtriangledown_a W_{ab}. \tag{2.41}$$

Accordingly, the momentum-conservation equation for an elastic solid can be derived as [41, 42]

$$\frac{\mathrm{d}\mathbf{v}_a}{dt} = -\sum_b m_b \left[\left(\frac{p_a + p_b}{\rho_a \rho_b} \right) \mathbf{I} - \left(\frac{\boldsymbol{\sigma}'_a + \boldsymbol{\sigma}'_b}{\rho_a \rho_b} \right) \right] \bigtriangledown_i W_{ij} + \mathbf{g}_a. \tag{2.42}$$

Here, subscripts a and b are sued for denoting the solid particles.

2.4 SPH method based on Riemann solver

Different from the aforementioned traditional SPH discretizations, the SPH method based on Riemann solver introduces a Riemann problem to determines the particle interaction. The advantage of this method is that no explicit artificial viscosity is used and the numerical dissipation is introduced implicitly. Another worth noting feature is that a high-order reconstruction, e.g. Monotonic Upwind Scheme for Conservation Laws (MUSCL) and Weighted Essentially Non-Oscillatory (WENO), may be applied.

2.4.1 Baseline scheme

The SPH method based on Riemann solver can be derived by constructing an inter-particle Riemann problem alonging a unit vector $\mathbf{e}_{ij} = -\mathbf{r}_{ij}/r_{ij}$ pointing form particle i to particle j, as shown in Fig. 2.2. In this Riemann problem the initial left and right states are on particles i and j, respectively, and the discontinuity is at the

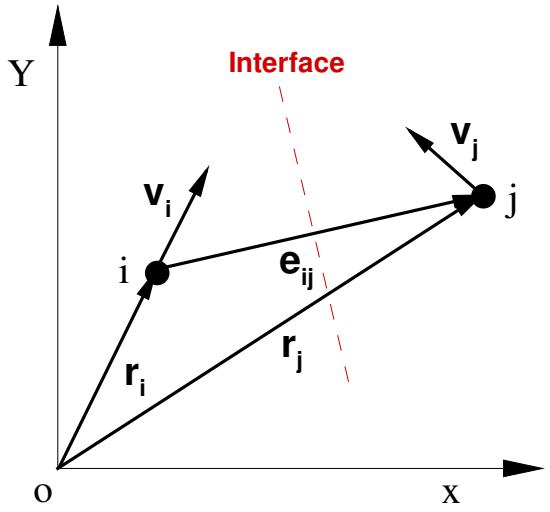

FIGURE 2.2: Construction of Riemann problem along the interacting line of particles i and j.

middle point $\bar{\mathbf{r}}_{ij} = \frac{1}{2}(\mathbf{r}_i + \mathbf{r}_j)$. The L and R states are

$$\begin{cases} (\rho_L, U_L, P_L) = (\rho_i, \mathbf{v}_i \cdot \mathbf{e}_{ij}, p_i) \\ (\rho_R, U_R, P_R) = (\rho_j, \mathbf{v}_j \cdot \mathbf{e}_{ij}, p_j) \end{cases} . \tag{2.43}$$

It is worth noting that such a Riemann problem is based on a piece-wise constant assumption, i.e. 1st-order reconstruction (denoted as "Baseline" scheme).

The solution of the Riemann problem results in three waves emanating from the discontinuity [44], as shown in Fig. 2.3. Two waves, which can be shock or rar-

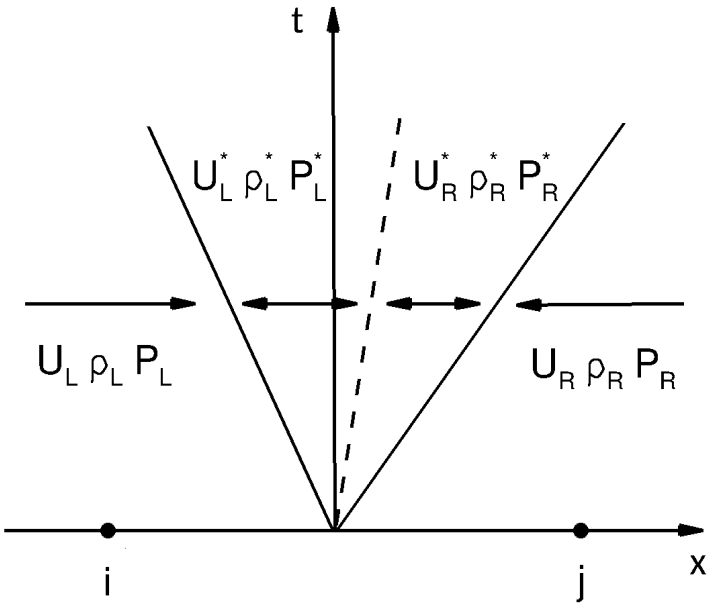

FIGURE 2.3: Simplified Riemann fan with two intermediate states.

efaction wave, traveling with the smallest or largest wave speed. The middle wave

is always a contact discontinuity and separates two intermediate states, denoted by (ρ_L^*, U_L^*, P_L^*) and (ρ_R^*, U_R^*, P_R^*). By assuming that the intermediate state satisfies $U_L^* = U_R^* = U^*$ and $P_L^* = P_R^* = P^*$, a linearised Riemann solver [44] for smooth flows or with only moderately strong shocks can be written as

$$\begin{cases} U^* = \overline{U} + \frac{1}{2}\frac{(P_L - P_R)}{\bar{\rho} c_0} \\ P^* = \overline{P} + \frac{1}{2}\bar{\rho} c_0 (U_L - U_R) \end{cases}, \tag{2.44}$$

where $\overline{U} = (U_L + U_R)/2$ and $\overline{P} = (P_L + P_R)/2$ are inter-particle averages. With the solution of the Riemann problem, i.e. U^* and P^*, the discretization of the SPH method is

$$\frac{d\rho_i}{dt} = 2\rho_i \sum_j \frac{m_j}{\rho_j} (\mathbf{v}_i - \mathbf{v}^*) \cdot \nabla_i W_{ij}, \tag{2.45}$$

$$\frac{d\mathbf{v}_i}{dt} = -2 \sum_j m_j \left(\frac{P^*}{\rho_i \rho_j} \right) \nabla_i W_{ij}, \tag{2.46}$$

where $\mathbf{v}^* = U^* \mathbf{e}_{ij} + (\overline{\mathbf{v}}_{ij} - \overline{U} \mathbf{e}_{ij})$. This indicates that the inter-particle average velocity and pressure in Eqs. (2.30) and (2.41) are simply replaced by the solution of the Riemann problem. By comparing both it can be seen that the intermediate velocity and pressure in Eq. (2.44) from the inter-particle averages amount to implicit dissipation, i.e. density regularization and numerical viscosity, respectively.

2.4.2 MUSCL reconstruction

The Baseline scheme can be modified by adopting a MUSCL reconstruction with a slope limiter according to Total Variational Diminishing (TVD) constraint. Introducing the the MUSCL reconstruction [45], the left and right states of the Riemann problem in Baseline scheme are reconstructed from

$$\begin{array}{l} \Phi_L = \Phi_i + \frac{1}{2}\overline{\Delta\Phi_i} \\ \Phi_R = \Phi_j - \frac{1}{2}\overline{\Delta\Phi_j} \end{array}, \tag{2.47}$$

where $\overline{\Delta\Phi_i}$ and $\overline{\Delta\Phi_j}$ are limited slopes. In a typical SPH formulation [46] the limited slopes are defined as

$$\overline{\Delta\Phi_i}, \overline{\Delta\Phi_j} = \begin{cases} max[0, min(\beta\Delta\Phi_i, \Delta\Phi_j), min(\Delta\Phi_i, \beta\Delta\Phi_j)], \Delta\Phi_j > 0 \\ max[0, min(\beta\Delta\Phi_i, \Delta\Phi_j), min(\Delta\Phi_i, \beta\Delta\Phi_j)], \Delta\Phi_j < 0 \end{cases}, \tag{2.48}$$

where

$$\begin{cases} \Delta\Phi_i = \bigtriangledown\Phi_i \cdot \mathbf{r}_{ji} \\ \Delta\Phi_j = \bigtriangledown\Phi_j \cdot \mathbf{r}_{ij} \end{cases} \text{ and } \quad \beta = 1.5. \tag{2.49}$$

Note that many other slope limiters, e.g. Minmod, Superbee, Sweby, which are widely used in Eulerian mesh method [45] , may be applied. For example, Iwasaki et al. [47] and Murante et al. [48] use a van Leer slop limiter for modeling compressible MHD flow problems.

2.4.3 A WENO-based reconstruction

The WENO reconstruction has been widely used in Eulerian Godunov-method to achieve higher accuracy and less numerical dissipation. For this reason, we apply

a WENO reconstruction to the SPH method based on Riemann solver to increase accuracy through decreasing numerical dissipation. Based on the concept inherited from the schemes in Refs. [49, 50], a modified WENO reconstruction, by which the full 4-point stencil (4 points with indices from -1 to 2 as shown in Fig. 2.4), is constructed from a set of small stencils with incremental size.

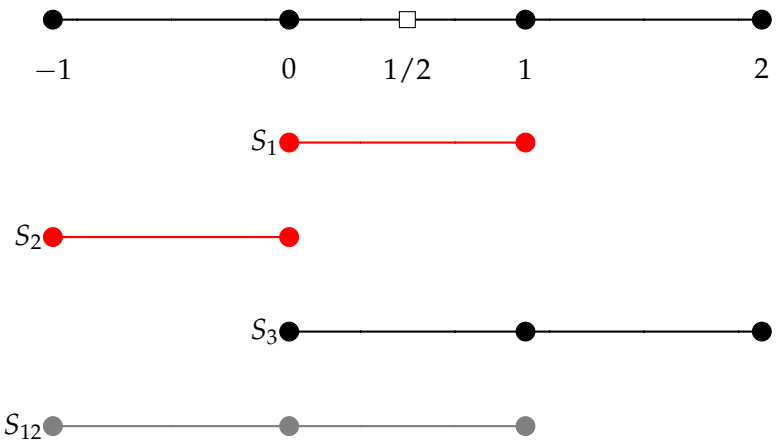

FIGURE 2.4: Full stencil and candidate stencils, i.e. $S_k, k = 1, 2, 3$, for the incremental-stencil WENO reconstruction of $q_{1/2}$. Note that S_1 and S_2 are subsets of the original stencil S_{12} for WENO-JS reconstruction [51].

In the present reconstruction, the mid-point value, i.e. $q_{1/2}$, is predicted by the non-linear weighted average

$$q_{1/2} = \sum_k w_k q_{1/2}^{(k)}, \tag{2.50}$$

where $q_{1/2}^{(k)}$ and w_k, $k = 1, 2, 3$, are the reconstructed values from the candidate stencils and their non-linear weights. These reconstructed values are

$$\begin{cases} q_{1/2}^{(1)} = \frac{1}{2}q_0 + \frac{1}{2}q_1 \\ q_{1/2}^{(2)} = -\frac{1}{2}q_{-1} + \frac{3}{2}q_0 \\ q_{1/2}^{(3)} = \frac{1}{3}q_0 + \frac{5}{6}q_1 - \frac{1}{6}q_2 \end{cases} . \tag{2.51}$$

Following Wang et al. [50], the non-linear weights are defined as

$$w_k = \frac{\alpha_k}{\sum_{s=1}^{3}\alpha_s}, \begin{cases} \alpha_1 = d_1\left(1 + \frac{\tau_4}{\beta_1+\varepsilon}\cdot\frac{\tau_4}{\beta_{12}+\varepsilon}\right) \\ \alpha_2 = d_2\left(1 + \frac{\tau_4}{\beta_2+\varepsilon}\cdot\frac{\tau_4}{\beta_{12}+\varepsilon}\right) \\ \alpha_3 = d_3\left(1 + \frac{\tau_4}{\beta_3+\varepsilon}\right) \end{cases} , \tag{2.52}$$

where the linear weights are determined as $d_1 = 1/3$, $d_2 = 1/6$ and $d_3 = 1/2$. β_k, $k = 1, 2, 3$, and β_{12} are the smoothness indicators for the candidate stencils,

$$\begin{cases} \beta_1 = (q_1 - q_0)^2 \\ \beta_2 = (q_0 - q_{-1})^2 \\ \beta_{12} = \frac{1}{4}(q_{-1} - q_1)^2 + \frac{13}{12}(3q_{-1} - 2q_0 + q_1)^2 \\ \beta_3 = \frac{13}{12}(q_0 - 2q_1 + q_2)^2 + \frac{1}{4}(3q_0 - 4q_1 + q_2)^2 \end{cases}, \tag{2.53}$$

$\varepsilon = 10^{-6}$ as in WENO-JS, and τ_4 is a global reference smoothness indicator [49] given as

$$\begin{aligned} \tau_4 = [q_{-1}(547q_{-1} - 2522q_0 + 1922q_1 - 494q_2) \\ + q_0(3423q_0 - 5966q_1 + 1602q_2) \\ + q_1(2843q_1 - 1642q_2) \\ + 267q_2]\ /240. \end{aligned} \tag{2.54}$$

To implement the modified WENO reconstruction into the SPH method based on Riemann solver, the 4-point stencil for interacting particle pair, such as particle i and j, can be constructed. For particle i, the values at the stencil points are calculated as

$$\begin{cases} q_{-1} = \Phi_i - \nabla\Phi_i \cdot \boldsymbol{r}_{ij} \\ q_0 = \Phi_i \\ q_1 = \Phi_j \\ q_2 = \Phi_j + \nabla\Phi_j \cdot \boldsymbol{r}_{ij} \end{cases}, \tag{2.55}$$

where Φ_i and Φ_j represent the primitive values, ρ, P and $\boldsymbol{v} \cdot \mathbf{e}_{ij}$, at particle i and j respectively. Note that $\nabla\Phi_i$ and $\nabla\Phi_j$ are the corresponding gradients calculated from the SPH approximation as

$$\nabla\Phi_i = \sum_j \frac{m_j}{\rho_j}(\Phi_j - \Phi_i)\nabla_i W_{ij}. \tag{2.56}$$

The left state Φ_L of the Riemann problem for the interacting particle pair of i and j is defined as

$$\Phi_L = q_{1/2}, \tag{2.57}$$

by applying Eq. 2.50 based on the 4-point stencil calculated as Eq. 2.55. The right state Φ_R is also obtained from by Eq. 2.50, but based on the mirrored stencil given by

$$\begin{cases} q_{-1} = \Phi_j + \nabla\Phi_j \cdot \boldsymbol{r}_{ij} \\ q_0 = \Phi_j \\ q_1 = \Phi_i \\ q_2 = \Phi_i - \nabla\Phi_i \cdot \boldsymbol{r}_{ij} \end{cases}. \tag{2.58}$$

2.5 Generalized particle transport velocity

With the transport-velocity formulation [30] the momentum velocity for particle transport is modified, and we can redefine the material derivative of a particle moving with the transport velocity $\widetilde{\mathbf{v}}$ as

$$\frac{\widetilde{d}(\bullet)}{dt} = \frac{\partial(\bullet)}{\partial t} + \widetilde{\mathbf{v}} \cdot \nabla(\bullet). \tag{2.59}$$

The mass-conservation equation for a Lagrangian particle is modified accordingly to

$$\frac{\widetilde{d}\rho}{dt} = -\rho \nabla \cdot \widetilde{\mathbf{v}} \tag{2.60}$$

and the momentum equation to

$$\frac{\widetilde{d}\mathbf{v}}{dt} = \frac{1}{\rho}\nabla \cdot \sigma + \frac{1}{\rho}\nabla \cdot \mathbf{A} + \mathbf{g}, \tag{2.61}$$

where the extra stress tensor $\mathbf{A} = \rho \mathbf{v} \otimes (\widetilde{\mathbf{v}} - \mathbf{v})$ is a consequence of the modified transport velocity.

In Adami et al. [30], instead of the momentum velocity the transport velocity $\widetilde{\mathbf{v}}$ is used for particle transport

$$\frac{d\mathbf{r}_a}{dt} = \widetilde{\mathbf{v}}_a. \tag{2.62}$$

The transport velocity at every time step is obtained by modifying the momentum velocity, i.e. ,

$$\widetilde{\mathbf{v}}_a(t+\delta t) = \mathbf{v}_a(t) + \delta t \left(\frac{\widetilde{d}\mathbf{v}_a}{dt} - \frac{1}{\rho_a}\nabla p^0 \right), \tag{2.63}$$

where the term $\frac{1}{\rho_a}\nabla p^0$ is discretized as

$$\frac{1}{\rho_a}\nabla p^0 = p^0 \sum_b m_b \left(\frac{1}{\rho_a^2} + \frac{1}{\rho_b^2} \right) \frac{\partial W_{ab}}{\partial r_{ab}} \mathbf{e}_{ab} = \left(\frac{d\mathbf{v}_a}{dt} \right)_c, \tag{2.64}$$

where p^0 in Adami et al. [30] is a globally constant background pressure whose exact gradient vanishes. In SPH, however, the conservative approximation of the gradient for constant background pressure results in a residual force due to the lack of zero-order consistency. This residual force leads to a self-relaxation mechanism which regularizes the particle distribution such that they assume approximately a configuration with low consistency error [52].

If we consider the right-hand-side of Eq. (2.64) as a general correction of the particle acceleration such that $\left(\frac{d\mathbf{v}_a}{dt} \right)_c$ is proportional to p^0, we are free to choose different p^0 for different particles, or a different influence radius of such a correction. In this paper, we propose to modify Eq. (2.64) as

$$\left(\frac{d\mathbf{v}_a}{dt} \right)_c = p_a^0 \sum_b m_b \frac{1}{\rho_a^2} \frac{\partial \widetilde{W}_{ab}}{\partial r_{ab}} \mathbf{e}_{ab}, \tag{2.65}$$

where $\widetilde{W}_{ab} = W(\mathbf{r}_{ab}, \widetilde{h})$ and $\widetilde{h} = 0.5h$, which indicates that only the nearest-neighbor particles within the distance $2\widetilde{h}$ affect the correction. Here, p_a^0 is chosen as

$$p_a^0 = \min(10|p_a|, p_{ref}), \tag{2.66}$$

where p_{ref} is a reference pressure to avoid excessive time-step size limitation. For a weakly-compressible fluid or solid, $p_{ref} = K$. For compressible fluid or solid, $p_{ref} = \max(|p|_{\max}, K)$, where $|p|_{\max}$ is the maximum pressure magnitude in the entire domain. While Eq. (2.65) implies that the correction is proportional to the local particle pressure, it also implies that there is no, or only a very slight correction for a particle near a free fluid or solid material surface due to the surface boundary condition. Note that the factor of $|p_a|$ in Eq. (2.66) and the size of $\widetilde{h}$ in $\widetilde{W}_{ab}$ may affect the correction effectiveness. By preliminary numerical tests we found that the parameters of 10 and $0.5h$ are generally suitable.

2.6 Weakly-compressible SPH method

2.6.1 Equation of state

To close the system of conservation equations, one further relation is required for pressure. In the WCSPH method [43], the material is assumed to be weakly compressible and an appropriate equation of state (EoS) is used to link the pressure with the density. The most common EoS used in WCSPH takes the form [19]

$$p = \rho_0 c^2 [(\frac{\rho}{\rho_0}) - 1], \tag{2.67}$$

where ρ_0 is the reference density.

For fluid dynamics, the speed of sound should be

$$c = 10 V_{max} \tag{2.68}$$

where V_{max} is the anticipated maximum velocity inside the flow to ensure incompressibility in the liquid. For solid dynamics, the sound speed is calculated by

$$c = \sqrt{\frac{E}{3(1-2\nu)\rho_0}} \tag{2.69}$$

where E is the Young's modulus and ν the Poisson ratio.

2.6.2 Wall boundary treatment

Treating the wall-boundary conditions is one of most challenging parts of the WCSPH method and many different approaches have been developed [53, 23]. In the following we briefly summarize three techniques proposed in the literature for the treatment of wall-boundary condition.

1. Ghost particle technique as shown in Figure 2.5 (a) has been widely used in particle methods to impose different boundary conditions. By using artificial particles with prescribed physical quantities (such as pressure and velocity), one fills the empty area of the kernel support in the boundary. The ghost particle method shows advantage in preventing nonphysical behavior. However,

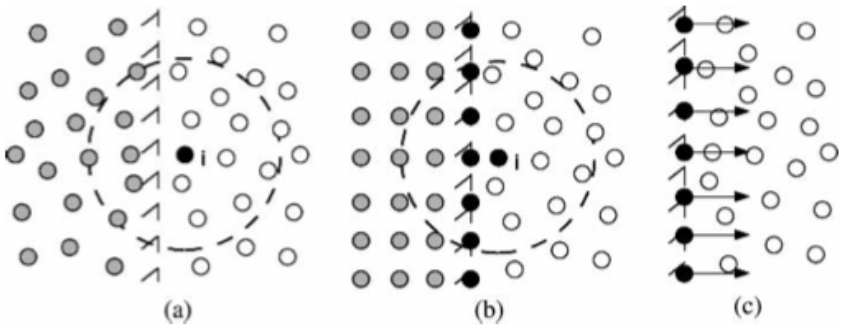

FIGURE 2.5: Solid boundary treatment: (a) ghost particles, (b) dummy particles, (c) repulsive force

the positioning of ghost particles can be hard to implement in three dimensional complex geometries.

2. The dummy particle method has been developed by Adami et al. [23]. In this method, the boundaries are represented by several layers of fixed particles with the same spacing as the initial fluid particles to ensure the convolution of the nearby fluid particles as shown in Figure 2.5 (b). The dummy particles are governed by the same continuity and momentum equations as the fluid particles.

3. Monaghan and Kajtar [53] proposed to use one single layer fixed particles, which interact with the fluid particles through radial forces, to imposed solid wall boundary condition as shown in Figure 2.5 (c). This method is easy to implement for complex boundary geometries and computationally cheap. However, this treatment is impossible to maintain particles stationary in hydrostatic condition.

In addition to the three broad categories of boundary treatment, some new boundary treatments have been developed , such as, the unified semi analytical boundary condition [54].

As for the WCSPH method based on Riemann solver, the interaction between an fluid particle and a wall particle is determined by solving a one-sided Riemann problem [55] along the wall-normal direction.

In the one-sided Riemann problem the left state is defined from the fluid particle corresponding to the local boundary normal,

$$(\rho_L, U_L, P_L) = (\rho_f, -\mathbf{n}_w \cdot \mathbf{v}_f, P_f) \tag{2.70}$$

where the subscript f represents the fluid particles, $\mathbf{n}_w$ is the local wall-normal direction as shown in Fig. 2.6. According to the physical wall boundary condition the right-state velocity U_R is assumed as

$$U_R = -U_L + 2u_w, \tag{2.71}$$

where u_w is the wall velocity. Similarly to Adami et al. [23] the right-state pressure is assumed as

$$P_R = P_L + \rho_f \mathbf{g} \cdot \mathbf{r}_{fw}, \tag{2.72}$$

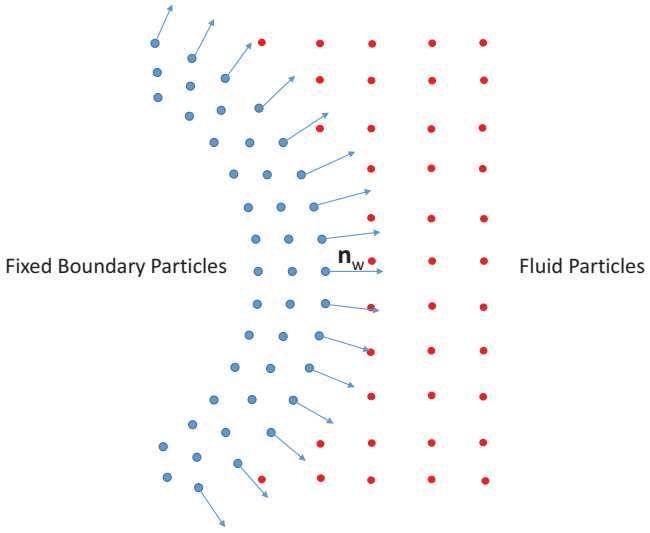

FIGURE 2.6: Sketch of fluid particles interacting with fixed wall boundary particles along the wall normal direction through the one-side Riemann problem.

where $\mathbf{g}$ is the gravity force, $\mathbf{r}_{fw} = \mathbf{r}_w - \mathbf{r}_f$, and the right-state density is obtained by applying the artificial equation of state. Note that, unlike Adami et al. [23], since the Riemann problem is solved in a particle-by-particle fashion no interpolation of states for the wall particles is required. The wall normal direction is calculated for each wall particle by

$$\mathbf{n}_w = \frac{\mathbf{\Phi}(\mathbf{r}_i)}{|\mathbf{\Phi}(\mathbf{r}_i)|}, \quad \mathbf{\Phi}(\mathbf{r}_i) = -\sum_{j \in w} \frac{m_j}{\rho_j} \bigtriangledown W_{ij}, \tag{2.73}$$

where the summation is over wall particles only. A more accurate calculation would be to apply the reproducing-kernel correction [18, 56]. For problems with static walls $\mathbf{n}_w$ is pre-computed before the numerical simulation. If there is a moving wall the wall-normal direction should be updated according to its rotation.

2.6.3 Time integration

Any stable time integrating algorithm for ordinary differential equations can be used to integrate the WCSPH sets of governing equations. Similarly to Adami et al. [30], the kick-drift-kick scheme [12] is used for time integration in this thesis. First the momentum velocity and transport velocity are calculated at the half time step,

$$\mathbf{v}^{n+\frac{1}{2}} = \mathbf{v}^n + \frac{\Delta t}{2}\left(\frac{\widetilde{d}\mathbf{v}}{dt}\right)^n, \tag{2.74}$$

$$\widetilde{\mathbf{v}}^{n+\frac{1}{2}} = \mathbf{v}^{n+\frac{1}{2}} + \frac{\Delta t}{2}\left(\frac{d\mathbf{v}}{dt}\right)_c^n. \tag{2.75}$$

Then the time derivatives of density and deviatoric stresses for solid dynamics are calculated using the transport velocity. The new time step density, deviatoric stresses

and particle position are updated by

$$\rho^{n+1} = \rho^n + \Delta t \left(\frac{\widetilde{d}\rho}{dt} \right)^{n+\frac{1}{2}}, \tag{2.76}$$

$$\sigma'^{n+1} = \sigma'^n + \Delta t \left(\frac{\widetilde{d}\sigma'}{dt} \right)^{n+\frac{1}{2}}, \tag{2.77}$$

$$\mathbf{r}^{n+1} = \mathbf{r}^n + \Delta t \widetilde{\mathbf{v}}^{n+\frac{1}{2}}. \tag{2.78}$$

Finally, at new time-step particle position, the momentum velocity is updated

$$\mathbf{v}^{n+1} = \mathbf{v}^{n+\frac{1}{2}} + \frac{\Delta t}{2} \left(\frac{\widetilde{d}\mathbf{v}}{dt} \right)^{n+1}. \tag{2.79}$$

Note that if the transport velocity is not applied, $\widetilde{\mathbf{v}}^{n+\frac{1}{2}}$ equals to $\mathbf{v}^{n+\frac{1}{2}}$ and the present time integration will resolve the traditional counterpart.

For numerical stability several time step criteria should be satisfied, including the CFL condition

$$\Delta t \leq 0.25 \left(\frac{h}{c + |U|} \right), \tag{2.80}$$

where $|U|$ is the maximum velocity magnitude, the viscous condition

$$\Delta t \leq 0.25 \left(\frac{h^2}{\nu} \right), \tag{2.81}$$

and the body-force condition

$$\Delta t \leq 0.25 \sqrt{h/g}. \tag{2.82}$$

For solid dynamics, the elastic stress condition is

$$\Delta t \leq 0.25 \left(\frac{h}{\sqrt{\frac{E}{\rho_0}} + |U|} \right), \tag{2.83}$$

where E denotes the Young's modulus.

2.7 Summary

In this chapter, the fundamentals and theoretical aspects of the SPH method were presented. The integral interpolation and particle approximation were introduced. The traditional SPH discretizations of the continuity and the momentum equation of fluid and solid dynamics were presented. The SPH based on Riemann solver and the corresponding high-order reconstruction, namely MUSCL and WENO, were briefly summarized. Also, the equation of state, the treatment of wall boundary conditions and time integration of WCSPH were discussed.

Chapter 3

Summaries of publications

In this chapter, the relevant publications of this thesis are briefly summarized.

3.1 A weakly compressible SPH method based on a low dissipation Riemann solver

C. Zhang, X. Y. Hu and N.A. Adams

3.1.1 Summary of the publication

In modeling fluid dynamics, in particular free-surface flows involving breaking and impact events, the WCSPH method exhibits spurious pressure oscillations, which may lead to numerical instability [43, 28], due to the fact that the pressure is evaluated through density by using an artificial equation of state.

In this paper, we propose a WCSPH method based on a low-dissipation Riemann solver for simulating violent free-surface flows. The key idea is to modify a Riemann solver which determines the interaction between particles by introducing a simple limiter to decrease the intrinsic numerical dissipation other than applying the classic Riemann solvers directly [57, 58, 59, 60].

We propose to limit the intermediate pressure in Eq. (2.44) as

$$P^* = \overline{P} + \frac{1}{2}\beta\overline{\rho}(U_L - U_R), \tag{3.1}$$

where the limiter is defined as

$$\beta = \min\left(\eta \max(U_L - U_R, 0), \overline{c}\right). \tag{3.2}$$

The present limiter ensure that zero and decreased numerical dissipation for expansion and compression waves, respectively. Unlike using explicit diffusive terms as in Refs. [27, 61], the present method regularizes the density profile implicitly by the Riemann solver. In addition, a wall boundary condition based on the one-sided Riemann solver is developed to handle violent breaking-wave impact. Several numerical examples, e.g. Taylor-Green vortex, hydrostatic test and three-dimensional dam-break problem involving violent free-surface breaking and impacting, are used to validate the present method. The hydrostatic test, as shown in Figure 3.1, shows that the proposed method is compatible with the hydrostatic solution which ensures the numerical stability in long-time simulations. The low-dissipation feature of the present method is validated by comparing the dissipation of mechanical energy of two-dimensional dam break flow with the numerical results of Marrone et al. [62]

with δ-SPH method. Extensive numerical examples shown that without tuning parameters the method is able to resolve violent wave breaking and impact events accurately, produces smooth pressure field and predicts reasonable pressure peaks.

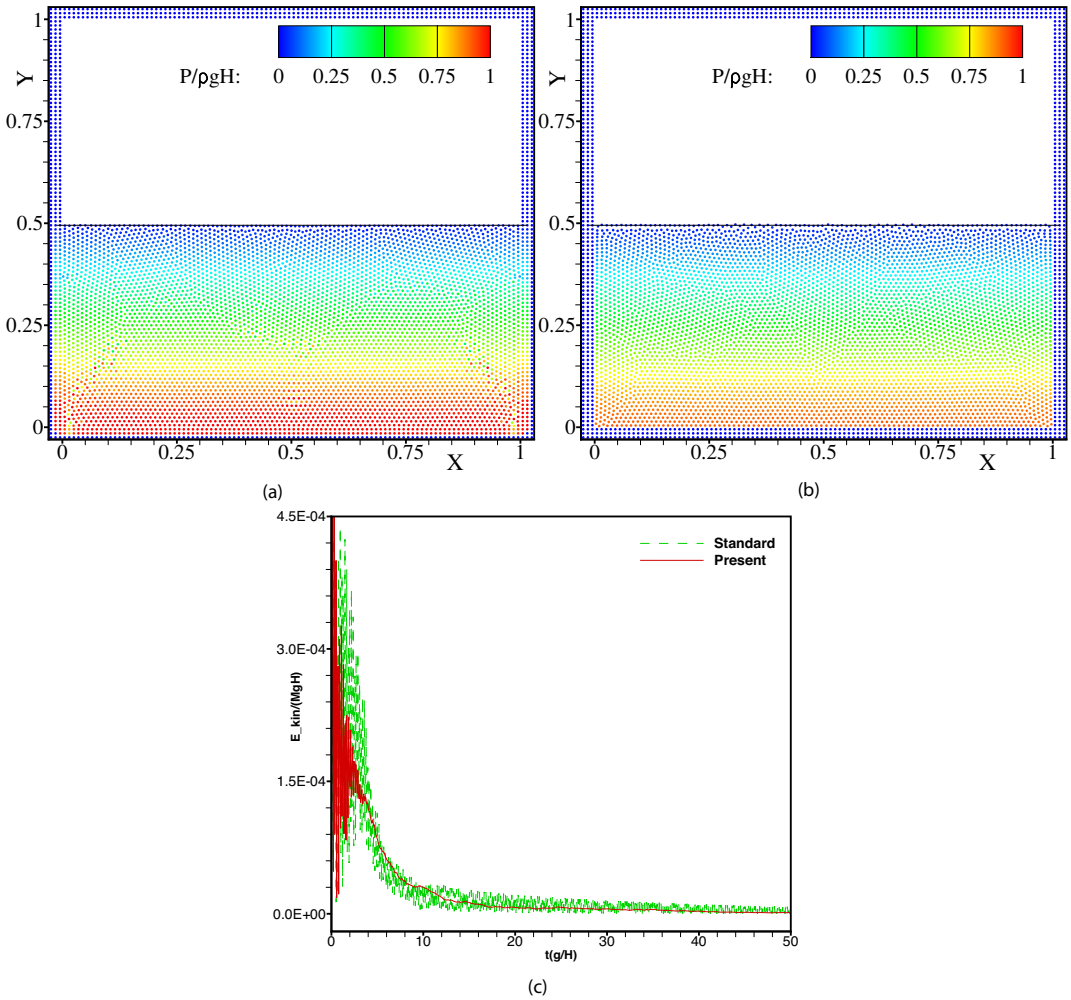

FIGURE 3.1: The hydrostatic test where the initial free surface is denoted by solid line.The standard WCSPH method with artificial viscosity term (a), the present method (b) and the evolution of kinetic energy (c).

3.1.2 Individual contributions of the candidate

This article [29] was published in the international peer-reviewed journal *journal of computational physics*. My contribution to this work was the development of the method and the corresponding computer code for its implementation. I have performed simulations, analyzed the results, and wrote the manuscript for the publication.

3.2 A weakly compressible SPH method with WENO reconstruction

C. Zhang, G.M. Xiang, B. Wang, X. Y. Hu and N.A. Adams

3.2.1 Summary of the publication

The proposed WCSPH method based on low-dissipation Riemann solver [29] has shown good performance in modeling free-surface flows. It is noted that the Riemann solver is based on a 1st-order construction only. Therefore, the application of higher-order reconstruction may lead to even less numerical dissipation.

High-order reconstruction, such as weighted essentially non-oscillatory (WENO), used in Eulerian Godunov-method is able to achieve higher accuracy and less numerical dissipation [63]. The first WENO reconstruction for computing multi-dimensional problems is proposed by Avesani et al. [65], in which the directionally-biased multi-dimensional candidate stencils with high-order Moving-Least-Squares (MLS) reconstructions are combined with the WENO weighting strategy. Although this method achieves higher accuracy than those using linear reconstructions, it exhibits much lower computational efficiency due to a large number of multi-dimensional candidate-stencil evaluations.

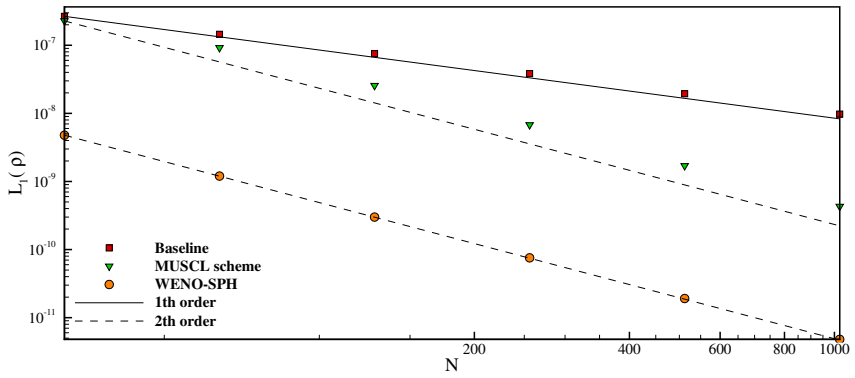

FIGURE 3.2: One dimensional acoustic wave: the convergence of the density error as a function of particle resolution.

In this paper we proposed a simple and computationally efficient WENO reconstruction to increase accuracy and to decrease numerical dissipation for multi-dimensional WCSPH simulation of hydrodynamic problems. Similarly to Avesani et al. [65], the main objective of applying the WENO reconstruction here is to increase accuracy by decreasing the numerical dissipation other than increasing the formal approximation order of the SPH method, which depends on many factors and is quite difficult to achieve in practice. It is shown that a general SPH method applying Gaussian-like kernel achieves only 2nd-order convergence even when the integration error is sufficiently small [34, 67]. The construction is applied to the low-dissipation Riemann solver of Paper I. [29]. The proposed WENO construction does not apply multi-dimensional candidate stencils [65]. Rather it operates in a one-dimensional fashion along each interacting particle pair, similarly as that used for MUSCL reconstructions [57]. As shown in Figure 3.2, numerical simulation of one dimensional acoustic wave demonstrates that the proposed method exhibits considerably smaller errors due to less numerical dissipation compared with Baseline wich achieves first-order convergence only and MUSCL reconstruction. Also, numerical

simulations of violent free-surface flows shown that the proposed method exhibits considerably less numerical dissipation of mechanical energy while maintains robustness and efficiency.

3.2.2 Individual contributions of the candidate

This article [68] was published in the international peer-reviewed journal *journal of computational physics*. My contribution to this work was the development of the method and the corresponding computer code for its implementation. I have performed simulations, analyzed the results, and wrote the manuscript for the publication.

3.3 A generalized transport-velocity formulation for smoothed particle hydrodynamics

C. Zhang, X. Y. Hu and N.A. Adams

3.3.1 Summary of the publication

The SPH method suffers from tensile instability. In fluid-dynamics simulations this instability leads to particle clumping and void regions when negative pressure occurs. In solid-dynamics simulations, it results in unphysical structure fragmentation as shown in Figure 3.3.

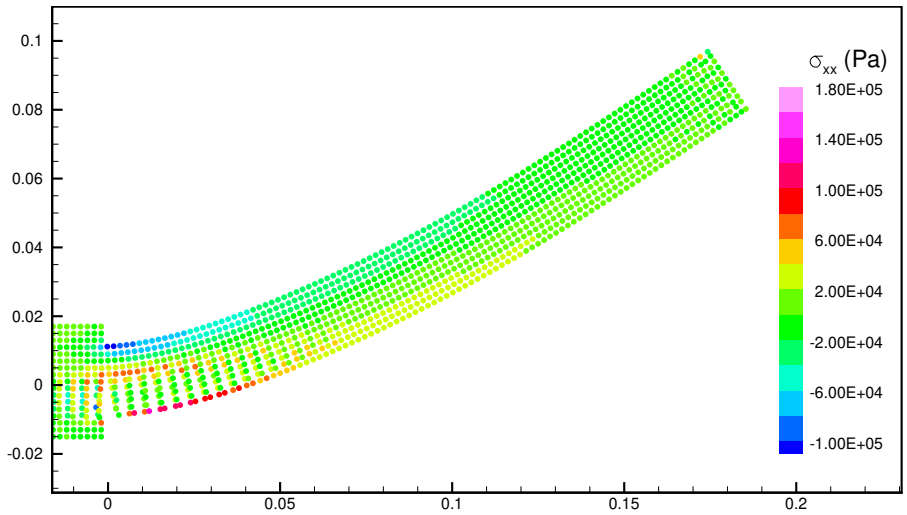

FIGURE 3.3: Unphysical structure fragmentation in the simulation of the oscillating plate using standard SPH method.

In this paper, we extend the transport-velocity formulation proposed by Adami et al. [30] to address the tensile-instability problem for accurate modeling of solid and fluid dynamic problems. Instead of using a globally constant background pressure the present method uses a variable background pressure for the transport velocity correction. According to this modification the correction is proportional to the local pressure and can be implemented to problems with free fluid or solid material surfaces. Additionally, the background pressure correction is localized by involving only nearest-neighbor particles due to a shortened smoothing length. Extensive numerical examples, including free-surface flow, elastic–solid dynamics, high-velocity impact and Taylor–Green vortex flow, are studied to demonstrate effectiveness of the proposed method for eliminating the tensile instability. By reproducing the simulation of the Taylor-Green vortex, the present method preserves the accuracy of the original transport-velocity formulation. Furthermore, numerical results of both fluid and solid dynamics problems show that the present method generally eliminates the tensile instability. In particular, the proposed method has shown good performance in modeling solid dynamics where material has high Poisson ratio as shown in Figure 3.4. Generality and stability of the present method suggest that it has the potential to supersede current standard SPH method.

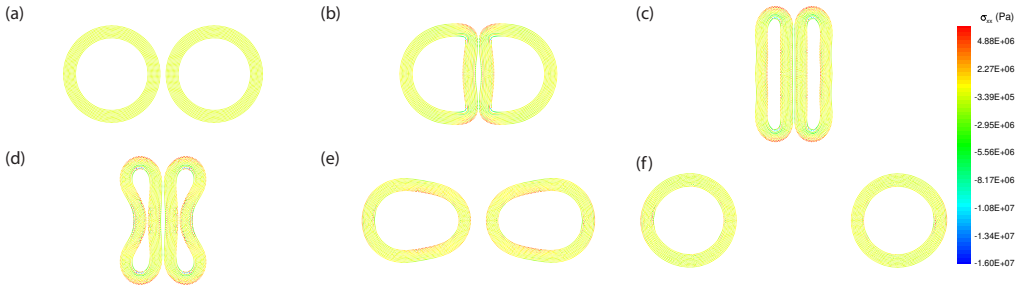

FIGURE 3.4: Collision of rubber rings with Poisson ratio $\nu = 0.49$ using the present method and particles are coloured by σ_{xx} stress field: (a) $t = 0.0s$,(b) $t = 0.03s$, (c) $t = 0.12s$,(d) $t = 0.19s$,(e), $t = 0.25s$, (f) $t = 0.34s$.

3.3.2 Individual contributions of the candidate

This article [6] was published in the international peer-reviewed journal *journal of computational physics*. My contribution to this work was the development of the method and the corresponding computer code for its implementation. I have performed simulations, analyzed the results, and wrote the manuscript for the publication.

Chapter 4

Discussion and outlook

The motivation behind this thesis was three–fold: to develop an accurate and robust WCSPH method based on Riemann solver for modeling free-surface flows where violent breaking and impact events are involved, to improve the accuracy of the proposed method by exploiting WENO reconstruction scheme, and to derive a generalized transport-velocity formulation for SPH to address the tensile instability problem. These objectives have been accomplished successfully by exploiting the proposed methods to several applications. Here, I wrap–up this thesis with discussions and remarks regarding future research.

4.1 Discussions

To dampen the pressure oscillations of WCSPH method in simulating violent free-surface flows, a wide range of numerical approaches have been proposed in the literature. Monaghan and Gingold [26] proposed an Neumann-Richtmeyer type artificial viscosity term in the momentum equation. While a moderate artificial viscosity is able to stabilize the computation, it may lead to excessive dissipation which affects the physical flow characteristics. Colagrossi and Landrini [37] suggested to use a Mean Least Squares (MLS) interpolation to filter the density field. This approach gives good results while is computationally rather expensive [28]. Vila [57] and Moussa [58] developed a SPH method based on solving a Riemann problem along interacting particles. The advantage of this method is that no explicit artificial viscosity is used and the numerical dissipation is introduced implicitly [57, 58]. Unfortunately, this method is very dissipative even when an exact Riemann solver is applied [27]. Similar ideas of enhancing numerical stability using Riemann solvers are also proposed in Refs. [9, 59, 60]. While these methods have been applied to solve shock tube problems [69], solid mechanics problems [60], interface instability [70, 71] and Magnetohydrodynamics (MHD) [47] problems, they are generally more dissipative than those based on artificial viscosity, and do not reproduce violent free-surface flows reliably.

In Paper I, we have proposed a WCSPH method based on a low-dissipation Riemann solver for modeling free-surface flows. To reduce the intrinsic numerical dissipation of the Riemann solver, a simple limiter is proposed and a wall-boundary condition by applying one-sided Riemann problem is also developed. Compared with the previous numerical approaches [27], the proposed method is compatible with the hydrostatic solution. This is an important feature to ensure the numerical stability in long-time simulations which are common countered in engineering applications, for example in the study of wave-structure interactions. Another worth noting feature of the proposed method is that it exhibits considerably less numerical damping of the mechanical energy. This feature is validated by comparison with the

result given by Marrone et al. [62] with δ-SPH method. Several numerical examples, where violent free-surface flows and fluid-solid interactions are involved, are investigated by the proposed method. Numerical results shown that without tuning parameters the present method is able to resolve violent wave breaking and impact events accurately, produces smooth pressure fields and predicts reasonable pressure peaks. In summary, the proposed method has shown comprising potential in the simulation of engineering applications where free-surface flows are involved.

One notable feature of the SPH method based on Riemann solver is that it can apply high-order reconstruction for further improvement. For example, Vila [57] proposed a weighted particle method based on the well-known techniques of Monotonic Upwind Scheme for Conservation Laws (MUSCL) developed by Van Leer [72]. More recently, several innovative efforts have been devoted to developed a high-order SPH method based on weighted essentially non-oscillatory (WENO) reconstruction. Avesani et al. [65] proposed a class of MLS-WENO-SPH methods where the directionally-biased multi-dimensional candidate stencils with high-order MLS reconstructions are combined with the WENO weighting strategy.

Different from the work of Avesani et al. [65], the main objective of Paper II is to develop a modified WENO reconstruction to improve the accuracy of the method developed in Paper I through decreasing the numerical dissipation. The proposed WENO reconstruction is based on the concept inherited from the schemes in Ref. [50]. A 4-point stencils is constructed from a set of small stencils with incremental size. Different from Ref. [50], the minimum-size stencil here has 2 points and the full stencil 4 points in the proposed WENO reconstruction. Using the proposed modified WENO reconstruction, the physical variables are reconstructed for inter-particle Riemann problem which determines the interaction of particles. Compared with the work of Avesani et al. [65], the proposed method is simple and easy for implementation in both 2D and 3D. Also, to the best knowledge of the author, this is the first time that WENO scheme is adopted in WCSPH method for free-surface flows. The numerical results of one dimensional acoustic wave shown that the proposed method is able to achieve second-order convergence. This is reasonable due to the fact that second order is the formal accuracy of a general SPH method with Gaussian-like smoothing kernels when the particle integration error is negligible. Compared with the results obtained with a MUSCL reconstruction, the proposed method exhibits considerably smaller errors due to less numerical dissipation. Also, the present method is applied for simulation of violent free-surface flows, namely dam-break flow, non-linear liquid sloshing and dam-break flow impact on a sharp-edged obstacle. Extensive numerical examples shown that the proposed method looks promising in achieving considerably less numerical damping of mechanical energy, and meanwhile maintains the feature of predicting the pressure peak reasonably.

To tackle the tensile instability of the SPH method, several attempts have been carried out to address this problem since its first observation. Schussler and Schmitt [73] proposed a new kernel function which can produce a repulsive force when negative pressure occurs. However, this function does not satisfy the requirement of continuous first-order derivatives. Jonson and Beissel [74] used a modified non-zero quadratic kernel function to reduce this instability. The problem of this kernel is that it does not have a continuous second-order derivative. Randles and Libersky [18] used a conservative smoothing approach to add stabilizing dissipation for removing the tensile instability. Mandell et al. [75] commented that this approach is good in some cases but only qualitatively correct in other cases. Dilts [76] proposed

MLS particle hydrodynamics (MLSPH) method which replaces the SPH approximation with MLS formulation to reduce tensile instability. While MLSPH is not locally conservative, it increases substantially computational cost compared with standard SPH. Dyka et al. [77] developed a stress-point algorithm which uses stress points located in the mid-way between particles to calculate the stress and maps it to SPH particles. Randles and Libersky [78] showed that this algorithm is stable but complex and computationally inefficient. Since SPH is a particle-based numerical method, a straightforward concept is to eliminate tensile instability by mimicking atomic forces rather than changing the kernel function [17]. Monaghan [16] and Gray et al. [17] developed an artificial stress algorithm to prevent particle clumping and successfully simulated the cases of an oscillating plate and colliding rubber rings. However, as pointed out by Lobovsky and Kren [79], this algorithm fails when the material has comparably high Poisson ratio. Adami et al. [30] proposed a transport-velocity formulation to address particle clumping and void-region problems in WCSPH simulations of high Reynolds number flows. With the original transport-velocity formulation [30], the momentum equation is reformulated by moving particles with a transport velocity [22, 80]. Using a globally constant background pressure for regulation, the transport velocity leads to favorable particle distribution and reduces numerical error [52]. A problem of the original transport-velocity formulation is that there is no straightforward applicability to problems with fluid or solid material free surfaces. This is due to the fact that a constant correcting background pressure may introduce a large artificial velocity at such boundaries.

In Paper III, we have proposed a generalized transport-velocity formulation to address the tensile instability of SPH method. Compared with the original one [30], the proposed generalized formulation implies that the correction is proportional to the local particle pressure, it also implies that there is no, or only a very slight correction for a particle near a free fluid or solid material surface due to the surface boundary condition. By reproducing the simulation of the Taylor-Green vortex flow, the present formulation preserves the accuracy of the original one. Furthermore, the proposed method demonstrates that it generally eliminates the tensile instability for both fluid and solid dynamics. For example, in the simulation of oscillating elastic plate and colliding rubber rings, where large structure deformations are experienced, no unphysical structure fragmentation is observed. Compared with the artificial stress algorithm [17], the proposed method has good performance in the simulation of problem where material has considerable high Poisson ratio, e.g. $\nu = 0.49$. For some challenge simulations, e.g. high-velocity impact and interaction involving realistic rubber material, the robustness and accuracy of the present method are also validated. Again, generality and stability of the present method suggest that it has the potential to supersede the current standard SPH method.

4.2 Outlooks

The present work can be further improved in several directions and some of them are related to both numerical features and physical modeling. Several possibilities for future work are :

- The present generalized transport-velocity formulation suggests that it has the potential to supersede current standard SPH method. Therefore, it is of great benefit to understand whether present method can be extended to simulate compressible flow. Furthermore, the numerical results have shown that

the present method can be employed for modeling fluid-structure interaction problems straightforwardly.

- The proposed WCSPH method based on a low-dissipation Riemann solver is based on particle pair–wise solution of the Riemann problem. It is suggested that future efforts may be done to improve the computational efficiency by solving the Riemann problem only once for each particle and its neighbors.
- It is known that including turbulence models has a significant effect on the simulation of violent free-surface flows. Therefore, it is of great benefit to understand how the inclusion of SPH turbulence model can influence the accuracy and stability of the proposed WCSPH method based on Riemann solver.
- In this thesis, the modified WENO reconstruction is implemented for the WCSPH simulation of incompressible free-surface flows. Its straightforward that the present method may be extended to simulate compressible flows.
- Other high resolution approximations, such as RKPM [81], can be incorporated into the present WENO reconstruction by a MOOD-type approach [66] to increase the overall numerical accuracy.

Bibliography

[1] John David Anderson and J Wendt. *Computational fluid dynamics*. Vol. 206. Springer, 1995.

[2] ML McAllister et al. "Laboratory recreation of the Draupner wave and the role of breaking in crossing seas". In: *Journal of Fluid Mechanics* 860 (2019), pp. 767–786.

[3] Roel Luppes et al. "Simulations of Wave Impact and Two-Phase Flow with ComFLOW: Past and Recent Developments". In: *The Twenty-third International Offshore and Polar Engineering Conference*. International Society of Offshore and Polar Engineers. 2013.

[4] Ashkan Rafiee et al. "Comparative study on the accuracy and stability of SPH schemes in simulating energetic free-surface flows". In: *European Journal of Mechanics-B/Fluids* 36 (2012), pp. 1–16.

[5] European Space Agency. *Image: Hypervelocity impact testing*. 2018. URL: `https://phys.org/news/2018-02-image-hypervelocity-impact.html` (visited on 06/06/2019).

[6] Chi Zhang, Xiangyu Y Hu, and Nikolaus A Adams. "A generalized transport-velocity formulation for smoothed particle hydrodynamics". In: *Journal of Computational Physics* 337 (2017), pp. 216–232.

[7] Olgierd Cecil Zienkiewicz et al. *The finite element method*. Vol. 3. McGraw-hill London, 1977.

[8] Leon B Lucy. "A Numerical Approach to the Testing of the Fission Hypothesis". In: *The astronomical journal* 82 (1977), pp. 1013–1024.

[9] J J Monaghan. "SPH and Riemann solvers". In: *J. Comput. Phys.* 136.2 (1997), pp. 298–307.

[10] Seiichi Koshizuka and Yoshiaki Oka. "Moving-particle semi-implicit method for fragmentation of incompressible fluid". In: *Nuclear science and engineering* 123.3 (1996), pp. 421–434.

[11] Ante Munjiza. *The combined finite-discrete element method*. Vol. 32. Wiley Online Library, 2004.

[12] Joe J Monaghan. "Smoothed Harticle Hydrodynamics". In: *Reports on progress in physics* 68.8 (2005), p. 1703.

[13] M B Liu and G R Liu. "Smoothed particle hydrodynamics (SPH): an overview and recent developments". In: *Arch. Comput. Methods Eng.* 17.1 (2010), pp. 25–76.

[14] J J Monaghan. "Smoothed particle hydrodynamics and its diverse applications". In: *Annu. Rev. Fluid Mech.* 44 (2012), pp. 323–346.

[15] Robert A Gingold and Joseph J Monaghan. "Smoothed Particle Hydrodynamics: theory and application to non-spherical stars". In: *Monthly notices of the royal astronomical society* 181.3 (1977), pp. 375–389.

[16] Joseph J Monaghan. "SPH without a tensile instability". In: *Journal of Computational Physics* 159.2 (2000), pp. 290–311.

[17] J P Gray, J J Monaghan, and R P Swift. "SPH elastic dynamics". In: *Computer methods in applied mechanics and engineering* 190.49 (2001), pp. 6641–6662.

[18] P W Randles and L D Libersky. "Smoothed Particle Hydrodynamics: some recent improvements and applications". In: *Computer methods in applied mechanics and engineering* 139.1 (1996), pp. 375–408.

[19] Joseph J Monaghan. "Simulating free surface flows with SPH". In: *Journal of computational physics* 110.2 (1994), pp. 399–406.

[20] Joseph P Morris, Patrick J Fox, and Yi Zhu. "Modeling low Reynolds number incompressible flows using SPH". In: *Journal of computational physics* 136.1 (1997), pp. 214–226.

[21] X Y Hu and Nikolaus A Adams. "A multi-phase SPH method for macroscopic and mesoscopic flows". In: *J. Comput. Phys.* 213.2 (2006), pp. 844–861.

[22] X Y Hu and Nikolaus A Adams. "An incompressible multi-phase SPH method". In: *Journal of Computational Physics* 227.1 (2007), pp. 264–278.

[23] S Adami, XY Hu, and NA Adams. "A generalized wall boundary condition for smoothed particle hydrodynamics". In: *Journal of Computational Physics* 231.21 (2012), pp. 7057–7075.

[24] Carla Antoci, Mario Gallati, and Stefano Sibilla. "Numerical simulation of fluid–structure interaction by SPH". In: *Computers & Structures* 85.11 (2007), pp. 879–890.

[25] Ting Ye et al. "Smoothed particle hydrodynamics (SPH) for complex fluid flows: Recent developments in methodology and applications". In: *Physics of Fluids* 31.1 (2019), p. 011301.

[26] J J Monaghan and R A Gingold. "Shock simulation by the particle method SPH". In: *J. Comput. Phys.* 52.2 (1983), pp. 374–389.

[27] Angela Ferrari et al. "A new 3D parallel SPH scheme for free surface flows". In: *Computers & Fluids* 38.6 (2009), pp. 1203–1217.

[28] M Antuono, Andrea Colagrossi, and S Marrone. "Numerical diffusive terms in weakly-compressible SPH schemes". In: *Comput. Phys. Commun.* 183.12 (2012), pp. 2570–2580.

[29] C Zhang, XY Hu, and NA Adams. "A weakly compressible SPH method based on a low-dissipation Riemann solver". In: *Journal of Computational Physics* 335 (2017), pp. 605–620.

[30] S Adami, X Y Hu, and N A Adams. "A transport-velocity formulation for Smoothed Particle Hydrodynamics". In: *Journal of Computational Physics* 241 (2013), pp. 292–307.

[31] Gui Rong Liu and M B Liu. *Smoothed particle hydrodynamics: a meshfree particle method*. World Scientific, 2003.

[32] M B Liu, G R Liu, and K Y Lam. "Constructing smoothing functions in smoothed particle hydrodynamics with applications". In: *Journal of Computational and Applied Mathematics* 155.2 (2003), pp. 263–284.

[33] Joseph J Monaghan and John C Lattanzio. "A refined particle method for astrophysical problems". In: *Astronomy and astrophysics* 149 (1985), pp. 135–143.

[34] Joe J Monaghan. "Smoothed particle hydrodynamics". In: *Annual review of astronomy and astrophysics* 30.1 (1992), pp. 543–574.

[35] Daniel James Price. "Magnetic fields in Astrophysics". In: *Institute of Astronomy & Churchill College, Cambridge, Cambridge* (2004).

[36] Holger Wendland. "Piecewise polynomial, positive definite and compactly supported radial functions of minimal degree". In: *Advances in computational Mathematics* 4.1 (1995), pp. 389–396.

[37] Andrea Colagrossi and Maurizio Landrini. "Numerical simulation of interfacial flows by smoothed particle hydrodynamics". In: *Journal of Computational Physics* 191.2 (2003), pp. 448–475.

[38] Carl Eckart. "Variation principles of hydrodynamics". In: *The Physics of Fluids* 3.3 (1960), pp. 421–427.

[39] Joseph J Monaghan. "An introduction to SPH". In: *Computer physics communications* 48.1 (1988), pp. 89–96.

[40] XY Hu and NA Adams. "Angular-momentum conservative smoothed particle dynamics for incompressible viscous flows". In: *Physics of Fluids* 18.10 (2006), p. 101702.

[41] Willie Benz and Erik Asphaug. "Impact simulations with fracture. I. Method and tests". In: *ICARUS* 107.1 (1994), pp. 98–116.

[42] Willy Benz and Erik Asphaug. "Simulations of brittle solids using smooth particle hydrodynamics". In: *Computer physics communications* 87.1 (1995), pp. 253–265.

[43] E-S Lee et al. "Comparisons of weakly compressible and truly incompressible algorithms for the SPH mesh free particle method". In: *J. Comput. Phys.* 227.18 (2008), pp. 8417–8436.

[44] Eleuterio F Toro. *Riemann solvers and numerical methods for fluid dynamics: a practical introduction*. Springer Science & Business Media, 2009.

[45] Eleuterio F Toro. *Riemann solvers and numerical methods for fluid dynamics: a practical introduction*. Springer Science & Business Media, 2013.

[46] B D Roges, RA Dalrymple, and P K Stansby. "User guide for the SPHysics Code v2.0". In: *http://wiki.manchester.ac.uk/sphysics* (2010).

[47] Kazunari Iwasaki and Shu-ichiro Inutsuka. "Smoothed particle magnetohydrodynamics with a Riemann solver and the method of characteristics". In: *Mon. Not. R. Astron. Soc.* 418.3 (2011), pp. 1668–1688.

[48] Giuseppe Murante et al. "Hydrodynamic simulations with the Godunov smoothed particle hydrodynamics". In: *Monthly Notices of the Royal Astronomical Society* 417.1 (2011), pp. 136–153.

[49] Lin Fu, Xiangyu Y Hu, and Nikolaus A Adams. "A family of high-order targeted ENO schemes for compressible-fluid simulations". In: *Journal of Computational Physics* 305 (2016), pp. 333–359.

[50] Bing Wang, Gaoming Xiang, and Xiangyu Hu. "An incremental-stencil WENO reconstruction for simulation of compressible two-phase flows". In: *International Journal of Multiphase Flow* 104 (2018), pp. 20–31.

[51] Guang-Shan Jiang and Chi-Wang Shu. "Efficient Implementation of Weighted ENO Schemes". In: *Journal of Computational Physics* 126.1 (1996), pp. 202–228.

[52] S Litvinov, X Y Hu, and N A Adams. "Towards consistence and convergence of conservative SPH approximations". In: *submitted* (2015).

[53] Joe J Monaghan and Jules B Kajtar. "SPH particle boundary forces for arbitrary boundaries". In: *Comput. Phys. Commun.* 180.10 (2009), pp. 1811–1820.

[54] Martin Ferrand et al. "Unified semi-analytical wall boundary conditions for inviscid, laminar or turbulent flows in the meshless SPH method". In: *Int. J. Numer. Methods Fluids* 71.4 (2013), pp. 446–472.

[55] François Dubois. "3.1 Partial Riemann Problem, Boundary Conditions, and Gas Dynamics." In: *Absorbing Boundaries and Layers, Domain Decomposition Methods: Applications to Large Scale Computers* (2001), p. 16.

[56] S Marrone et al. "Fast free-surface detection and level-set function definition in SPH solvers". In: *J. Comput. Phys.* 229.10 (2010), pp. 3652–3663.

[57] J P Vila. "On particle weighted methods and smooth particle hydrodynamics". In: *Math. Models Methods Appl. Sci.* 9.02 (1999), pp. 161–209.

[58] Bachir Ben Moussa. "On the convergence of SPH method for scalar conservation laws with boundary conditions". In: *Methods and applications of analysis* 13.1 (2006), pp. 29–62.

[59] Shu Ichiro Inutsuka. "Reformulation of smoothed particle hydrodynamics with Riemann solver". In: *J. Comput. Phys.* 179.1 (2002), pp. 238–267.

[60] Anatoly N Parshikov and Stanislav A Medin. "Smoothed particle hydrodynamics using interparticle contact algorithms". In: *J. Comput. Phys.* 180.1 (2002), pp. 358–382.

[61] Diego Molteni and Andrea Colagrossi. "A simple procedure to improve the pressure evaluation in hydrodynamic context using the SPH". In: *Comput. Phys. Commun.* 180.6 (2009), pp. 861–872.

[62] S Marrone et al. "δ-SPH model for simulating violent impact flows". In: *Computer Methods in Applied Mechanics and Engineering* 200.13 (2011), pp. 1526–1542.

[63] Sergio Pirozzoli. "Numerical methods for high-speed flows". In: *Annual review of fluid mechanics* 43 (2011), pp. 163–194.

[64] Xueying Zhang et al. "A contact SPH method with high-order limiters for simulation of inviscid compressible flows". In: *Communications in Computational Physics* 14.02 (2013), pp. 425–442.

[65] Diego Avesani, Michael Dumbser, and Alberto Bellin. "A new class of Moving-Least-Squares WENO–SPH schemes". In: *Journal of Computational Physics* 270 (2014), pp. 278–299.

[66] Xesús Nogueira et al. "High-accurate SPH method with multidimensional optimal order detection limiting". In: *Computer Methods in Applied Mechanics and Engineering* 310 (2016), pp. 134–155.

[67] Sergey Litvinov, XY Hu, and NA Adams. "Towards consistence and convergence of conservative SPH approximations". In: *Journal of Computational Physics* 301 (2015), pp. 394–401.

[68] C Zhang et al. "A weakly compressible SPH method with WENO reconstruction". In: *Journal of Computational Physics* 392 (2019), pp. 1–18.

[69] Kunal Puri and Prabhu Ramachandran. "A comparison of SPH schemes for the compressible Euler equations". In: *J. Comput. Phys.* 256 (2014), pp. 308–333.

[70] Seung-Hoon Cha, Shu-ichiro Inutsuka, and Sergei Nayakshin. "Kelvin–Helmholtz instabilities with Godunov smoothed particle hydrodynamics". In: *Mon. Not. R. Astron. Soc.* 403.3 (2010), pp. 1165–1174.

[71] S Borgani et al. "Hydrodynamic Simulations with the Godunov SPH". In: *Advances in Computational Astrophysics: Methods, Tools, and Outcome*. Vol. 453. 2012, p. 259.

[72] Bram Van Leer. "Flux-vector splitting for the Euler equation". In: *Upwind and High-Resolution Schemes*. Springer, 1997, pp. 80–89.

[73] I Schuessler and D Schmitt. "Comments on Smoothed Particle Hydrodynamics". In: *Astronomy and Astrophysics* 97 (1981), pp. 373–379.

[74] Gordon R Johnson and Stephen R Beissel. "Normalized smoothing functions for SPH impact computations". In: *International Journal for Numerical Methods in Engineering* 39.16 (1996), pp. 2725–2741.

[75] D A Mandell, C A Wingate, and L A Schwalbe. *Computational brittle fracture using Smooth Particle Hydrodynamics*. Tech. rep. Los Alamos National Lab., NM (United States), 1996.

[76] Gary A Dilts. "Moving-least-squares-particle hydrodynamicsÑI. Consistency and stability". In: *International Journal for Numerical Methods in Engineering* 44.8 (1999), pp. 1115–1155.

[77] C T Dyka, P W Randles, and R P Ingel. "Stress points for tension instability in SPH". In: *International Journal for Numerical Methods in Engineering* 40.13 (1997), pp. 2325–2341.

[78] P W Randles and L D Libersky. "Normalized SPH with stress points". In: *International Journal for Numerical Methods in Engineering* 48.10 (2000), pp. 1445–1462.

[79] Libor Lobovskỳ and Jiří Křen. "Smoothed particle hydrodynamics modelling of fluids and solids". In: *Applied and Computational Mechanics* 1.49 (2007), pp. 521–530.

[80] XY Hu and NA Adams. "A SPH model for incompressible turbulence". In: *Procedia IUTAM* 18 (2015), pp. 66–75.

[81] Wing Kam Liu et al. "Overview and applications of the reproducing kernel particle methods". In: *Archives of Computational Methods in Engineering* 3.1 (1996), pp. 3–80.

Appendix A

Original journal papers

Here, the peer-reviewed journal publications of the present work are attached.

A.1 Paper I

Chi Zhang, Xiangyu Y. Hu, Nikolaus A. Adams

A weakly compressible SPH method based on a low-dissipation Riemann solver

In *Journal of Computational Physics*, Volume 335, 2017, pp. 605-620, DOI: `https://doi.org/10.1016/j.jcp.2017.01.027`.

Contribution: My contribution to this work was the development of the method and the corresponding computer code for its implementation. I performed simulations and analyzed the results, and wrote the manuscript for the publication.

Journal of Computational Physics 335 (2017) 605–620

Contents lists available at ScienceDirect

Journal of Computational Physics

www.elsevier.com/locate/jcp

A weakly compressible SPH method based on a low-dissipation Riemann solver

C. Zhang, X.Y. Hu *, N.A. Adams

Lehrstuhl für Aerodynamik und Strömungsmechanik, Technische Universität München, 85748 Garching, Germany

ARTICLE INFO

Article history:
Received 17 October 2016
Accepted 16 January 2017
Available online 26 January 2017

Keywords:
Weakly-compressible SPH
Riemann solver
Violent free-surface flows

ABSTRACT

We present a low-dissipation weakly-compressible SPH method for modeling free-surface flows exhibiting violent events such as impact and breaking. The key idea is to modify a Riemann solver which determines the interaction between particles by a simple limiter to decrease the intrinsic numerical dissipation. The modified Riemann solver is also extended for imposing wall boundary conditions. Numerical tests show that the method resolves free-surface flows accurately and produces smooth, accurate pressure fields. The method is compatible with the hydrostatic solution and exhibits considerably less numerical damping of the mechanical energy than previous methods.

1. Introduction

As a meshless Lagrangian approach, the smoothed particle hydrodynamics (SPH) method was first proposed by Lucy [1], Gigold and Monaghan [2] for astrophysical applications. It has been successfully extended to a wide range of problems in solid mechanics, e.g. Refs. [3–5], fluid dynamics, e.g. Refs. [6–10] and fluid structure interactions [11]. Comprehensive reviews can be found in Refs. [12,13].

Concerning the computation of hydrodynamic problems, the weakly compressible SPH (WCSPH) method assumes that the fluid is weakly compressible with a small variation of density [6,7]. When simulating violent free surface breaking and impact problems with WCSPH the pressure which is evaluated through density by using an artificial equation of state exhibits spurious oscillations which may lead to numerical instability [14,15].

Monaghan and Gingold [16] proposed an Neumann–Richtmeyer type artificial viscosity term in the momentum equation to dampen the pressure oscillations. While a moderate artificial viscosity is able to stabilize the computation, it may lead to excessive dissipation which affects the physical flow characteristics. Colagrossi and Landrini [17] suggested to use a Mean Least Squares (MLS) interpolation to filter the density field. This approach gives good results while is computationally rather expensive [15].

Vila [18] and Moussa [19] developed a SPH method based on solving a Riemann problem along interacting particles. The advantage of this method is that no explicit artificial viscosity is used and the numerical dissipation is introduced implicitly [18,19]. Unfortunately, this method is very dissipative even when an exact Riemann solver is applied [20]. Similar ideas of enhancing numerical stability using Riemann solvers are also proposed in Refs. [21–23]. Monaghan [21] pointed out that the artificial viscosity [16] is analogous to the intrinsic numerical dissipation of the Riemann solver, which scales with the wave speed and the velocity jump between interacting particles. While these methods have been applied to solve shock

* Corresponding author.
E-mail address: xiangyu.hu@tum.de (X.Y. Hu).

http://dx.doi.org/10.1016/j.jcp.2017.01.027
0021-9991/

tube problems [24], solid mechanics problems [23], interface instability [25,26] and MHD [27] problems, they are generally more dissipative than those based on artificial viscosity, and do not reproduce violent free-surface flows reliably.

To cope with the excessive dissipation introduced by directly applying a Riemann solver, Ferrari [20] proposed to add an artificial diffusion into the continuity equation. Molten and Colagrossi [28] pursued a similar idea but still applied a small amount of artificial viscosity [16]. Although both methods are able to recover violent free-surface flows with reasonably smooth pressure profiles, they are not compatible with the hydrostatic solution, which results in unphysical free-surface motion and expansion. A computationally quite involved correction [29] is proposed to decrease such artifacts.

In this paper we propose a low-dissipation Riemann solver for the WCSPH method to simulate violent free-surface flows. Other than applying the classic Riemann solvers directly [18,19,22,23], the present method introduces a simple low-dissipation limiter to a classic Riemann solver ensuring no or decreased numerical dissipation for expansion or compression waves, respectively. Unlike using explicit diffusive terms as in Refs. [20,28], the present method regularizes the density profile implicitly by the Riemann solver. In addition, a wall boundary condition based on the one-sided Riemann solver is developed to handle violent breaking-wave impact. To test the robustness and accuracy of the low-dissipative Riemann solver, a number of two and three-dimensional tests, including the Taylor–Green vortex, a hydrostatic test and several dam-break problems, are carried out and the results are compared to analytical and previous results.

2. Method

The conservation of mass and momentum in the Lagrangian frame for inviscid flow can be written as

$$\begin{cases} \frac{d\rho}{dt} = -\rho\nabla\cdot\mathbf{v} \\ \frac{d\mathbf{v}}{dt} = -\frac{1}{\rho}\nabla P \end{cases}, \tag{1}$$

where ρ is density, $\mathbf{v}$ is velocity, t is time, P is pressure and $\frac{d}{dt} = \frac{\partial}{\partial t} + \mathbf{v}\cdot\nabla$ refers to the material derivative. Applying the weakly compressible assumption, the fluid pressure is evaluated through density from an artificial equation of state

$$P = c_0^2(\rho - \rho_0), \tag{2}$$

where c_0 is the speed of sound and determined by $c_0 = 10V_{max}$ where V_{max} represents the maximum anticipated flow speed.

Following Refs. [8,12,13,18], a standard WCSPH discretization of the continuity equation is

$$\frac{d\rho_i}{dt} = \rho_i\sum_j \frac{m_j}{\rho_j}\mathbf{v}_{ij}\cdot\nabla_i W_{ij} = 2\rho_i\sum_j \frac{m_j}{\rho_j}(\mathbf{v}_i - \overline{\mathbf{v}}_{ij})\cdot\nabla_i W_{ij}. \tag{3}$$

Here, m_j is the particle mass, $\mathbf{v}_{ij} = \mathbf{v}_i - \mathbf{v}_j$ and $\overline{\mathbf{v}}_{ij} = (\mathbf{v}_i + \mathbf{v}_j)/2$ are the relative and average velocities, between particle i and j, respectively. $\nabla_i W_{ij}$ is the gradient of the kernel function $W(|\mathbf{r}_{ij}|, h)$, where $\mathbf{r}_{ij} = \mathbf{r}_i - \mathbf{r}_j$, and h is the smoothing length with respect to $\mathbf{r}_i$, position of particle i. A standard discretization of the momentum equation without taking account artificial viscosity [13,16] is

$$\frac{d\mathbf{v}_i}{dt} = -\sum_j m_j\left(\frac{P_i + P_j}{\rho_i\rho_j}\right)\nabla_i W_{ij} = -2\sum_j m_j\frac{\overline{P}_{ij}}{\rho_i\rho_j}\nabla_i W_{ij}, \tag{4}$$

where $\overline{P}_{ij} = (P_i + P_j)/2$ is the average pressure between particle i and j. In standard WCSPH the discretized momentum equation also includes an artificial viscosity term

$$\left(\frac{d\mathbf{v}_i}{dt}\right)^{(\nu)} = -\sum_j m_j\alpha\frac{hc_0}{\overline{\rho}}\frac{\mathbf{v}_{ij}\cdot\mathbf{r}_{ij}}{|\mathbf{r}_{ij}|^2}\nabla_i W_{ij} \tag{5}$$

where $\overline{\rho} = (\rho_L + \rho_R)/2$, and $\alpha \le 1.0$ is a tunable parameter.

2.1. WCSPH method based on a Riemann solver

For an SPH method based on Riemann solvers [18,19] an inter-particle Riemann problem is constructed along a unit vector $\mathbf{e}_{ij} = -\mathbf{r}_{ij}/r_{ij}$ pointing form particle i to particle j, as shown in Fig. 1. In this Riemann problem the initial left and right states are on particles i and j, respectively, and the discontinuity is at the middle point $\bar{\mathbf{r}}_{ij} = \frac{1}{2}(\mathbf{r}_i + \mathbf{r}_j)$. The L and R states are

$$\begin{cases} (\rho_L, U_L, P_L) = (\rho_i, \mathbf{v}_i\cdot\mathbf{e}_{ij}, P_i) \\ (\rho_R, U_R, P_R) = (\rho_j, \mathbf{v}_j\cdot\mathbf{e}_{ij}, P_j) \end{cases}. \tag{6}$$

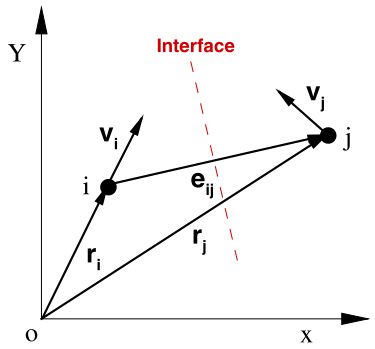

Fig. 1. Construction of Riemann problem along the interacting line of particles i and j.

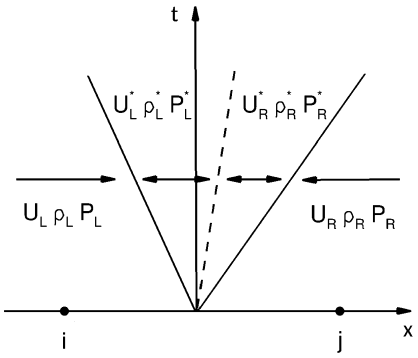

Fig. 2. Simplified Riemann fan with two intermediate states.

It is worth noting that such a Riemann problem is based on a piece-wise constant assumption, i.e. 1st-order reconstruction.

The solution of the Riemann problem results in three waves emanating from the discontinuity [30], as shown in Fig. 2. Two waves, which can be shock or rarefaction wave, traveling with the smallest or largest wave speed. The middle wave is always a contact discontinuity and separates two intermediate states, denoted by (ρ_L^*, U_L^*, P_L^*) and (ρ_R^*, U_R^*, P_R^*). By assuming that the intermediate state satisfies $U_L^* = U_R^* = U^*$ and $P_L^* = P_R^* = P^*$, a linearised Riemann solver [30] for smooth flows or with only moderately strong shocks can be written as

$$\begin{cases} U^* = \overline{U} + \frac{1}{2}\frac{(P_L - P_R)}{\bar{\rho} c_0} \\ P^* = \overline{P} + \frac{1}{2}\bar{\rho} c_0 (U_L - U_R) \end{cases}, \tag{7}$$

where $\overline{U} = (U_L + U_R)/2$ and $\overline{P} = (P_L + P_R)/2$ are inter-particle averages. With the solution of the Riemann problem, i.e. U^* and P^*, the discretization of the SPH method is

$$\frac{d\rho_i}{dt} = 2\rho_i \sum_j \frac{m_j}{\rho_j} (\mathbf{v}_i - \mathbf{v}^*) \cdot \nabla_i W_{ij}, \tag{8}$$

$$\frac{d\mathbf{v}_i}{dt} = -2 \sum_j m_j \left(\frac{P^*}{\rho_i \rho_j} \right) \nabla_i W_{ij}, \tag{9}$$

where $\mathbf{v}^* = U^* \mathbf{e}_{ij} + (\overline{\mathbf{v}}_{ij} - \overline{U}\mathbf{e}_{ij})$. This indicates that the inter-particle average velocity and pressure in Eqs. (3) and (4) are simply replaced by the solution of the Riemann problem. By comparing both it can be seen that the intermediate velocity and pressure in Eq. (7) from the inter-particle averages amount to implicit dissipation, i.e. density regularization and numerical viscosity, respectively.

2.2. Dissipation limiter

Since the above discretization is very dissipative a straightforward modification is to apply a limiter to decrease the implicit numerical dissipations introduced in Eq. (7). We propose to limit the intermediate pressure as

$$P^* = \overline{P} + \frac{1}{2}\beta \overline{\rho} (U_L - U_R), \tag{10}$$

where the limiter is defined as

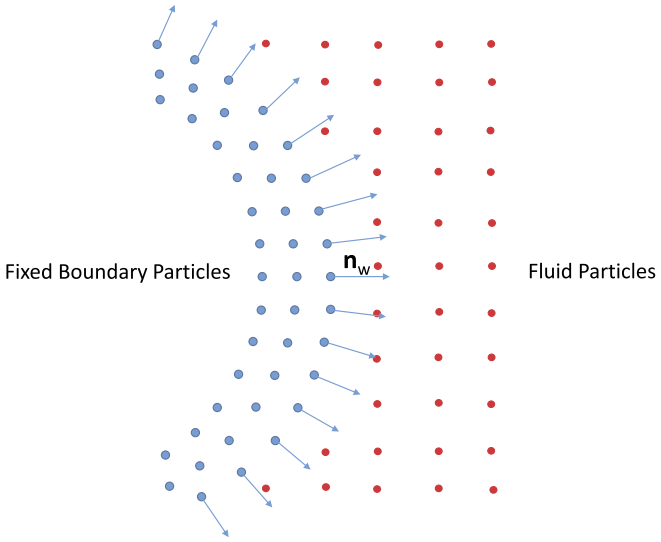

Fig. 3. Sketch of fluid particles interacting with fixed wall boundary particles along the wall normal direction through the one-side Riemann problem.

$$\beta = \min\left(\eta \max(U_L - U_R, 0), \overline{c}\right). \tag{11}$$

Note that β ensures that there is no dissipation when the fluid is under the action of an expansion wave, i.e. $U_L < U_R$, and that the parameter η is used to modulate dissipation when the fluid is under the action of a compression wave, i.e. $U_L \geq U_R$. We suggest $\eta = 3$ according to numerical tests and use it throughout this paper. Also note that the dissipation introduced by the intermediate velocity as in Eq. (7) is not limited.

2.3. Wall-boundary condition

Similarly to Adami et al. [10] fixed wall-boundary particles are used, as shown in Fig. 3, to impose the wall-boundary condition. The interaction between a fluid particle and a wall particle is determined by solving a one-sided Riemann problem [31] along the wall-normal direction.

In the one-sided Riemann problem the left state is defined from the fluid particle corresponding to the local boundary normal,

$$(\rho_L, U_L, P_L) = (\rho_f, -\mathbf{n}_w \cdot \mathbf{v}_f, P_f) \tag{12}$$

where the subscript f represents the fluid particles, $\mathbf{n}_w$ is the local wall-normal direction as shown in Fig. 3. According to the physical wall boundary condition the right-state velocity U_R is assumed as

$$U_R = -U_L + 2u_w, \tag{13}$$

where u_w is the wall velocity. Similarly to Adami et al. [10] the right-state pressure is assumed as

$$P_R = P_L + \rho_f \mathbf{g} \cdot \mathbf{r}_{fw}, \tag{14}$$

where $\mathbf{g}$ is the gravity force, $\mathbf{r}_{fw} = \mathbf{r}_w - \mathbf{r}_f$, and the right-state density is obtained by applying the artificial equation of state. Note that, unlike Adami et al. [10], since the Riemann problem is solved in a particle-by-particle fashion no interpolation of states for the wall particles is required. The wall normal direction is calculated for each wall particle by

$$\mathbf{n}_w = \frac{\boldsymbol{\Phi}(\mathbf{r}_i)}{|\boldsymbol{\Phi}(\mathbf{r}_i)|}, \quad \boldsymbol{\Phi}(\mathbf{r}_i) = -\sum_{j \in w} \frac{m_j}{\rho_j} \bigtriangledown W_{ij}, \tag{15}$$

where the summation is over wall particles only. A more accurate calculation would be to apply the reproducing-kernel correction [5,32]. For problems with static walls $\mathbf{n}_w$ is pre-computed before the numerical simulation. If there is a moving wall the wall-normal direction should be updated according to its rotation.

2.4. Time integration

A kick-drift-kick time-integration scheme [33,34] is applied. The half-time-step velocity is updated first, and then new time-step particle position is obtained as

$$\begin{cases} \mathbf{v}_i^{n+\frac{1}{2}} = \mathbf{v}_i^n + \frac{1}{2}\delta t \left(\frac{d\mathbf{v}_i}{dt}\right)^n \\ \mathbf{r}_i^{n+1} = \mathbf{r}_i^n + \delta t \mathbf{v}_i^{n+\frac{1}{2}} \end{cases}, \tag{16}$$

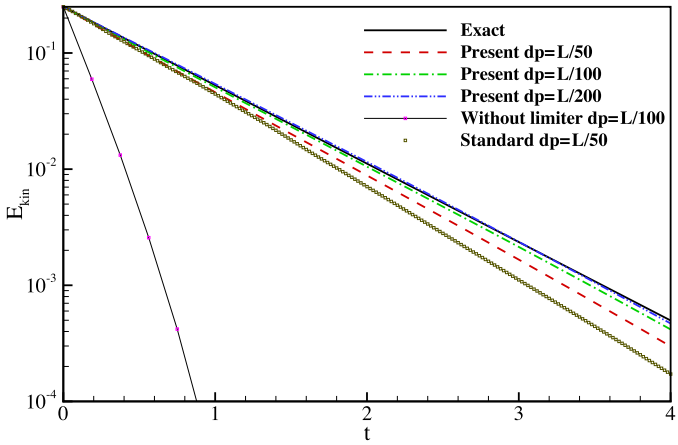

Fig. 4. Taylor–Green vortex: decay of the kinetic energy ($Re = 100$).

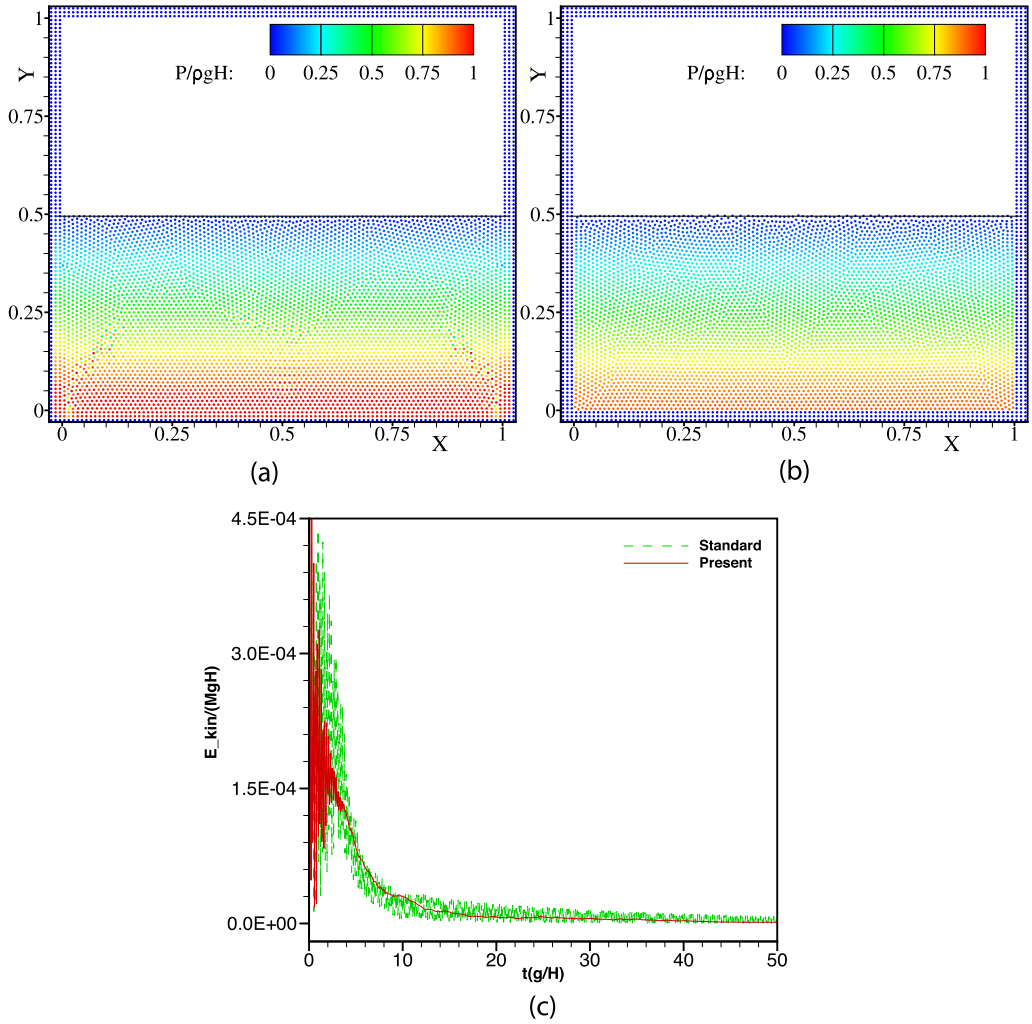

Fig. 5. The hydrostatic test where the initial free surface is denoted by solid line. The standard WCSPH method with artificial viscosity term (a), the present method (b) and the evolution of kinetic energy (c).

where the superscript n represents the old time step. After that the time-derivative of density $\left(\frac{d\rho_i}{dt}\right)^{n+1}$ is calculated through the updated flow states, the new-time-step particle density is updated by

$$\rho_i^{n+1} = \rho_i^n + \delta t \left(\frac{d\rho_i}{dt}\right)^{n+1}. \tag{17}$$

Then, the pressure is calculated through the updated particle density and the new-time-step rate of velocity $\left(\frac{d\mathbf{v}_i}{dt}\right)^{n+1}$ is computed. Finally, the new-time-step velocity is updated by

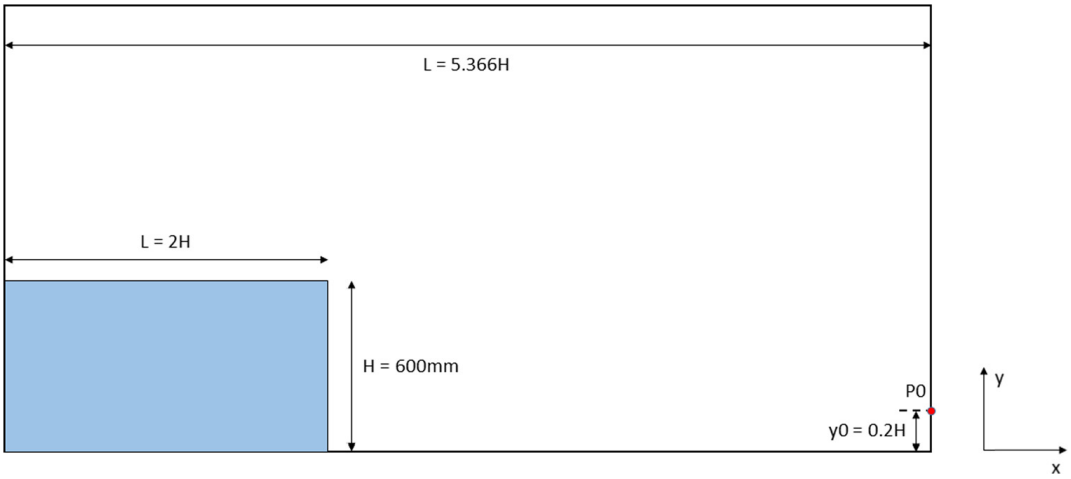

Fig. 6. Sketch of 2-D dam-break flow configuration. $P0$ indicates the pressure probe at the downstream wall.

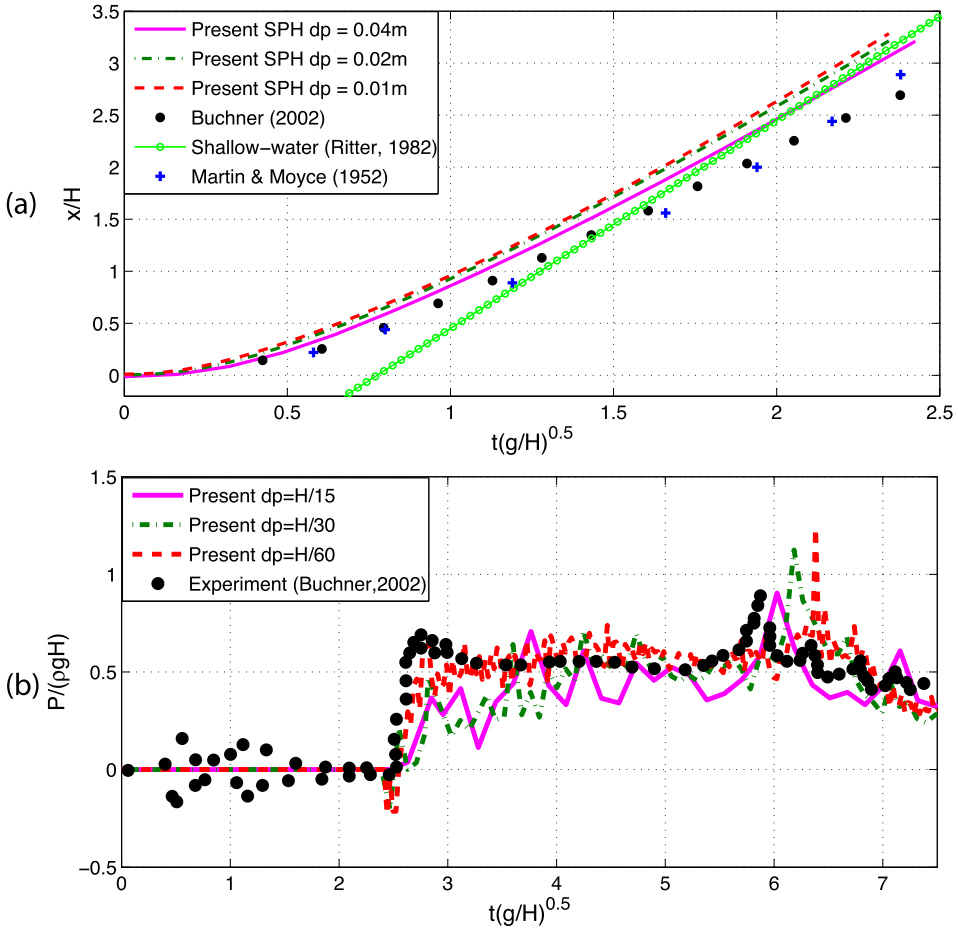

Fig. 7. Two-dimensional dam-break problem: (a) time evolution of the surge-wave front, (b) history of the pressure signals recorded at P0.

$$\mathbf{v}_i^{n+1} = \mathbf{v}_i^{n+\frac{1}{2}} + \frac{1}{2}\delta t\left(\frac{d\mathbf{v}_i}{dt}\right)^{n+1}. \tag{18}$$

For numerical stability, the CFL condition should be satisfied

$$\Delta t \leq 0.25\left(\frac{h}{c_0 + |U|}\right), \tag{19}$$

where $|U|$ is the maximum particle speed.

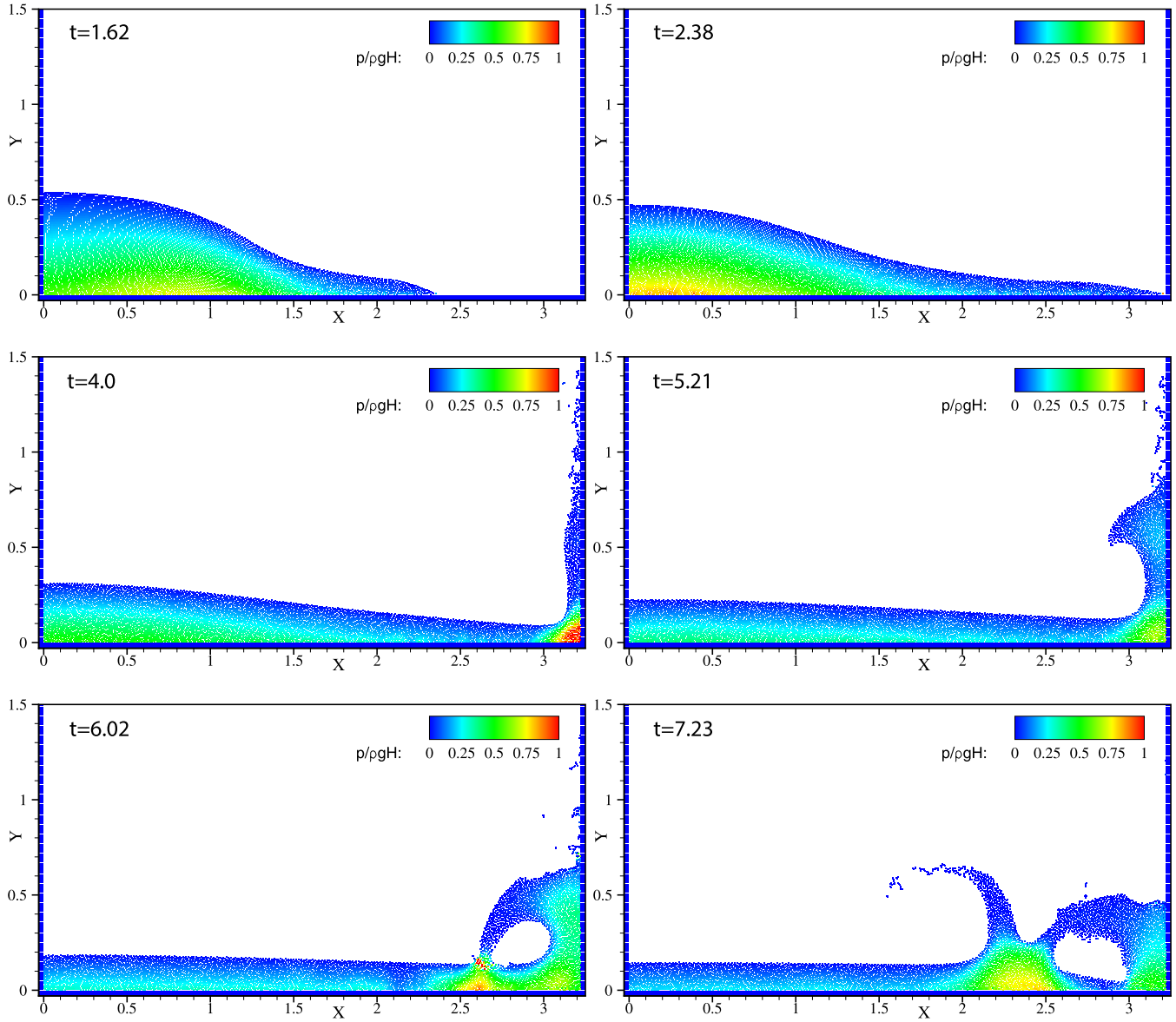

Fig. 8. Two-dimensional dam-break problem: snapshots of the free-surface profile at several time instances obtained with $dp = H/60$.

3. Numerical examples

In this section, Taylor–Green vortex, hydrostatic test and several dam-break problems involving violent free-surface breaking and impacting are used to validate the present method. The 5th-order Wendland kernel [35] with a smoothing length $h = 1.3dp$, where dp is the initial particle spacing, and a support radius $2.6dp$, are used in all test cases. The physical parameters density $\rho = 1000$ kg/m^3 and gravity $g = 9.8$ m/s^2 are applied. For all hydrodynamic cases, the maximum velocity is approximated as $V_{max} = 2\sqrt{gH}$, where H is the initial water depth, according to the shallow-water theory [36], for setting the speed of sound c_0. Note that for simplicity the water with zero initial pressure is released immediately when the computation starts instead of being released from a gate holding the pressure-relaxed water as in the experimental setup.

3.1. Taylor–Green vortex

The two-dimensional viscous Taylor–Green problem gives a periodic array of vortices with the velocity field given by

$$\begin{cases} u(x, y, t) = -Ue^{bt}\cos(2\pi x)\sin(2\pi y) \\ v(x, y, t) = Ue^{bt}\sin(2\pi x)\cos(2\pi y) \end{cases}, \tag{20}$$

where $b = -8\pi^2/Re$ is the decay rate, U is the initial maximum flow speed, Re is the Reynolds number and here we set $Re = 100$. The computation is performed on a square domain with unit length $L = 1$, and a periodic boundary condition is applied in both coordinate directions. The computation is carried out with three different particle resolutions, i.e. $dp = L/50$,

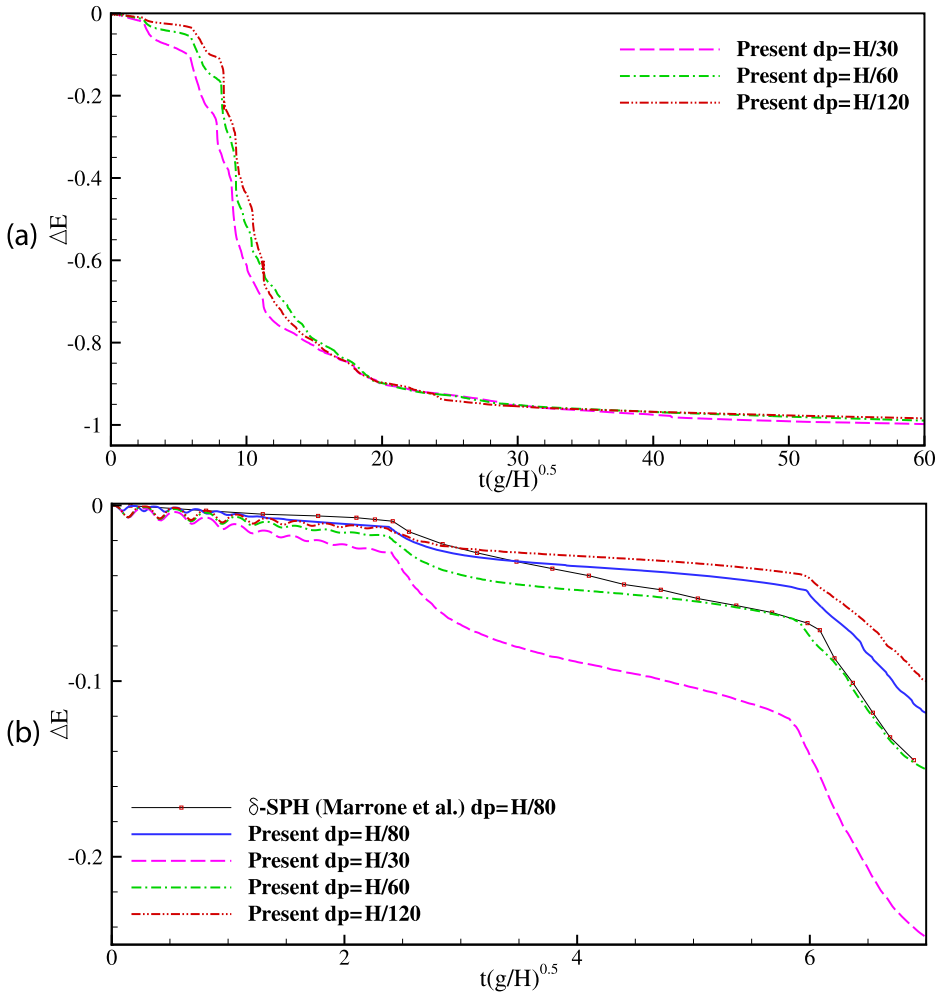

Fig. 9. Evolution of mechanical energy for the two-dimensional dam-break problem: (a) global evolution, (b) zoom in on the initial evolution.

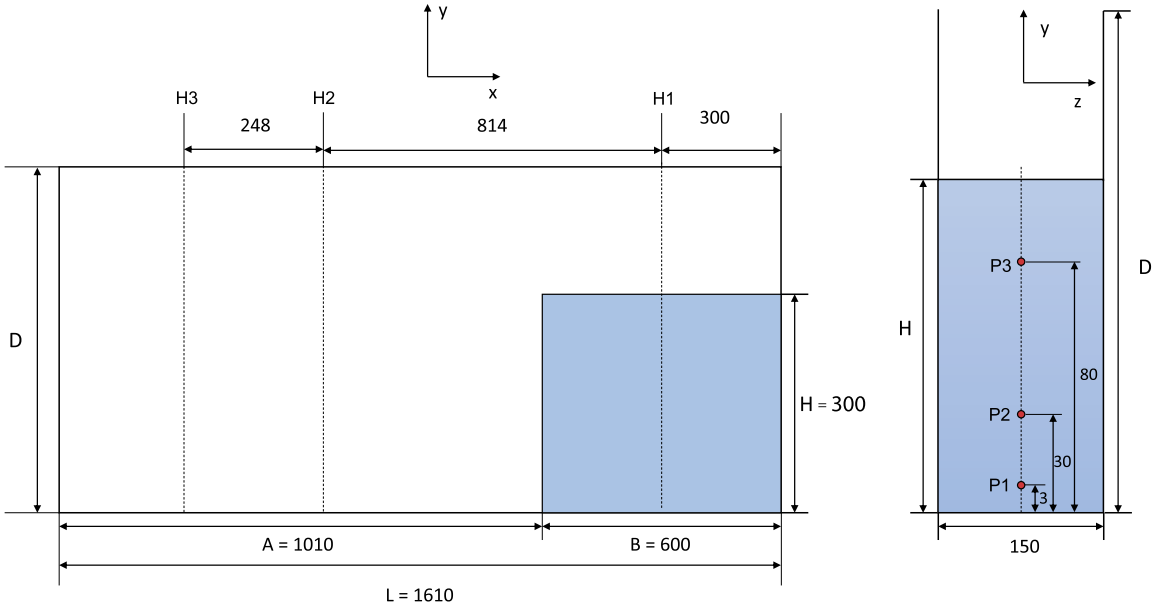

Fig. 10. Sketch of the three-dimensional dam-break problem with locations of free-surface and pressure sensors. Dimensions in millimeter.

$dp = L/100$ and $dp = L/200$ for convergence study. Similarly to Hu and Adams [9], to avoid the start-up effect a relaxed initial particle distribution is used.

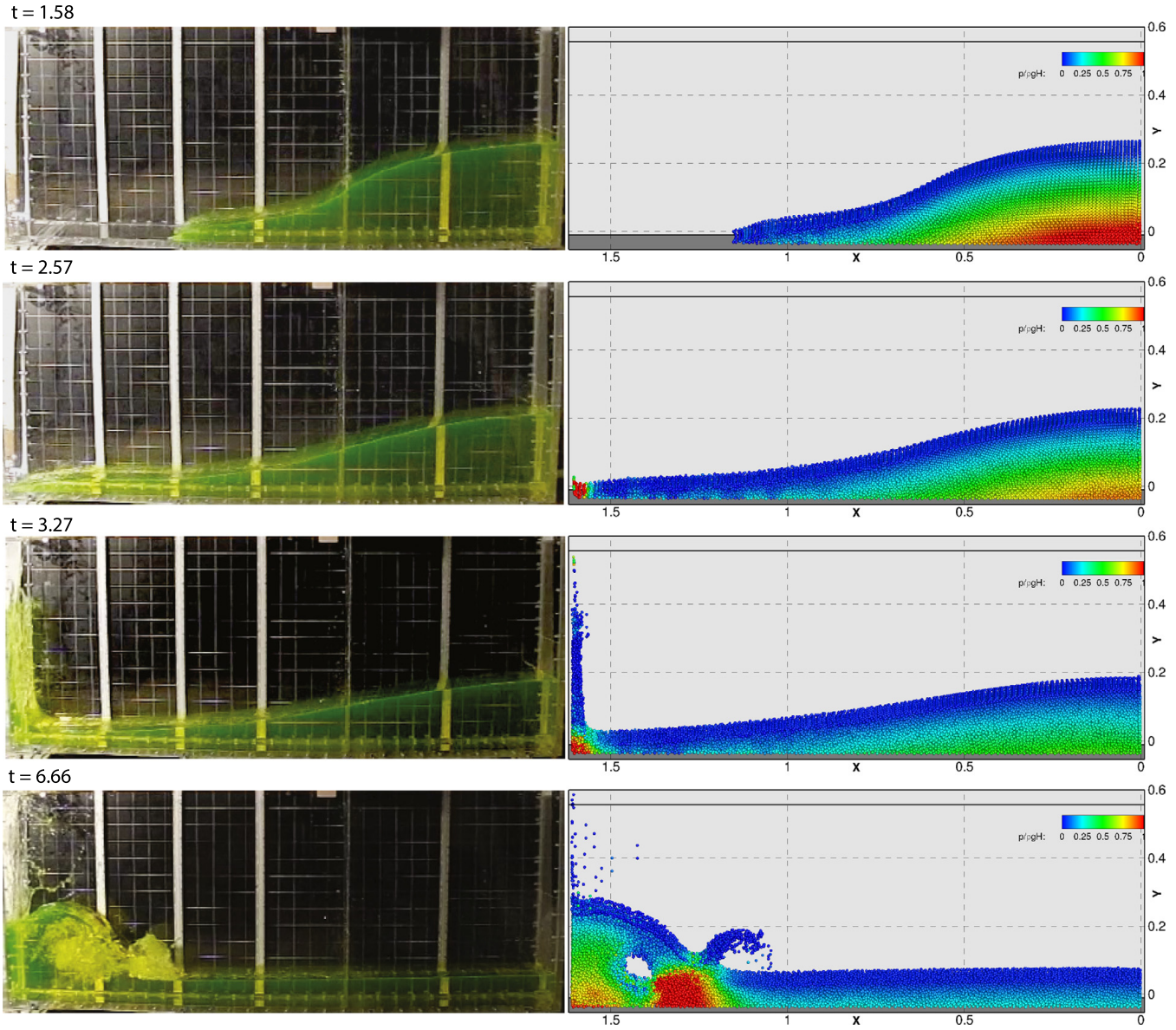

Fig. 11. Three-dimensional dam-break problem simulated with $dp = H/30$ (the total fluid particle number $N_f = 27000$): free-surface profile compared with experiment.

Fig. 4 gives the computed time evolution of the total kinetic energy and the corresponding analytical solution. It can be observed that the linear Riemann solver of Eq. (7) is too dissipative to predict a reasonable kinetic energy decay. Compared to the standard WCSPH with artificial viscosity ($\alpha = 0.02$), the present method achieves less dissipation and better agreement with the analytical solution. Also note that the present method achieves 2nd-order convergence for the total kinetic energy with increasing particle resolution.

3.2. Hydrostatic test

We consider a simple two-dimensional hydrostatic test, i.e. a tank is partially filled with water at rest. The tank has a length $L = 1$ and the initial water depth $H = 0.5$ denoted by a free-surface line as shown in Figs. 5(a) and (b). Initially, the particles are placed on a Cartesian lattice with a particle spacing of $dp = H/50$. For comparison, this test is also computed by the standard WCSPH with artificial viscosity ($\alpha = 0.02$) and the boundary condition as proposed by Adami et al. [10].

Figs. 5(a) and (b) show the obtained particle distribution and dimensionless pressure field at $t = 30$. Compared with the initial free-surface, no notable unphysical motion of free-surface particles is observed for both methods. Note that the present method produces a much smoother pressure field than the standard WCSPH. Fig. 5(c) shows the evolution of kinetic energy. After early-stage oscillations due to the weak compressibility the kinetic energy decays to a very small value quickly. It is also observed that the present method produces much less oscillations than the standard WCSPH, especially for late times. Note that the standard WCSPH using the small artificial-viscosity parameter $\alpha = 0.02$ is unable to compute other cases involving breaking waves due to numerical instability. This simple test shows that, without introducing the quite

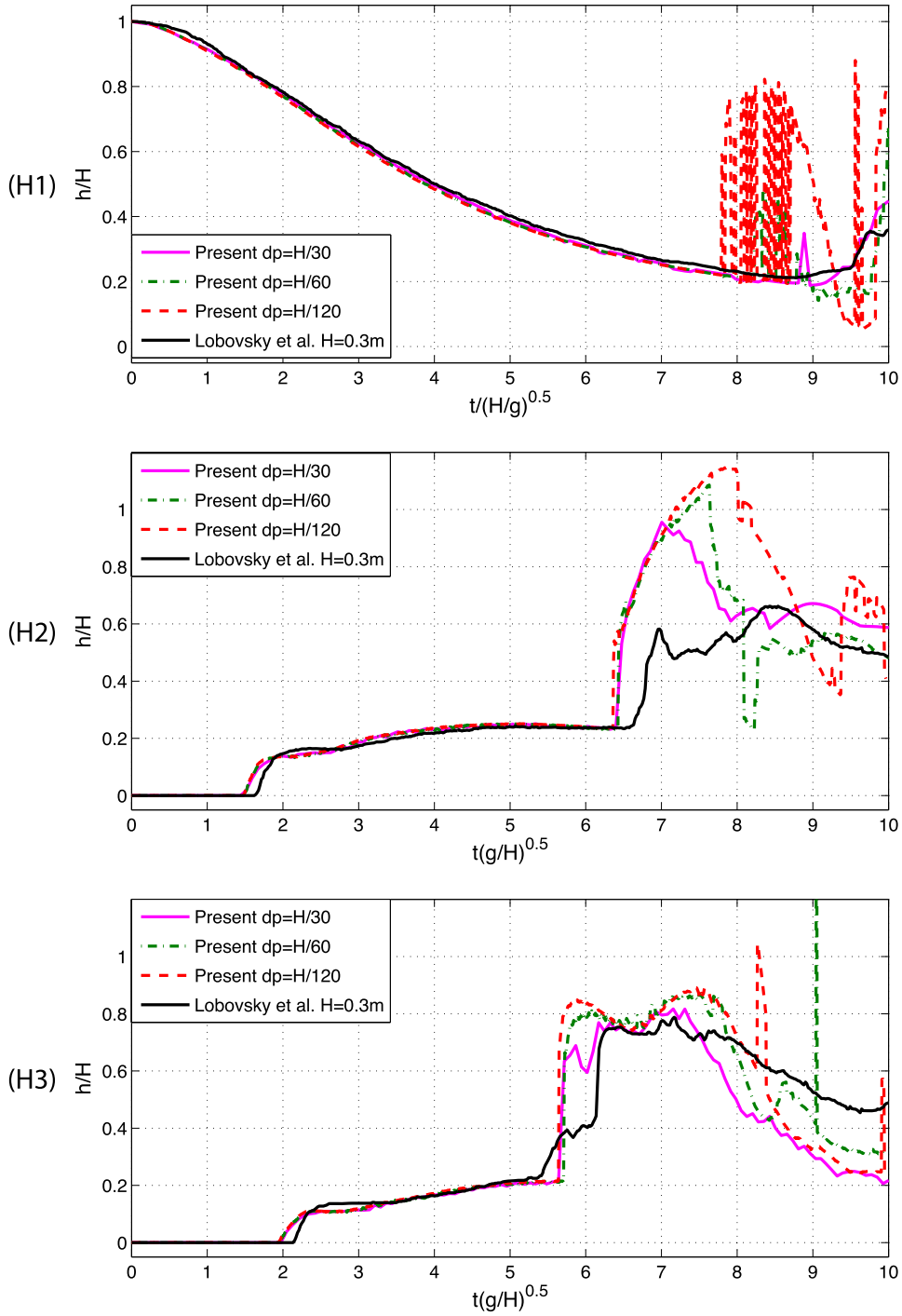

Fig. 12. Three-dimensional dam-break problem: the water-level recorded at $H1$, $H2$ and $H3$. Convergence study and comparison against experiment investigated by Lobovsky et al. [41].

elaborate correction approach [37], the present method is compatible with the hydrostatic solution, which is difficult for the density diffusion methods [20,28].

3.3. Two-dimensional dam break

We consider a two-dimensional dam-break problem which was studied by the methods using both artificial viscosity [10] and density diffusion [15,37]. The sketch of the configuration is shown in Fig. 6 where a pressure probe $P0$ located at the downstream wall is used to record pressure signals. Note that the probe position does not exactly match the experimental setup as Greco [38] suggested that a shift produces a better agreement [10]. We follow these suggesters.

In Fig. 7(a) we compare the computed propagation of surge-wave front with experimental data from Buchner [39], Martin and Moyce [40] and an analytical solution derived from the shallow-water equation [36]. It is observed that the

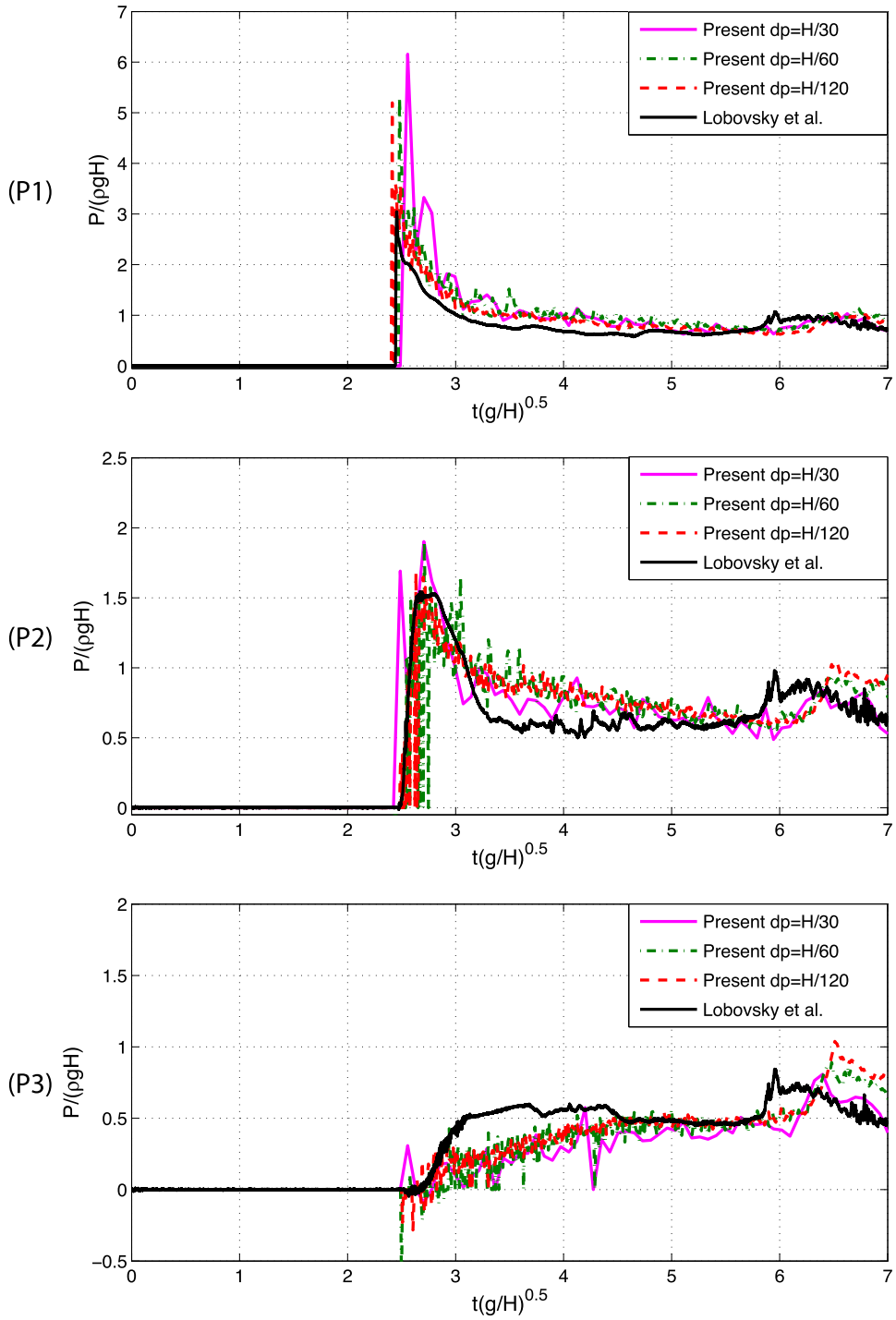

Fig. 13. Three-dimensional dam-break problem: history of pressure signals recorded at probes $P1$, $P2$ and $P3$. Convergence study and comparison against experiment investigated by Lobovsky et al. [41].

present results agree well with the analytical solution but, similarly to previous simulations [10,20,37], overestimate the front speed obtained from the experiments. Note that the computed propagation of the surge-wave front achieves about 2nd-order convergence with increasing particle resolution. Fig. 7(b) shows the history of pressure signals recorded at $P0$. It is observed that the main pressure plateau agrees well with the experimental data [39] and previous numerical results [20,37,17]. Several snapshots of the computed free surface at different time in stances are shown in Fig. 8. Compared with the results of Adami et al. [10] which applied the standard WCSPH, a higher rejected jet is produced by the present method.

In Marrone et al. [37] the numerical dissipation of mechanical energy is defined as

$$\Delta E = \frac{E_{kin} + E_{pot} - E^0_{pot}}{E^0_{pot} - E^\infty_{pot}}, \tag{21}$$

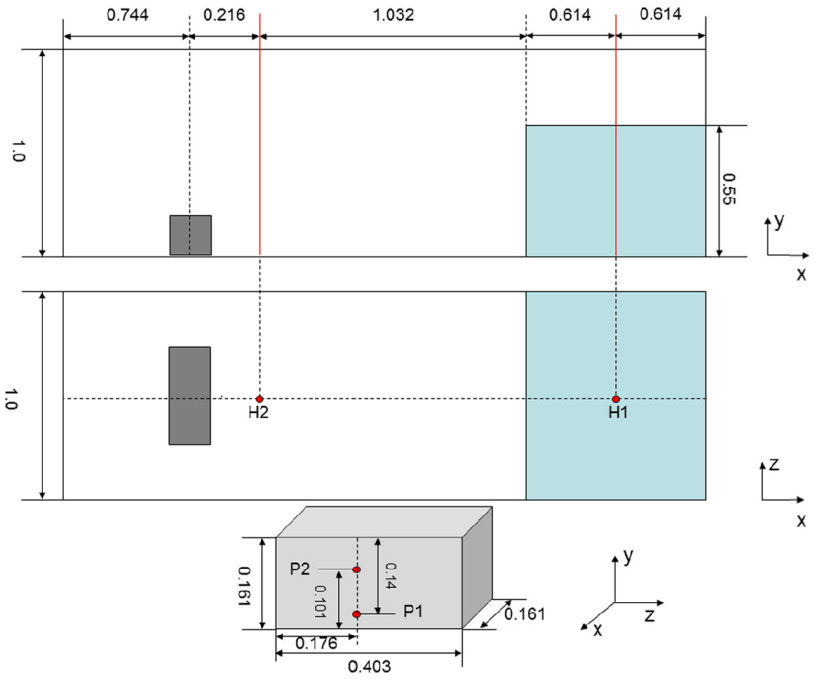

Fig. 14. Sketch of the three-dimensional dam break with an obstacle and water-level and pressure measuring points.

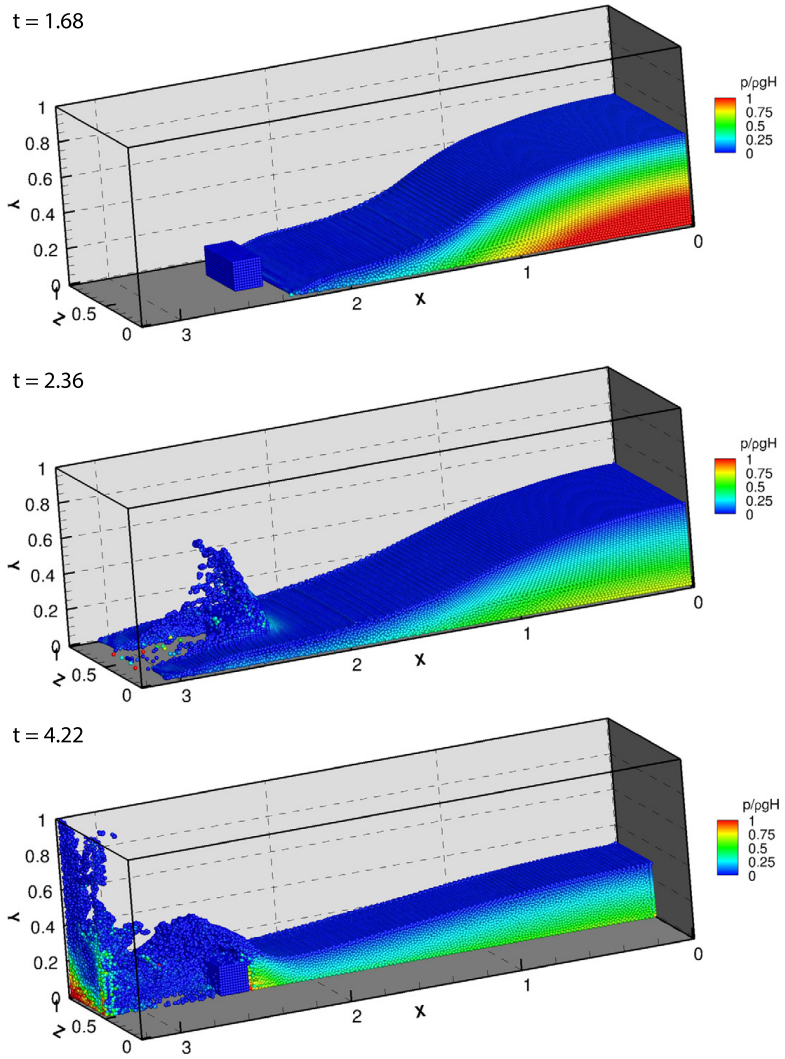

Fig. 15. Snapshots of 3-D free-surface flows impact at an obstacle at specific time in stances.

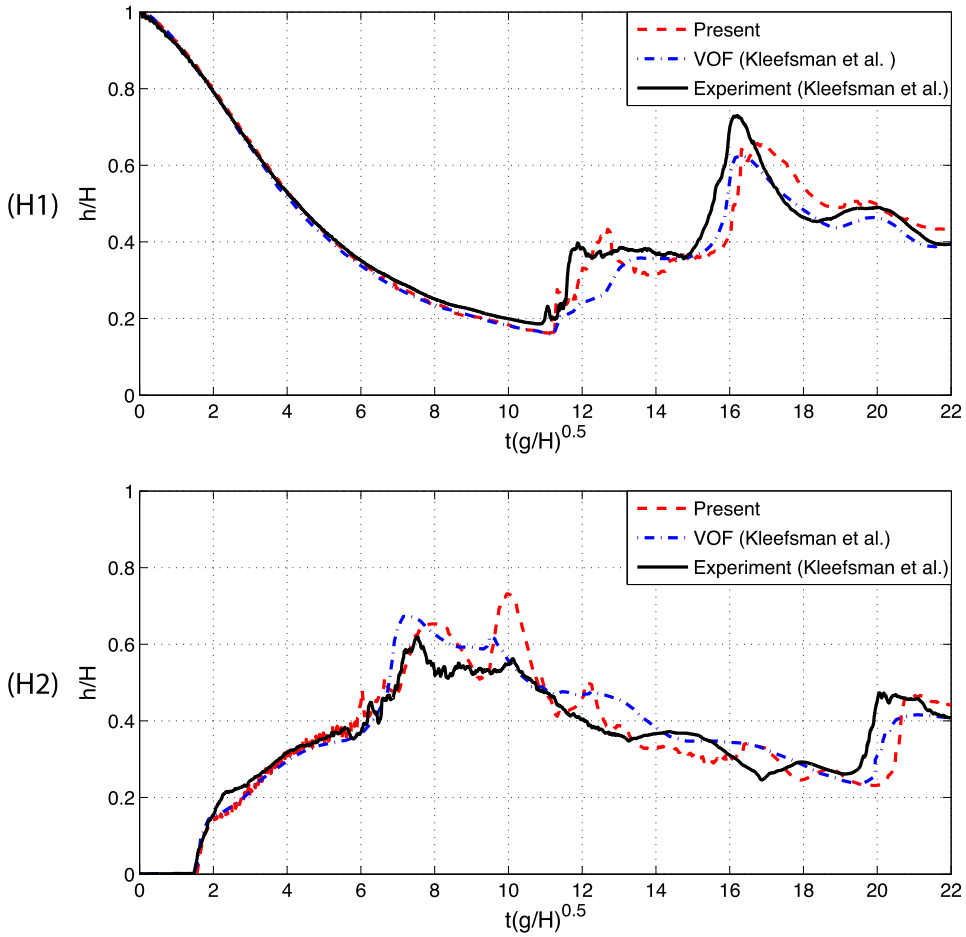

Fig. 16. History of free-surface level recorded at $H1$ and $H2$. Comparison with experimental data and numerical results with VOF method from Kleefsman et al. [44].

where E_{kin} is the kinetic energy, E_{pot} the potential energy, E^0_{pot} the initial potential energy and E^∞_{pot} the potential energy when the flow reaches a hydrostatic state finally. Fig. 9 shows ΔE obtained with increasing particle resolution. It is observed that, while in good agreement with those of Marrone et al. [37], the present results show slightly higher dissipation before the impact but considerably less at later time for the computations with the same particle resolution, see Fig. 9(b). Note that Marrone et al. [37] use a Gaussian kernel with a support radius of $4.5dp$ (shown in their Fig. A31), which leads to much larger number of neighbor particles and higher computational cost.

3.4. Three-dimensional dam-break problem

We test a three-dimensional dam-break problem which is also studied in experiments [41,39,40,42] and numerical simulations [20,43]. Following the experimental setup of Lobovsky et al. [41], the configuration is given in Fig. 10. There are three measurement points $H1$, $H2$ and $H3$ for recording the height of free surface and three probes $P1$, $P2$ and $P3$ for recording the pressure signals.

Fig. 11 gives several snapshots at different time in stances which show the evolution of the free surface. The main features are similar to that obtained in the previous section and are in good agreement with experimental [41] and previous numerical results [20]. Note that the present method produces quite smooth pressure fields even when intensive impact and splashing events occur. The water level is recorded at $H1$, $H2$ and $H3$ are compared with the experiment [41] in Fig. 12. It is observed that, the present results generally are in agreement with the experiment. Note that the simulation predicts a slightly faster wave front and a considerably higher run-up waves, especially when the spatial resolution is high. Such discrepancies also have been found in previous studies such as in Ref. [20] and probably due to the inviscid model used in the simulations. Also note that the water level at $H1$ obtained with high-resolution simulation shows some oscillations after $t = 8$ due to the particle splashing. The history of pressure signals recorded at $P1$, $P2$ and $P3$ are shown in Fig. 13. Generally the present results agree well with the experiment [41] except for the signal at $P3$, which also may be due to the inviscid model. Compared with the two-dimensional results from [43], the present results show much less fluctuations at later times during the entry of plunging breaker.

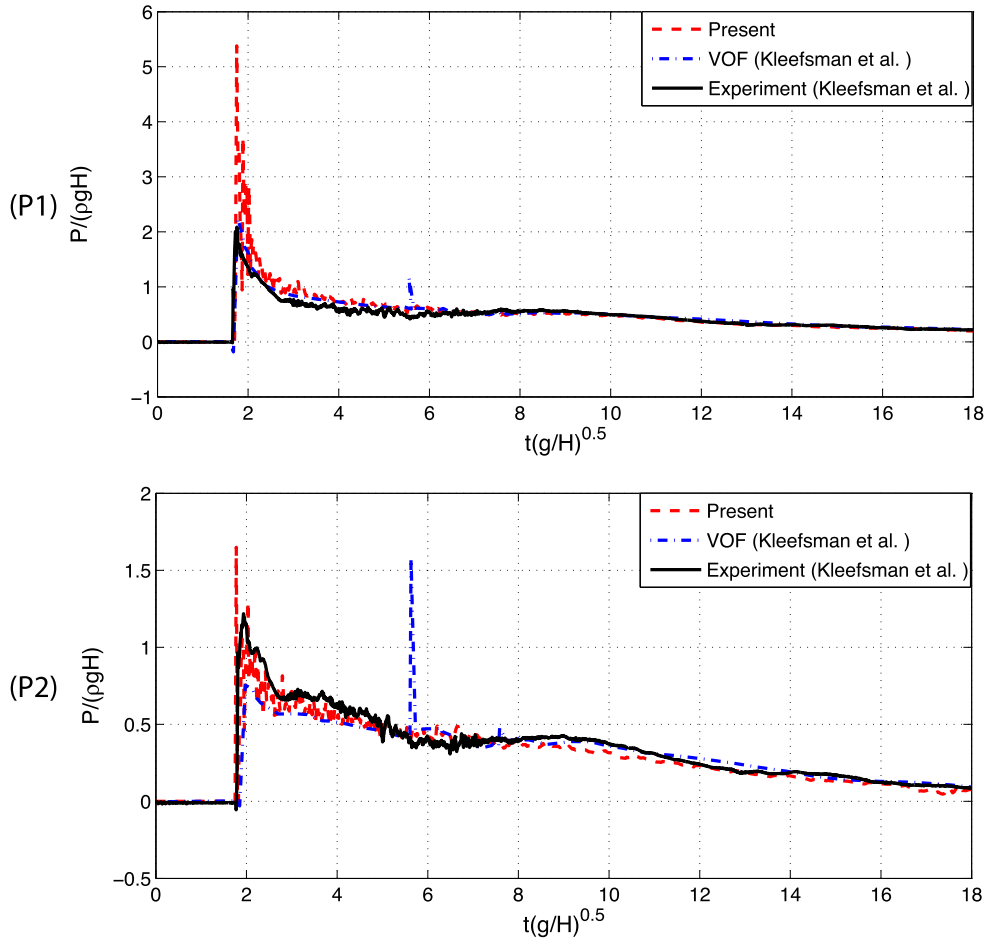

Fig. 17. History of pressure signals recorded at probes $P1$ and $P2$ located at the obstacle. Comparison with experimental data and numerical results with VOF method from Kleefsman et al. [44].

3.5. Three-dimensional dam break with an obstacle

We consider a three-dimensional dam-break problem with a cuboidal obstacle placed on the downstream horizontal bed. This test case was first simulated by Kleefsman et al. [44] with an Eulerian volume-of-fluid (VOF) method, then by Lee et al. [45] with the standard WCSPH and incompressible SPH (ISPH) method, and by δ-SPH [37]. The computational domain and measurement positions are briefly described in Fig. 14. There are water-level measuring points $H1$ and $H2$ and pressure recording probes $P1$ and $P2$ located at the front surface of the obstacle. To discretize the computational domain, the initial particle space is set as $dp = H/36$.

Fig. 15 shows the snapshots of free-surface profile colored by the pressure field at several time stances. The present free-surface profiles are in good agreement with experiment and the numerical results in Ref. [44] and previous simulations in Refs. [45,37]. Note that a splash-up is produced after the surge waves impacts the obstacle which is in agreement with the experimental observation [44].

Fig. 16 shows the history of water level recorded at $H1$ and $H2$. Again, being in general agreement with the experiment the simulation over-predicts the run-up and water level peak, due to the inviscid model. Note that the first reflected wave observed in the experiment at $H2$ and $t = 12$, is reproduced by present simulation but smeared entirely by the VOF simulation. The history of pressure signals recorded by probes $P1$ and $P2$ are shown in Fig. 17. The present results show a good agreement with averaged experimental data, except for the first peak. Note that the VOF method predicts a pressure peak around $t = 5.8$ which is not found by either the present method or the experiment. Note that the results of Ref. [45] show that standard WCSPH results in strong pressure fluctuations and that ISPH is unable to capture the pressure peak when the surge wave impacts at the obstacle.

4. Conclusions

In this paper we have proposed a weakly compressible SPH method based a low-dissipation Riemann solver for modeling free-surface flow problems with violent wave-breaking and impact events. A simple limiter is proposed to reduce the intrinsic numerical dissipation of the Riemann solver and a wall-boundary condition by applying one-sided Riemann problem is developed. The present method is compatible with the hydrostatic solution and produces very small damping of mechanical

energy. Extensive numerical examples show that without tuning parameters the method is able to resolve violent wave breaking and impact events accurately, produces smooth pressure fields and predicts reasonable pressure peaks. It is noted that the present Riemann solver is based on a 1st-order construction only. The application of higher-order reconstruction, which may lead to even less numerical dissipation, will be studied in the future work.

Acknowledgements

The first author is partially supported by the China Scholarship Council (No. 2011623002) and we acknowledge the work of Sbalzarini et al. [46] who provide the Parallel Particle Mesh (PPM) Library that we used to implement our model and enables to perform large-scale simulations on parallel computer architectures.

References

[1] L.B. Lucy, A numerical approach to the testing of the fission hypothesis, Astron. J. 82 (1977) 1013–1024.
[2] R.A. Gingold, J.J. Monaghan, Smoothed particle hydrodynamics: theory and application to non-spherical stars, Mon. Not. R. Astron. Soc. 181 (3) (1977) 375–389.
[3] J.J. Monaghan, SPH without a tensile instability, J. Comput. Phys. 159 (2) (2000) 290–311.
[4] J.P. Gray, J.J. Monaghan, R.P. Swift, SPH elastic dynamics, Comput. Methods Appl. Mech. Eng. 190 (49) (2001) 6641–6662.
[5] P.W. Randles, L.D. Libersky, Smoothed particle hydrodynamics: some recent improvements and applications, Comput. Methods Appl. Mech. Eng. 139 (1) (1996) 375–408.
[6] J.J. Monaghan, Simulating free surface flows with SPH, J. Comput. Phys. 110 (2) (1994) 399–406.
[7] J.P. Morris, P.J. Fox, Y. Zhu, Modeling low Reynolds number incompressible flows using SPH, J. Comput. Phys. 136 (1) (1997) 214–226.
[8] X.Y. Hu, N.A. Adams, A multi-phase SPH method for macroscopic and mesoscopic flows, J. Comput. Phys. 213 (2) (2006) 844–861.
[9] X.Y. Hu, N.A. Adams, An incompressible multi-phase SPH method, J. Comput. Phys. 227 (1) (2007) 264–278.
[10] S. Adami, X.Y. Hu, N.A. Adams, A generalized wall boundary condition for smoothed particle hydrodynamics, J. Comput. Phys. 231 (21) (2012) 7057–7075.
[11] C. Antoci, M. Gallati, S. Sibilla, Numerical simulation of fluid–structure interaction by SPH, Comput. Struct. 85 (11) (2007) 879–890.
[12] M.B. Liu, G.R. Liu, Smoothed particle hydrodynamics (SPH): an overview and recent developments, Arch. Comput. Methods Eng. 17 (1) (2010) 25–76.
[13] J.J. Monaghan, Smoothed particle hydrodynamics and its diverse applications, Annu. Rev. Fluid Mech. 44 (2012) 323–346.
[14] E.-S. Lee, C. Moulinec, R. Xu, D. Violeau, D. Laurence, P. Stansby, Comparisons of weakly compressible and truly incompressible algorithms for the sph mesh free particle method, J. Comput. Phys. 227 (18) (2008) 8417–8436.
[15] M. Antuono, A. Colagrossi, S. Marrone, Numerical diffusive terms in weakly-compressible SPH schemes, Comput. Phys. Commun. 183 (12) (2012) 2570–2580.
[16] J.J. Monaghan, R.A. Gingold, Shock simulation by the particle method SPH, J. Comput. Phys. 52 (2) (1983) 374–389.
[17] A. Colagrossi, M. Landrini, Numerical simulation of interfacial flows by smoothed particle hydrodynamics, J. Comput. Phys. 191 (2) (2003) 448–475.
[18] J.P. Vila, On particle weighted methods and smooth particle hydrodynamics, Math. Models Methods Appl. Sci. 9 (02) (1999) 161–209.
[19] B.B. Moussa, On the convergence of SPH method for scalar conservation laws with boundary conditions, Methods Appl. Anal. 13 (1) (2006) 29–62.
[20] A. Ferrari, M. Dumbser, E.F. Toro, A. Armanini, A new 3D parallel SPH scheme for free surface flows, Comput. Fluids 38 (6) (2009) 1203–1217.
[21] J.J. Monaghan, SPH and Riemann solvers, J. Comput. Phys. 136 (2) (1997) 298–307.
[22] S.I. Inutsuka, Reformulation of smoothed particle hydrodynamics with Riemann solver, J. Comput. Phys. 179 (1) (2002) 238–267.
[23] A.N. Parshikov, S.A. Medin, Smoothed particle hydrodynamics using interparticle contact algorithms, J. Comput. Phys. 180 (1) (2002) 358–382.
[24] K. Puri, P. Ramachandran, A comparison of SPH schemes for the compressible Euler equations, J. Comput. Phys. 256 (2014) 308–333.
[25] S.-H. Cha, S.-i. Inutsuka, S. Nayakshin, Kelvin–Helmholtz instabilities with Godunov smoothed particle hydrodynamics, Mon. Not. R. Astron. Soc. 403 (3) (2010) 1165–1174.
[26] S. Borgani, G. Murante, R. Brunino, S.-H. Cha, Hydrodynamic simulations with the Godunov SPH, in: Advances in Computational Astrophysics: Methods, Tools, and Outcome, vol. 453, 2012, p. 259.
[27] K. Iwasaki, S.-i. Inutsuka, Smoothed particle magnetohydrodynamics with a Riemann solver and the method of characteristics, Mon. Not. R. Astron. Soc. 418 (3) (2011) 1668–1688.
[28] D. Molteni, A. Colagrossi, A simple procedure to improve the pressure evaluation in hydrodynamic context using the SPH, Comput. Phys. Commun. 180 (6) (2009) 861–872.
[29] M. Antuono, A. Colagrossi, S. Marrone, D. Molteni, Free-surface flows solved by means of SPH schemes with numerical diffusive terms, Comput. Phys. Commun. 181 (3) (2010) 532–549.
[30] E.F. Toro, Riemann Solvers and Numerical Methods for Fluid Dynamics: A Practical Introduction, Springer Science & Business, Media, 2009.
[31] F. Dubois, 3.1 partial Riemann problem, boundary conditions, and gas dynamics, in: Absorbing Boundaries and Layers, Domain Decomposition Methods: Applications to Large Scale Computers, 2001, p. 16.
[32] S. Marrone, A. Colagrossi, D. Le Touzé, G. Graziani, Fast free-surface detection and level-set function definition in SPH solvers, J. Comput. Phys. 229 (10) (2010) 3652–3663.
[33] J.J. Monaghan, Smoothed particle hydrodynamics, Rep. Prog. Phys. 68 (8) (2005) 1703.
[34] S. Adami, X.Y. Hu, N.A. Adams, A transport-velocity formulation for smoothed particle hydrodynamics, J. Comput. Phys. 241 (2013) 292–307.
[35] H. Wendland, Piecewise polynomial, positive definite and compactly supported radial functions of minimal degree, Adv. Comput. Math. 4 (1) (1995) 389–396.
[36] A. Ritter, Die Fortpflanzung de Wasserwellen, Z. Ver. Dtsch. Ing. 36 (33) (1892) 947–954.
[37] S. Marrone, M. Antuono, A. Colagrossi, G. Colicchio, D. Le Touzé, G. Graziani, δ-SPH model for simulating violent impact flows, Comput. Methods Appl. Mech. Eng. 200 (13) (2011) 1526–1542.
[38] M. Greco, A Two-Dimensional Study of Green–Water Loading, Ph.D. thesis, Fakultet for ingeniørvitenskap og teknologi, 2001.
[39] B. Buchner, Green Water on Ship-Type Offshore Structures, Ph.D. thesis, TU Delft, Delft University of Technology, 2002.
[40] J.C. Martin, W.J. Moyce, Part IV. An experimental study of the collapse of liquid columns on a rigid horizontal plane, Philos. Trans. R. Soc., Math. Phys. Eng. Sci. 244 (882) (1952) 312–324.
[41] L. Lobovskỳ, E. Botia Vera, F. Castellana, J. Mas-Soler, A. Souto Iglesias, Experimental investigation of dynamic pressure loads during dam break, J. Fluids Struct. 48 (2014) 407–434.
[42] T.-h. Lee, Z. Zhou, Y. Cao, Numerical simulations of hydraulic jumps in water sloshing and water impacting, J. Fluids Eng. 124 (1) (2002) 215–226.
[43] J.L. Cercos-Pita, Aquagpusph, a new free 3d sph solver accelerated with opencl, Comput. Phys. Commun. 192 (2015) 295–312.

[44] K.M.T. Kleefsman, G. Fekken, A.E.P. Veldman, B. Iwanowski, B. Buchner, A volume-of-fluid based simulation method for wave impact problems, J. Comput. Phys. 206 (1) (2005) 363–393.
[45] E.S. Lee, D. Violeau, R. Issa, S. Ploix, Application of weakly compressible and truly incompressible SPH to 3-D water collapse in waterworks, J. Hydraul. Res. 48 (S1) (2010) 50–60.
[46] I.F. Sbalzarini, J.H. Walther, M. Bergdorf, S.E. Hieber, E.M. Kotsalis, P. Koumoutsakos, PPM – a highly efficient parallel particle – mesh library for the simulation of continuum systems, J. Comput. Phys. 215 (2) (2006) 566–588.

A.2 Paper II

Chi Zhang, G. M. Xiang, B. Wang, Xiangyu Y. Hu, Nikolaus A. Adams

A weakly compressible SPH method with WENO reconstruction

In *Journal of Computational Physics*, Volume 392, 2019, pp. 1-18, DOI: `https://doi.org/10.1016/j.jcp.2019.04.038`.

Contribution: My contribution to this work was the development of the method and the corresponding computer code for its implementation. I performed simulations and analyzed the results, and wrote the manuscript for the publication.

Journal of Computational Physics 392 (2019) 1–18

Contents lists available at ScienceDirect

Journal of Computational Physics

www.elsevier.com/locate/jcp

A weakly compressible SPH method with WENO reconstruction

C. Zhang [a], G.M. Xiang [b], B. Wang [b], X.Y. Hu [a,*], N.A. Adams [a]

[a] Department of Mechanical Engineering, Technical University of Munich, 85748 Garching, Germany
[b] School of Aerospace, Tsinghua University, 100084 Beijing, China

ARTICLE INFO

Article history:
Received 10 January 2018
Received in revised form 26 March 2019
Accepted 15 April 2019
Available online 19 April 2019

Keywords:
Smoothed particle hydrodynamics (SPH)
Riemann solver
WENO reconstruction
Free-surface flows

ABSTRACT

In this work, we improve a weakly-compressible SPH method which is based on our previous work of Zhang et al. (2017) [30] by employing a weighted essentially non-oscillatory (WENO) reconstruction. The key idea is to construct along each interacting particle pair a 4-point stencil and to apply a WENO reconstruction for determining the particle interaction with a low-dissipation Riemann solver. Several numerical examples on Taylor-Green vortex flow, dam break and non-linear liquid sloshing demonstrate that the method preserves the capability of producing smooth and accurate pressure fields of the original method and now achieves also very small numerical dissipation.

1. Introduction

Smoothed particle hydrodynamics (SPH) is a purely mesh-free Lagrangian method developed by Lucy [1], Gingold and Monaghan [2] for astrophysical applications. Since these pioneering works, the SPH method has been successfully applied for numerical simulations of solid mechanics [3–5], fluid dynamics [6–10] and fluid-structure interactions [11]. Different SPH algorithms that have been developed recently are comprehensively reviewed in Refs. [12–14].

The weakly-compressible SPH (WCSPH) method, which assumes that the fluid is weakly compressible with controlled density variation [6,7], is widely applied for computing hydrodynamic problems. In order to stabilize simulations involving violent free-surface wave breaking and impacting, very often artificial viscosity is added to the discretized momentum equation [15,16]. Similarly to introducing implicit numerical dissipation by Eulerian Godunov-methods [17], Vila [18] proposed to determine the interaction by solving a Riemann problem along interacting particle pair. While this Riemann-solver based method originally has been proposed for computing compressible flow [19–23], it also has been applied to the WCSPH simulation of hydrodynamic problems [24–26]. It is found that this method, in the latter case, generally exhibits excessive numerical dissipation compared with that based on artificial viscosity, and does not reliably reproduce violent free-surface flows [27,28].

The issue of numerical dissipation has been addressed before by the artificial-diffusion methods [27,29] which add artificial density diffusion in the discretized continuity equation other than implement the traditional Riemann-solvers directly. They introduced, however, another problem of incompatibility with the hydrostatic solution. Recently, we have proposed a simple low-dissipation Riemann solver to decrease numerical dissipation [30]. Without resorting to the computationally elaborate corrections [31], this solver is compatible with the hydrostatic solution.

* Corresponding author.
E-mail address: xiangyu.hu@tum.de (X.Y. Hu).

https://doi.org/10.1016/j.jcp.2019.04.038
0021-9991/

High-order reconstruction used in Eulerian Godunov-method is able to achieve higher accuracy and less numerical dissipation [32]. For this reason, it has also been explored with Riemann-solver based SPH methods. While earlier implementations use second-order linear reconstructions, such as the MUSCL scheme [18,19,33,34], more recent attempts have been aimed at higher-order, such as weighted essentially non-oscillatory (WENO), reconstructions. Zhang et al. [35] have considered a fifth-order WENO reconstruction for computing one-dimensional problems, the multidimensional extension, however, is not straightforward. The first WENO reconstruction for computing multi-dimensional problems is proposed by Avesani et al. [36], in which the directionally-biased multi-dimensional candidate stencils with high-order Moving-Least-Squares (MLS) reconstructions are combined with the WENO weighting strategy. Although this method achieves higher accuracy than those using linear reconstructions, it exhibits much lower computational efficiency due to a large number of multi-dimensional candidate-stencil evaluations. Nogueira et al. [37] proposed a SPH-MOOD-MLS method which uses a MLS-based approximation and a *posteriori* Multidimensional Optimal Order Detection (MOOD) approach for numerical stability. This method shows considerable improvement for modeling compressible flows with shock and blast waves. We point out that several approaches, e.g., reproducing kernel particle method (RKPM) [38], corrective smoothed particle method (CSPM) [39], decoupled finite particle method (DFPM) [40], have been developed to improve accuracy and consistency of the SPH method.

In this paper we propose a simple and computationally efficient WENO reconstruction to increase accuracy and to decrease numerical dissipation for multi-dimensional WCSPH simulation of hydrodynamic problems. Similarly to Avesani et al. [36], the main objective of applying the WENO reconstruction here is to increase accuracy by decreasing the numerical dissipation other than increasing the formal approximation order of the SPH method, which depends on many factors and is quite difficult to achieve in practice. It is shown that a general SPH method applying Gaussian-like kernel achieves only 2nd-order convergence even when the integration error is sufficiently small [41,42]. The construction is applied to the low-dissipation Riemann solver of Ref. [30]. The proposed WENO construction does not apply multi-dimensional candidate stencils [36]. Rather it operates in a one-dimensional fashion along each interacting particle pair, similarly as that used for MUSCL reconstructions [18]. To test the robustness and accuracy of the reconstruction, a number of two and three-dimensional tests, including the Taylor-Green vortex flow and several dam-break problems, are carried out, and the results are compared to analytical solutions and data from literature.

2. Method

The conservation of mass and momentum in the Lagrangian frame for inviscid flow can be written as

$$\frac{\mathrm{d}\rho}{\mathrm{d}t} = -\rho\nabla\cdot\mathbf{v}, \tag{1}$$

$$\frac{\mathrm{d}\mathbf{v}}{\mathrm{d}t} = -\frac{1}{\rho}\nabla P, \tag{2}$$

where ρ is density, $\mathbf{v}$ is velocity, t is time, P is pressure and $\frac{\mathrm{d}}{\mathrm{d}t} = \frac{\partial}{\partial t} + \mathbf{v}\cdot\nabla$ refers to the material derivative. Applying the weakly compressible assumption, the fluid pressure is evaluated through density from an artificial equation of state

$$P = c_0^2(\rho - \rho_0), \tag{3}$$

where $c_0 = 10V_{max}$ is the speed of sound and V_{max} represents the maximum anticipated velocity inside the flow.

2.1. Riemann-solver based WCSPH method

Similarly to previous work on Riemann-solver based WCSPH methods [18–20,30], Eqs. (1) and (2) can be discretized as

$$\frac{\mathrm{d}\rho_i}{dt} = 2\rho_i\sum_j \frac{m_j}{\rho_j}(\mathbf{v}_i - \mathbf{v}^*)\cdot\nabla_i W_{ij} = 2\rho_i\sum_j \frac{m_j}{\rho_j}(U_i - U^*)\frac{\partial W_{ij}}{\partial r_{ij}}, \tag{4}$$

$$\frac{\mathrm{d}\mathbf{v}_i}{dt} = -2\sum_j m_j\frac{P^*}{\rho_i\rho_j}\nabla_i W_{ij}. \tag{5}$$

Here, m is particle mass, $\nabla_i W_{ij} = \frac{\partial W_{ij}}{\partial r_{ij}}\mathbf{e}_{ij}$ is the gradient of kernel function with respect to particle i, where, as shown in Fig. 1, $\mathbf{e}_{ij}$ is the unit vector pointing form particle i to particle j, and r_{ij} is the distance between them. $U_i = \mathbf{v}_i\cdot\mathbf{e}_{ij}$ and $U^* = \mathbf{v}^*\cdot\mathbf{e}_{ij}$. Note that U^* and P^* are the solution of the inter-particle Riemann problem constructed at the mid-point of particle i and j as shown in Fig. 1.

In this Riemann problem the discontinuous left and right states, i.e. (ρ_L, U_L, P_L) and (ρ_R, U_R, P_R), are assigned to each side of the mid point. We apply the low-dissipation Riemann solver [30]

$$\begin{cases} U^* = \overline{U} + \frac{1}{2}\frac{(P_L - P_R)}{\overline{\rho}c_0} \\ P^* = \overline{P} + \frac{1}{2}\overline{\rho}c_0\beta(U_L - U_R) \end{cases}, \tag{6}$$

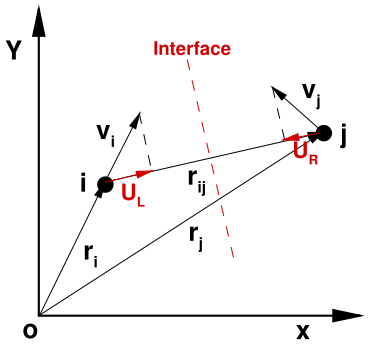

Fig. 1. Construction of Riemann problem along the interacting line of particles i and j.

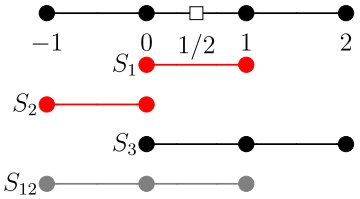

Fig. 2. Full stencil and candidate stencils, i.e. $S_k, k = 1, 2, 3$, for the incremental-stencil WENO reconstruction of $q_{1/2}$. Note that S_1 and S_2 are subsets of the original stencil S_{12} for WENO-JS reconstruction [45].

where $\overline{\rho} = (\rho_L + \rho_R)/2$, $\overline{U} = (U_L + U_R)/2$ and $\overline{P} = (P_L + P_R)/2$ and $\beta = \min\left(3\max\left[(U_L - U_R, 0)/c_0, 1\right]\right.$ is a numerical dissipation limiter. If the initial states of the Riemann problem are the same as that of particle i and particle j, i.e.

$$(\rho_L, U_L, P_L) = (\rho_i, U_i, P_i), \quad (\rho_R, U_R, P_R) = (\rho_j, U_j, P_j), \tag{7}$$

a piece-wise constant reconstruction (denoted as "Baseline") is applied.

2.2. WENO reconstruction

Based on the concept inherited from the schemes in Refs. [43,44], we introduce a modified WENO reconstruction, by which the full 4-point stencil (4 points with indices from -1 to 2 as shown in Fig. 2), is constructed from a set of small stencils with incremental size. Note that the differences between the present candidate stencils and those in Refs. [43,44] are that the minimum-size stencil here has 2 points and the full stencil 4 points. In the present reconstruction, the mid-point value, i.e. $q_{1/2}$, is predicted by the non-linear weighted average

$$q_{1/2} = \sum_k w_k q_{1/2}^{(k)}, \tag{8}$$

where $q_{1/2}^{(k)}$ and w_k, $k = 1, 2, 3$, are the reconstructed values from the candidate stencils and their non-linear weights. These reconstructed values are

$$\begin{cases} q_{1/2}^{(1)} = \frac{1}{2}q_0 + \frac{1}{2}q_1 \\ q_{1/2}^{(2)} = -\frac{1}{2}q_{-1} + \frac{3}{2}q_0 \\ q_{1/2}^{(3)} = \frac{1}{3}q_0 + \frac{5}{6}q_1 - \frac{1}{6}q_2 \end{cases}. \tag{9}$$

Following Wang et al. [44], the non-linear weights are defined as

$$w_k = \frac{\alpha_k}{\sum_{s=1}^{3}\alpha_s}, \begin{cases} \alpha_1 = d_1\left(1 + \frac{\tau_4}{\beta_1+\varepsilon}\cdot\frac{\tau_4}{\beta_{12}+\varepsilon}\right) \\ \alpha_2 = d_2\left(1 + \frac{\tau_4}{\beta_2+\varepsilon}\cdot\frac{\tau_4}{\beta_{12}+\varepsilon}\right) \\ \alpha_3 = d_3\left(1 + \frac{\tau_4}{\beta_3+\varepsilon}\right) \end{cases}, \tag{10}$$

where the linear weights are determined as $d_1 = 1/3$, $d_2 = 1/6$ and $d_3 = 1/2$. β_k, $k = 1, 2, 3$, and β_{12} are the smoothness indicators for the candidate stencils,

$$\begin{cases} \beta_1 = (q_1 - q_0)^2 \\ \beta_2 = (q_0 - q_{-1})^2 \\ \beta_{12} = \frac{1}{4}(q_{-1} - q_1)^2 + \frac{13}{12}(3q_{-1} - 2q_0 + q_1)^2 \\ \beta_3 = \frac{13}{12}(q_0 - 2q_1 + q_2)^2 + \frac{1}{4}(3q_0 - 4q_1 + q_2)^2 \end{cases}, \tag{11}$$

$\varepsilon = 10^{-6}$ as in WENO-JS, and τ_4 is a global reference smoothness indicator [43] given as

$$\begin{aligned} \tau_4 = [&q_{-1}(547q_{-1} - 2522q_0 + 1922q_1 - 494q_2) \\ &+q_0(3423q_0 - 5966q_1 + 1602q_2) \\ &+q_1(2843q_1 - 1642q_2) \\ &+267q_2]/240. \end{aligned} \tag{12}$$

To implement the modified WENO reconstruction into the SPH method, we construct the 4-point stencil for interacting particle pair, such as particle i and j. For particle i, the values at the stencil points are calculated as

$$\begin{cases} q_{-1} = \Phi_i - \nabla\Phi_i \cdot \boldsymbol{r}_{ij} \\ q_0 = \Phi_i \\ q_1 = \Phi_j \\ q_2 = \Phi_j + \nabla\Phi_j \cdot \boldsymbol{r}_{ij} \end{cases}, \tag{13}$$

where Φ_i and Φ_j represent the primitive values, ρ, P and $\boldsymbol{v} \cdot \mathbf{e}_{ij}$, at particle i and j respectively. Note that $\nabla\Phi_i$ and $\nabla\Phi_j$ are the corresponding gradients calculated from the SPH approximation as

$$\nabla\Phi_i = \sum_j \frac{m_j}{\rho_j}(\Phi_j - \Phi_i)\nabla_i W_{ij}. \tag{14}$$

The left state Φ_L of the Riemann problem for the interacting particle pair of i and j is defined as

$$\Phi_L = q_{1/2}, \tag{15}$$

by applying Eq. (8) based on the 4-point stencil calculated as Eq. (13). The right state Φ_R is also obtained from by Eq. (8), but based on the mirrored stencil given by

$$\begin{cases} q_{-1} = \Phi_j + \nabla\Phi_j \cdot \boldsymbol{r}_{ij} \\ q_0 = \Phi_j \\ q_1 = \Phi_i \\ q_2 = \Phi_i - \nabla\Phi_i \cdot \boldsymbol{r}_{ij} \end{cases}. \tag{16}$$

2.3. Time integration

Following Refs. [46,47], a kick-drift-kick scheme is employed for time advancement. The half time-step velocity is updated first followed by the new time-step particle position by

$$\begin{cases} \mathbf{v}_i^{n+\frac{1}{2}} = \mathbf{v}_i^n + \frac{1}{2}\delta t\left(\frac{d\mathbf{v}_i}{dt}\right)^n \\ \mathbf{r}_i^{n+1} = \mathbf{r}_i^n + \delta t \mathbf{v}_i^{n+\frac{1}{2}} \end{cases}, \tag{17}$$

where the superscript n represents the time step. After that the change rate of density is calculated through the half time-step velocity and the new time-step particle position. The new time-step particle density is updated by

$$\rho_i^{n+1} = \rho_i^n + \delta t\left(\frac{d\rho_i}{dt}\right)^{n+1/2}. \tag{18}$$

Then, the pressure is updated through the equation of state, and the particle force is calculated at the new time-step. Finally, the velocity is updated for the new time step as

$$\mathbf{v}_i^{n+1} = \mathbf{v}_i^{n+\frac{1}{2}} + \frac{1}{2}\delta t\left(\frac{d\mathbf{v}_i}{dt}\right)^{n+1}. \tag{19}$$

For numerical stability, a CFL condition is employed

$$\Delta t \leq \min\left(0.25\frac{h}{c+|U|}, 0.125\frac{h^2}{\nu}, 0.25\sqrt{\frac{h}{|g|}}\right), \tag{20}$$

where $|U|$ is the maximum velocity inside the flow, ν is the kinetic viscosity and $\nu = \mu/\rho$.

3. Numerical examples

In this section, test cases on one dimensional acoustic wave, two- and three-dimensional dam-break, non-linear liquid sloshing and Taylor-Green vortex flow are considered to validate and demonstrate the SPH method with WENO reconstruction (denoted as "WENO-SPH"). The 5th-order Wendland kernel [48] with a smoothing length $h = 1.3dp$, where dp is the initial particle spacing, and a support radius $2.6dp$, are used in hydrodynamic test cases. The physical parameters density $\rho = 1000$ kg/m^3 and gravitational acceleration $g = 9.8$ m/s^2 are applied. For all hydrodynamic cases, the maximum fluid velocity is approximated as $V_{max} = 2\sqrt{gH}$, where H is the initial water depth, according to the shallow-water theory [49], for setting the speed of sound c_0. Water with zero initial pressure is released immediately when the computation starts instead of being released from a gate holding the water column with a hydrostatic pressure field as in the experimental setup. Also note that the Riemann solver with a low-dissipation limiter and the solid boundary treatment in Ref. [30] are applied.

We compare numerical results with those obtained by the baseline scheme in which a piece-wise constant reconstruction is applied [30] (denoted as "Baseline") and a scheme with MUSCL reconstruction [17,50] (denoted as "MUSCL"). In the MUSCL reconstruction [17], the left and right states are reconstructed from

$$\begin{aligned} \Phi_L &= \Phi_i + \tfrac{1}{2}\overline{\Delta\Phi_i} \\ \Phi_R &= \Phi_j - \tfrac{1}{2}\overline{\Delta\Phi_j} \end{aligned}, \tag{21}$$

where $\overline{\Delta\Phi_i}$ and $\overline{\Delta\Phi_j}$ are limited slopes. In a typical SPH formulation [50] the limited slopes are defined as

$$\overline{\Delta\Phi_i}, \overline{\Delta\Phi_j} = \begin{cases} max[0, min(\beta\Delta\Phi_i, \Delta\Phi_j), min(\Delta\Phi_i, \beta\Delta\Phi_j)], \Delta\Phi_j > 0 \\ min[0, max(\beta\Delta\Phi_i, \Delta\Phi_j), max(\Delta\Phi_i, \beta\Delta\Phi_j)], \Delta\Phi_j < 0 \end{cases}, \tag{22}$$

where

$$\begin{cases} \Delta\Phi_i = \bigtriangledown\Phi_i \cdot \mathbf{r}_{ji} \\ \Delta\Phi_j = \bigtriangledown\Phi_j \cdot \mathbf{r}_{ij} \end{cases} \text{ and } \quad \beta = 1.5. \tag{23}$$

Note that many other slope limiters, e.g. Minmod, Superbee, Sweby, which are widely used in Eulerian mesh method [17], may be applied. For example, Iwasaki et al. [33] and Murante et al. [34] use a van Leer slop limiter for modeling compressible MHD flow problems.

3.1. One-dimensional acoustic wave

Following Refs. [51,52], we test the convergence of WENO-SPH with a case of sound-wave propagation. The one-dimensional acoustic wave travels in an ideal gas with $\gamma = 5/3$, unity density $\rho_0 = 1.0$ and sound speed $c = 1.0$ inside a periodic domain. The sound wave is defined by a sinusoidal perturbation

$$\rho_i = \rho_0 + \delta_i, \mathbf{v}_i = c_s\delta_i, p_i = p_0 + \delta_i, \delta_i = Asin(\frac{2\pi x_i}{\lambda}), \tag{24}$$

where $A = 10^6$ and wavelength $\lambda = 1.0$. The background pressure $p_0 = \frac{c_s^2\rho_0}{\gamma} = \frac{3}{5}$ is determined by the ideal gas equation of state. We simulate this case at different resolutions with $N = 32$, 64, 128, 256, 512, and 1024 particles. The L_1 error of density is given as

$$L_1(\rho) = \frac{1}{N}\sum_i |\rho_i - \rho(x_i)|. \tag{25}$$

Here $\rho(x_i)$ is sampled from the analytical solution. Note that using Eq. (4) to evaluate the density, exact consistency between mass and density is not satisfied [53,41]. In order to avoid this problem and demonstrate the formal convergence order of different reconstruction schemes, a fully compressible SPH formulation is applied here with density summation equation (number of neighbors $N_{ngb} = 4$), variable smoothing length and internal energy equation, and an exact Riemann solver as in Refs. [51,52]. Note that the number of neighbors $N_{ngb} = 4$ is consistent with the setup $h = 1.3dp$ in other tests.

Fig. 3 gives the density error, at $t = 1$ when the wave propagated back to the original position, with increasing particle resolution. It is observed that WENO-SPH and MUSCL achieve second-order convergence, which is the formal accuracy of a general SPH method with Gaussian-like smoothing kernels when the particle integration error is negligible [54]. Note that, compared with WENO-SPH, while Baseline achieves first-order convergence only, MUSCL exhibits considerably larger errors due to numerical dissipation.

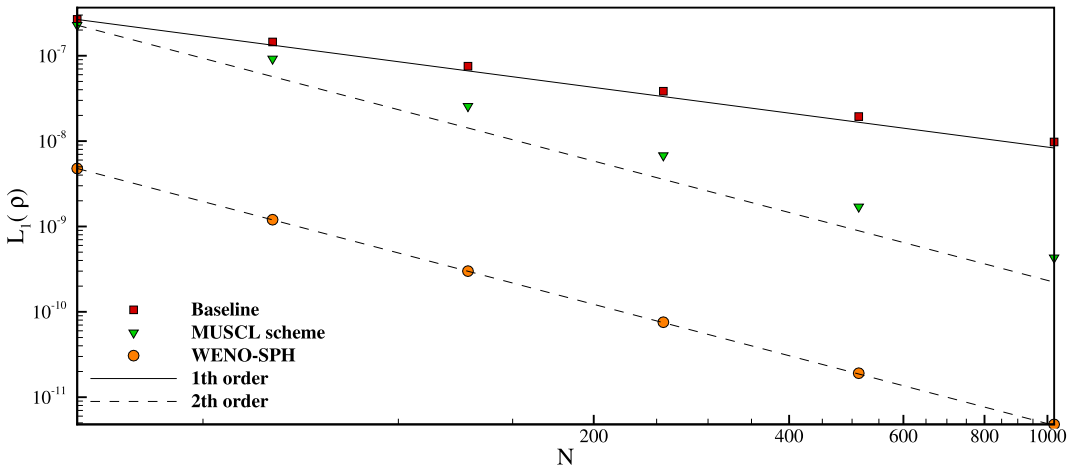

Fig. 3. One dimensional acoustic wave: the convergence of the density error as a function of particle resolution.

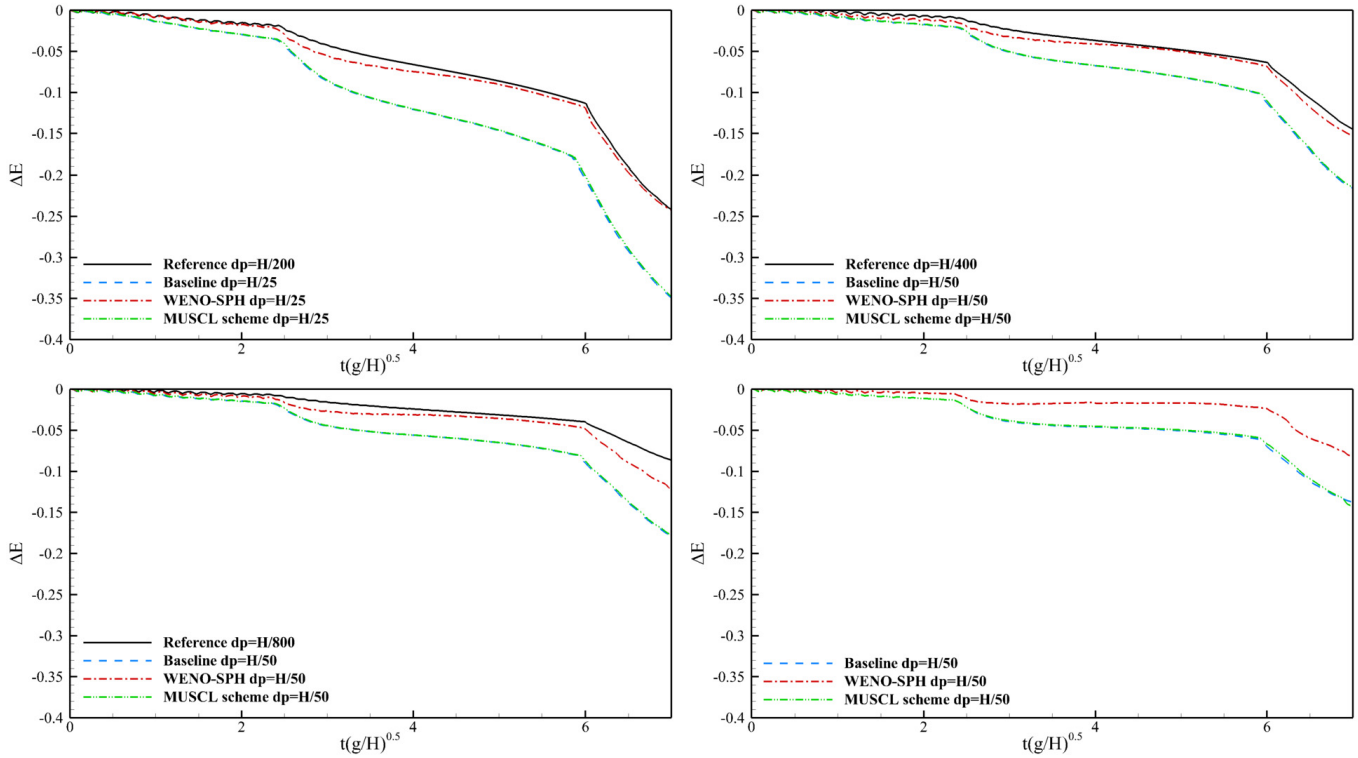

Fig. 4. Two-dimensional dam-break flow: mechanical energy damping obtained by using Baseline, WENO-SPH and MUSCL for $R_e = 400$ (top-left panel), $Re = 800$ (top-right panel), $R_e = 1600$ (bottom-left panel), and inviscid flow (bottom-right panel), respectively.

3.2. Dam-break flows

In this section, we compute several cases of dam-break flow in two- and three-dimensions. These classical test cases are characterized by different evolution stages involving violent free-surface wave impacting, breaking and reconnect.

3.2.1. Two-dimensional dam break

The sketch of the initial configuration is the same as that in Refs. [55,30], where the water column initially covers a rectangle of size $H = 0.6$ and $L = 2H$. The right wall of the tank is located at $L_{wall} = 5.366H$.

Mechanical energy damping can be defined as $\Delta E = (E_{kin} + E_{pot} - E^0)/(E^0 - E^\infty)$, where E_{kin} and E_{pot} are kinetic and potential energies, respectively. E^0 and E^∞ are the initial and final energies, respectively, with the contribution of potential energy only. Three cases with different Reynolds numbers $R_e = 400$, $R_e = 800$ and $R_e = 1600$ are considered. For comparison, the reference energy-damping data are obtained by numerically converged SPH simulations, which are computed with Baseline at much higher resolutions. As shown in Figs. 4 (the top-left, top-right and bottom-left panels), WENO-SPH achieves considerably less numerical dissipation compared to the Baseline and MUSCL. Compared with Baseline,

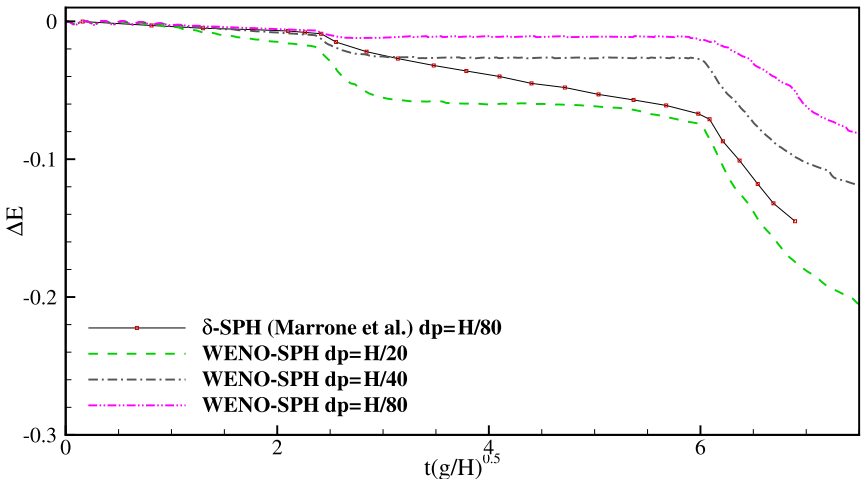

Fig. 5. Two-dimensional dam-break flow: convergence study of mechanical energy damping obtained with WENO-SPH for inviscid flow, and comparison with state of art result by using δ-SPH method.

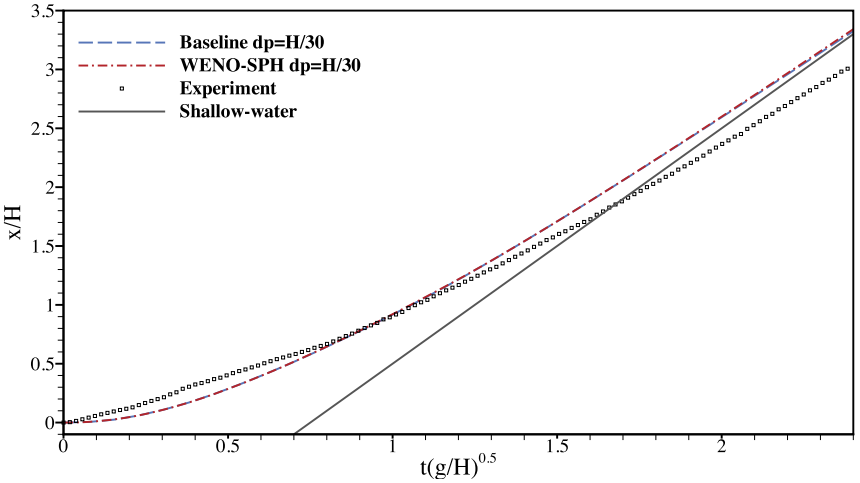

Fig. 6. Three-dimensional dam-break flow: the propagation of the surge-wave front compared with experimental data [57] and analytical solution [49].

MUSCL only slightly decreases the numerical dissipation. Fig. 4 (the bottom-right panel) also gives the numerical damping for the inviscid dam break flow. Again, mechanical energy is better preserved by WENO-SPH. Fig. 5 gives the damping of mechanical energy for the inviscid problem with increasing resolution. It is observed that at the same resolution of $dp = H/80$ the present method has less numerical dissipation than the δ-SPH method. [56]. The results show that MUSCL does not improve notably the energy loss. This can be explained by the fact that, unlike the WENO reconstruction, MUSCL may enforce the zero gradient condition in Eq. (22) too frequently due to very complex flow structures.

3.2.2. Three-dimensional dam break

The setup of this case follows the experimental setup of Lobovsky et al. [57]. We consider a viscous flow with a Reynolds number of $R_e = 3.8 \times 10^6$.

Fig. 6 gives the propagation of the surge wave front compared with experimental data [57] and the analytical solution of shallow-water equation [49]. Similarly with previous SPH simulations [10,55,27,56], both results obtained by Baseline and WENO-SPH agree well with the analytical solution which slightly overestimates the propagation speed. Note that the analytical solution obtained by shallow-water theory is not applicable at the initial time [58]. Fig. 7 shows the recorded water levels and the comparison with experimental data [57]. The numerical results generally are in agreement with the experiment except for a slightly faster wave front propagation and a considerably higher reflected jet. Such discrepancies also have been found in previous studies [27,59] and may be due to wall roughness which is neglected in the simulations. Compared with Baseline, WENO-SPH produces a slightly higher reflected wave due to less damping of mechanical energy. The predicted histories of pressure signals are shown in Fig. 8. Generally, both results agree well with the experimental data [57]. Note that WENO-SPH improves the capability of resolving the first impacting pressure at probe $P3$. The measured losses of mechanical energy (not shown here) for the results computed with Baseline, MUSCL and SPH-WENO resemble that in Fig. 4.

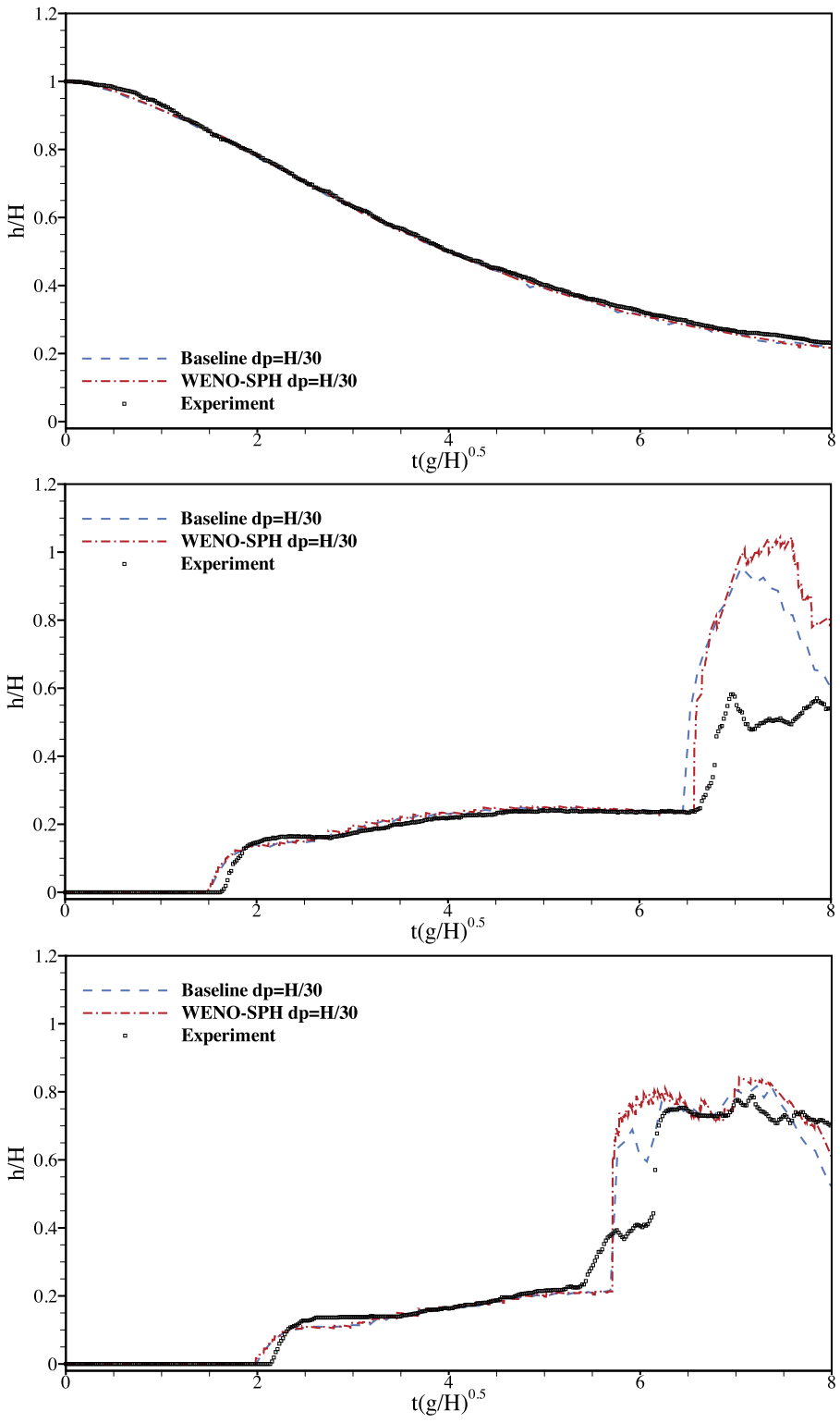

Fig. 7. Three-dimensional dam-break flow: the time histories of free surface recorded at $H1$ (top panel), $H2$ (middle panel) and $H3$ (bottom panel) and comparison against experimental data [57].

3.3. Dam break flow against a sharp-edged obstacle

We compute a two-dimensional inviscid dam break flow impacting at a sharp-edged obstacle according to the setup shown in Fig. 9. This test case is taken from Ref. [60], where the numerical solution is obtained by a finite-difference solver combined with a single-phase level-set method. One pressure probe is placed at the front surface of the obstacle. Note that this test case is also studied by Marrone et al. [56] to validate their δ-SPH method as this case consists of a wave impact which is more violent than previous dam break tests and requires good numerical stability of SPH method.

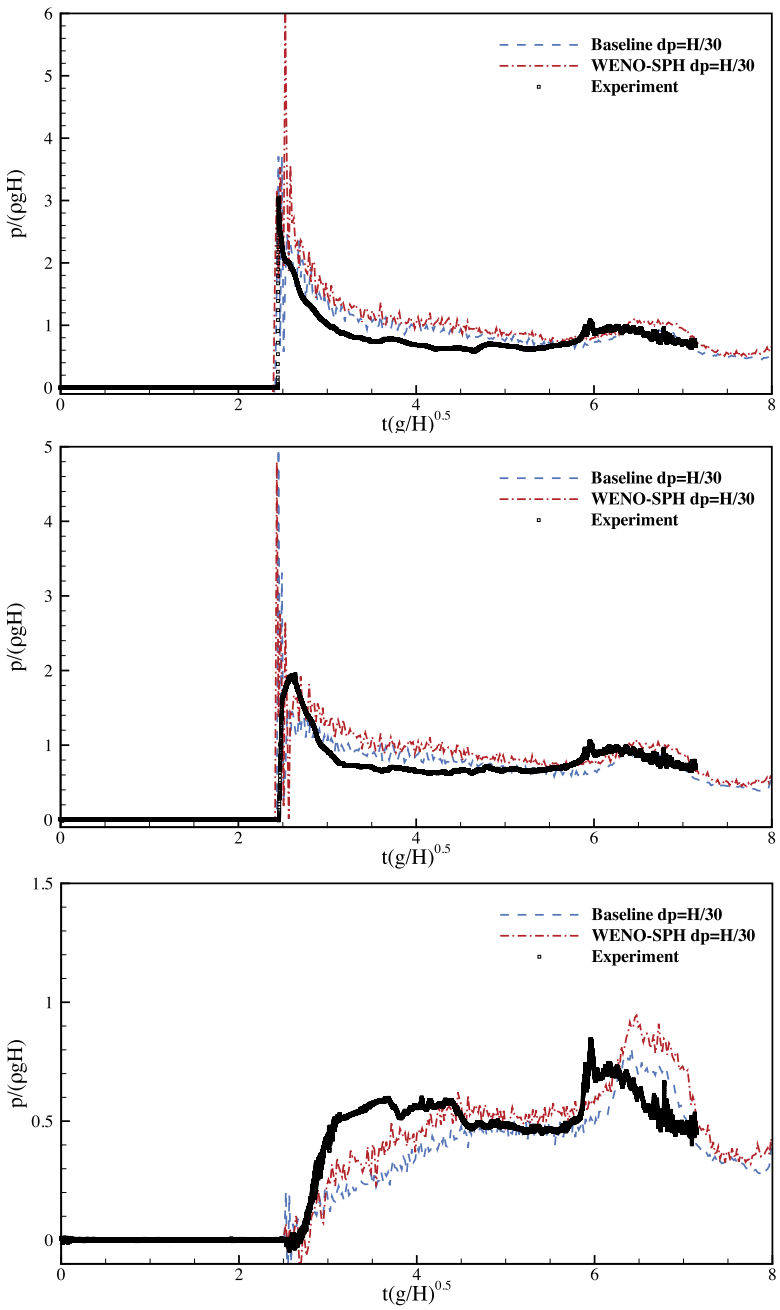

Fig. 8. 3D dam-break flow: the time histories of pressure signals sampled by $P1$ (top panel), $P2$ (middle panel) and $P3$ (bottom panel) and comparison against experimental data [57]. The pressure is sampled every 10 time-steps and averaged from the particles within a radius of $2h$. The same smoothing is also applied to the latter cases.

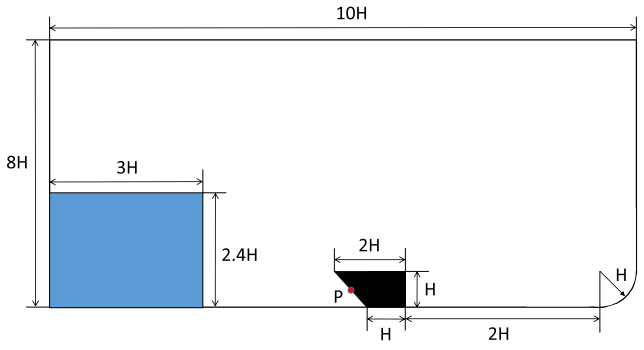

Fig. 9. Dam break flow against a sharp-edged obstacle: the schematic of the initial configuration with a pressure probe located at the midpoint of the front surface of the obstacle.

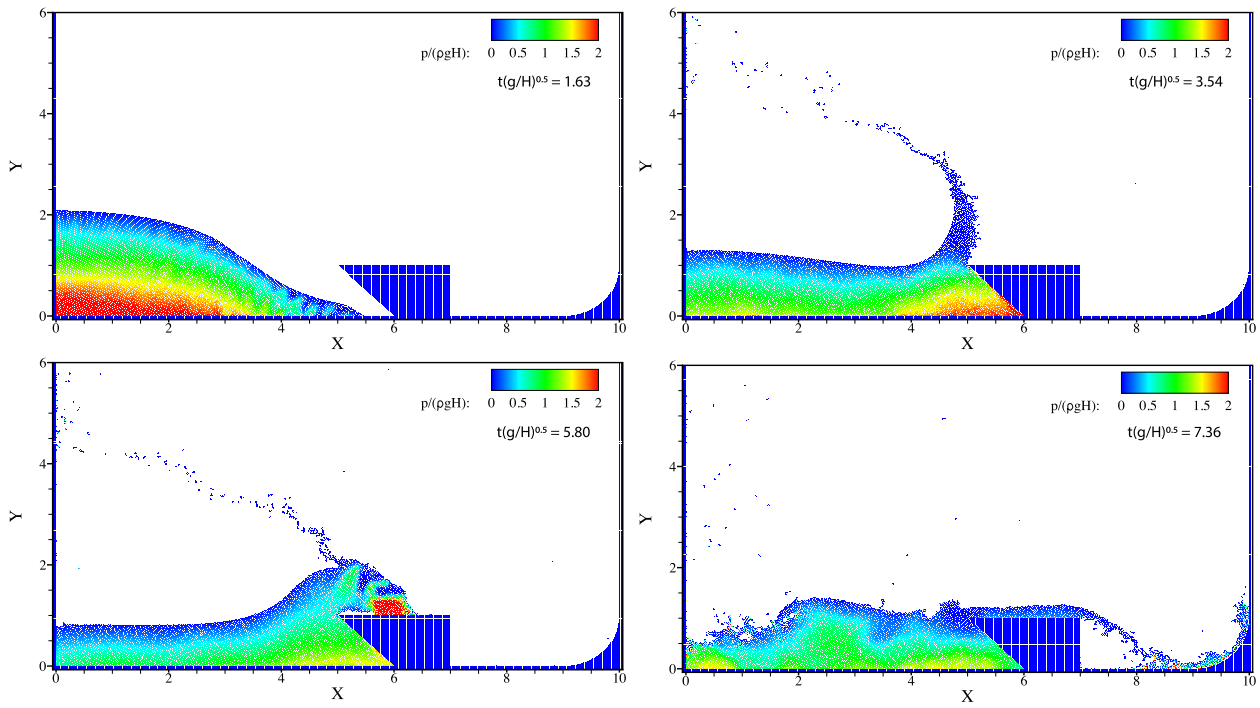

Fig. 10. Dam break flow against a sharp-edged obstacle: snapshots produced by WENO-SPH.

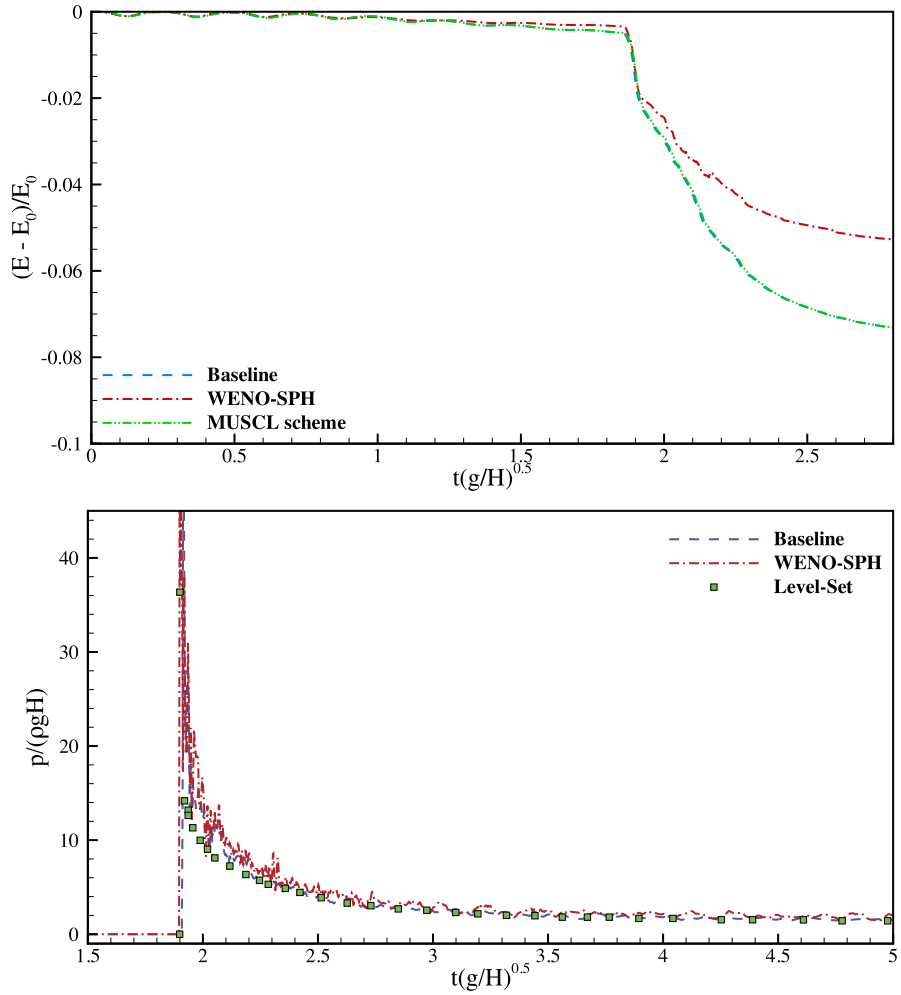

Fig. 11. Dam break flow against a sharp-edged obstacle: the evolution of mechanical energy and the time history of pressure signals sampled by probe P.

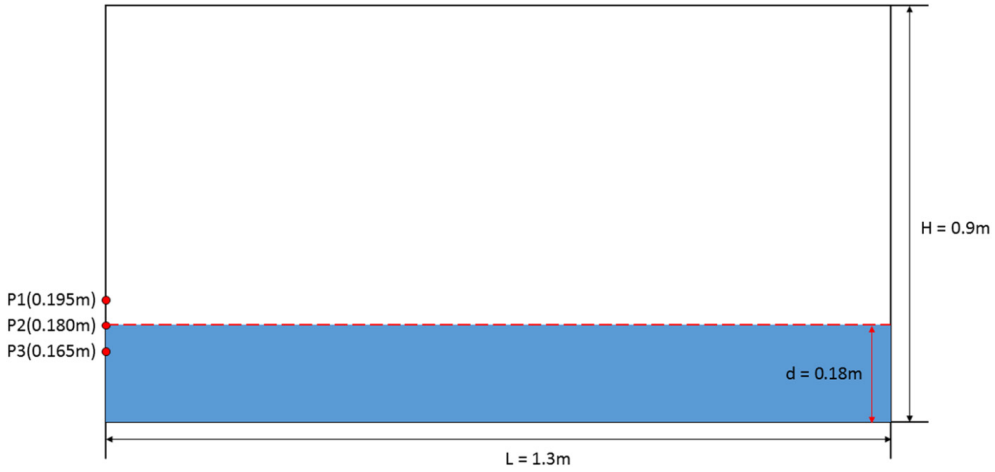

Fig. 12. The schematic of the non-linear liquid sloshing.

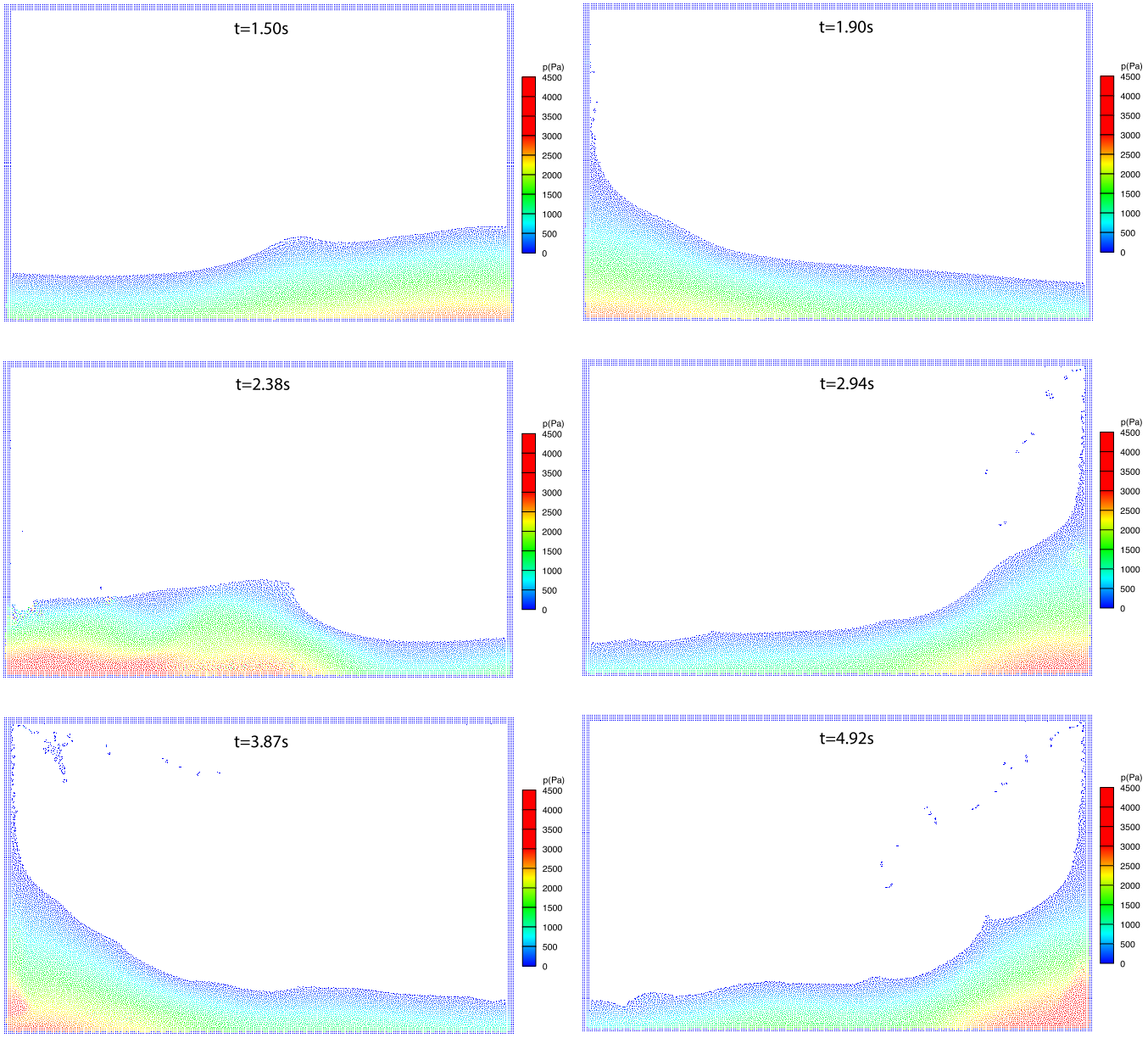

Fig. 13. Snapshots of the non-linear liquid sloshing obtained by WENO-SPH.

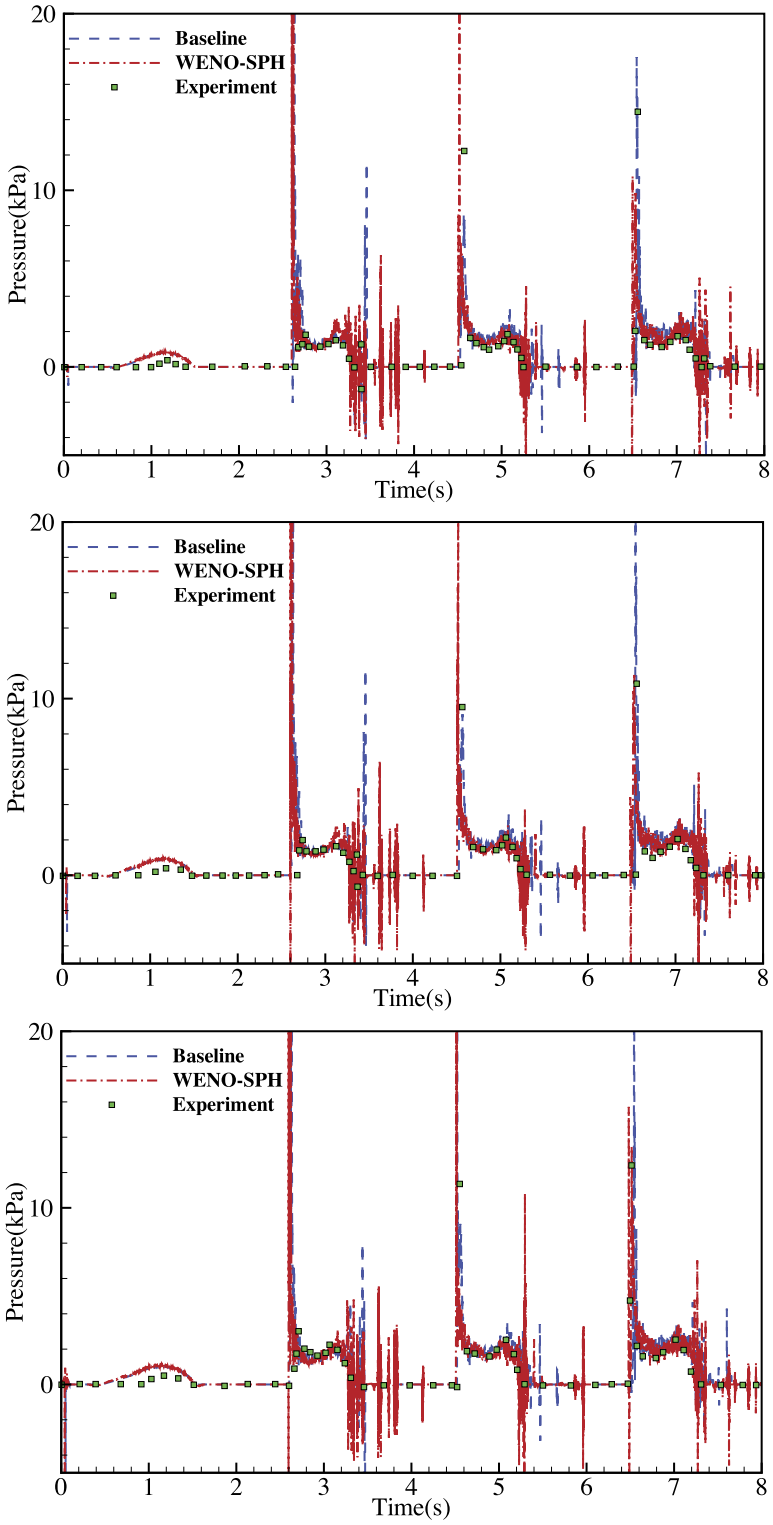

Fig. 14. The time history of pressure signals of the liquid sloshing: $P1$ (top panel), $P2$ (middle panel) and $P3$ (bottom panel).

Fig. 10 shows the snapshots of free-surface at different time instances obtained by WENO-SPH with a spatial resolution of $dp = H/50$. The fluid motion, before impact on the obstacle, is similar to that of typical dam break flow, and is characterized by a violent fluid injection due to the sharp edge as shown in Fig. 10 (top panels). Later, a large reflected jet is generated and impacts at the left wall. After that the flow becomes very complex and the free surface fragments as shown in Fig. 10 (bottom panels). Compared with the results obtained by Marrone et al. [56], a good agreement is noted in reproducing the violent free-surface motion by the present WENO-SPH method. Also note that WENO-SPH shows more small-scale structures (splash) at time instances $t(g/H)^{0.5} = 3.54$ and $t(g/H)^{0.5} = 5.8$ compared with Ref. [56]. Fig. 11 (top panel) gives the evolution of mechanical energy. Compared with Baseline and MUSCL, WENO-SPH produces less damping, especially

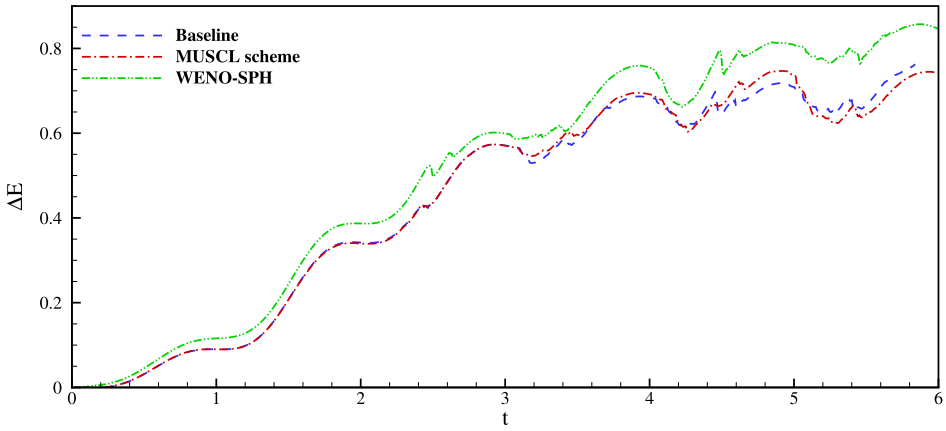

Fig. 15. The evolution of total mechanical energy for the non-linear liquid sloshing problem.

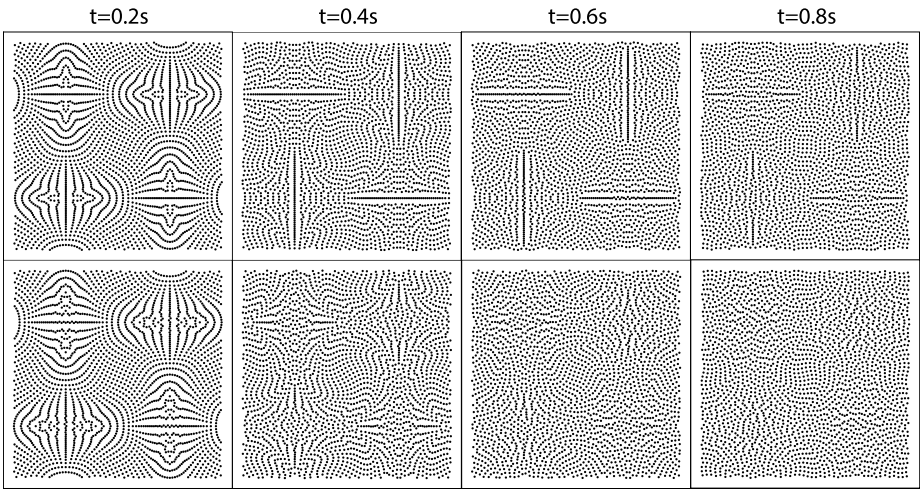

Fig. 16. Snapshots of particle distribution of Taylor-Green vortex flow at $R_e = 100$ with a spatial resolution of $dp = L/50$: Baseline (top panel) and WENO-SPH (bottom panel).

after the flow impacts on the sharp-edged obstacle, which implies considerable less numerical dissipation. Again, it is observed that MUSCL only slightly decreases the numerical dissipation compared to Baseline. Fig. 11 (bottom panel) also gives the time history of pressure signal sampled by probe P, which indicates the results are in good agreement with that in Ref. [60], except for a large magnitude of impact pressure due to the assumption of weakly compressible fluid. Again, the main pressure plateau agrees well with that obtained by δ-SPH method [56].

3.4. Non-linear liquid sloshing

This test case concerns liquid sloshing inside a partially filled tank, which is taken from the experimental study of Rafiee et al. [61]. The resonant sloshing phenomenon, which is highly non-linear and occurs when the tank-motion frequency is close to the natural frequency of the inside fluid, may lead to a very violent free-surface motion and risks structure stability [62].

We consider the non-linear liquid sloshing at a low filling ratio ($d/H = 0.2$), as shown in Fig. 12. A sinusoidal excitation motion of the tank, $x = A_0 \sin(2\pi f_0 t)$, is defined by a large amplitude $A_0 = 0.1$ m and resonance frequency $f_0 = 0.496$ s^{-1}. Similarly to the experimental setup [61], the pressure variations at three locations, as shown in Fig. 12, are recorded. We are computing a viscous flow with the dynamics viscosity $\mu = 1.0 \times 10^{-6}$ kg $\cdot$ m^{-1} $\cdot$ s^{-1}. The particles initially were placed on a regular lattice with spacing $dp = L/260$.

Fig. 13 shows several snapshots of free-surface and particles colored by pressure field during sloshing. After the onset of excitation, a traveling wave with a crest is generated and then subsequently hits the left wall of the tank. The wave climbs up along the left wall and then falls back and results a bore. The bore travels in the tank, breaks and impacts at the right wall and then forming a high run-up. Fig. 14 gives the time history of pressure signals compared with experimental data from Ref. [61]. Generally, all numerically predicted main pressure plateaus are in close agreement with the experimental data, but the maximum pressure peaks are larger than that of the experiment. This discrepancy may be due to the fact that the presence of air phase in the experiment reduces impact pressure. Another reason is associated to the three-dimensional nature of the sloshing flow. Note that there are some fluctuations in the numerical results. These are a consequence of the

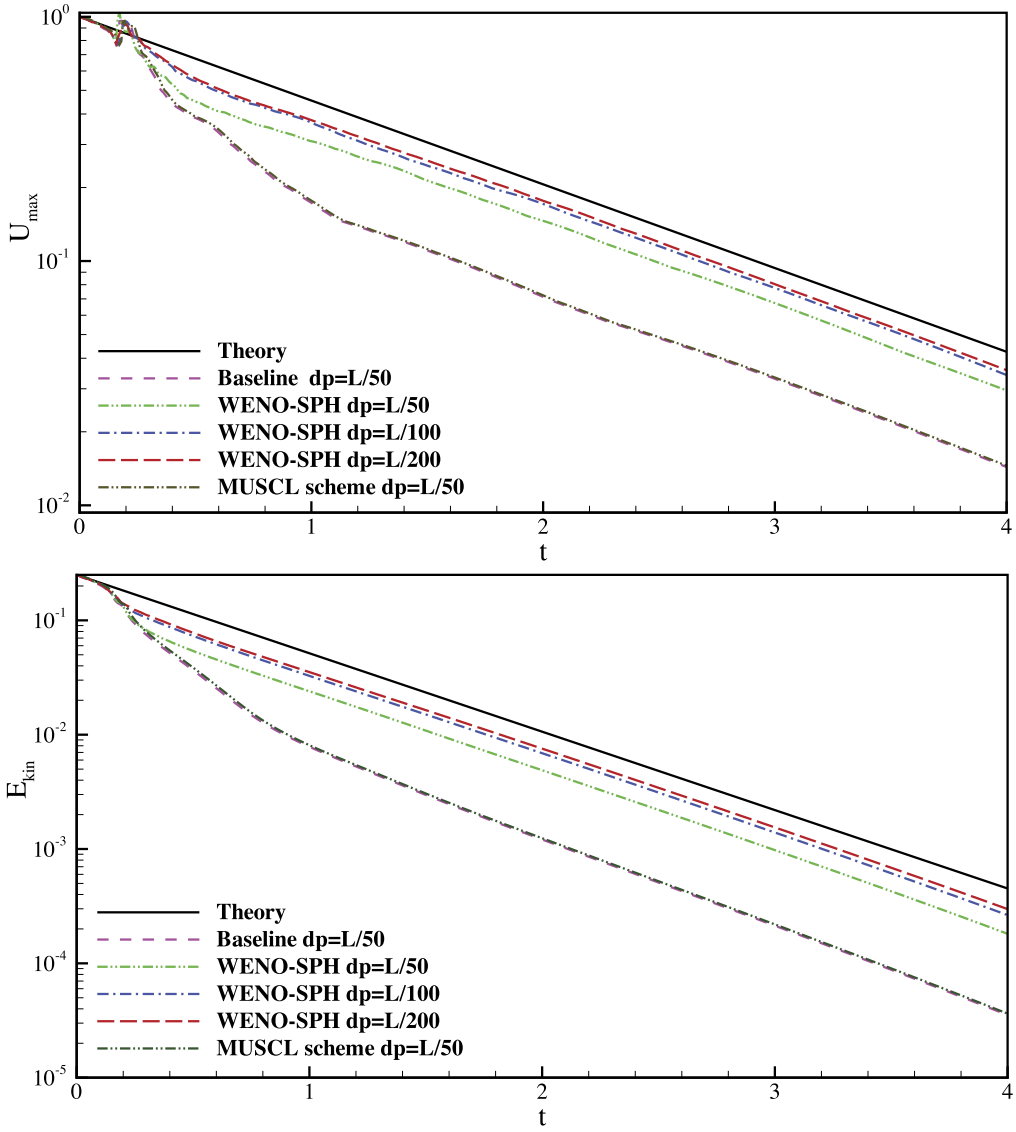

Fig. 17. Numerical results of the Taylor-Green vortex flow at $R_e = 100$ with a lattice initial particle distribution. Decay of the maximum velocity and the kinetic energy.

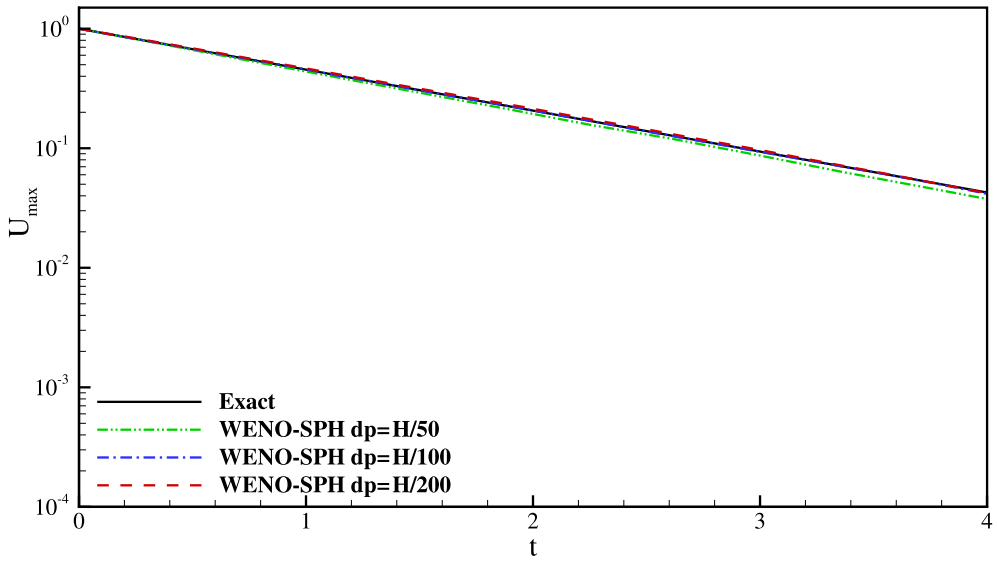

Fig. 18. Numerical results of the Taylor-Green vortex flow at $R_e = 100$ with a relaxed initial particle distribution. Decay of the maximum kinetic energy.

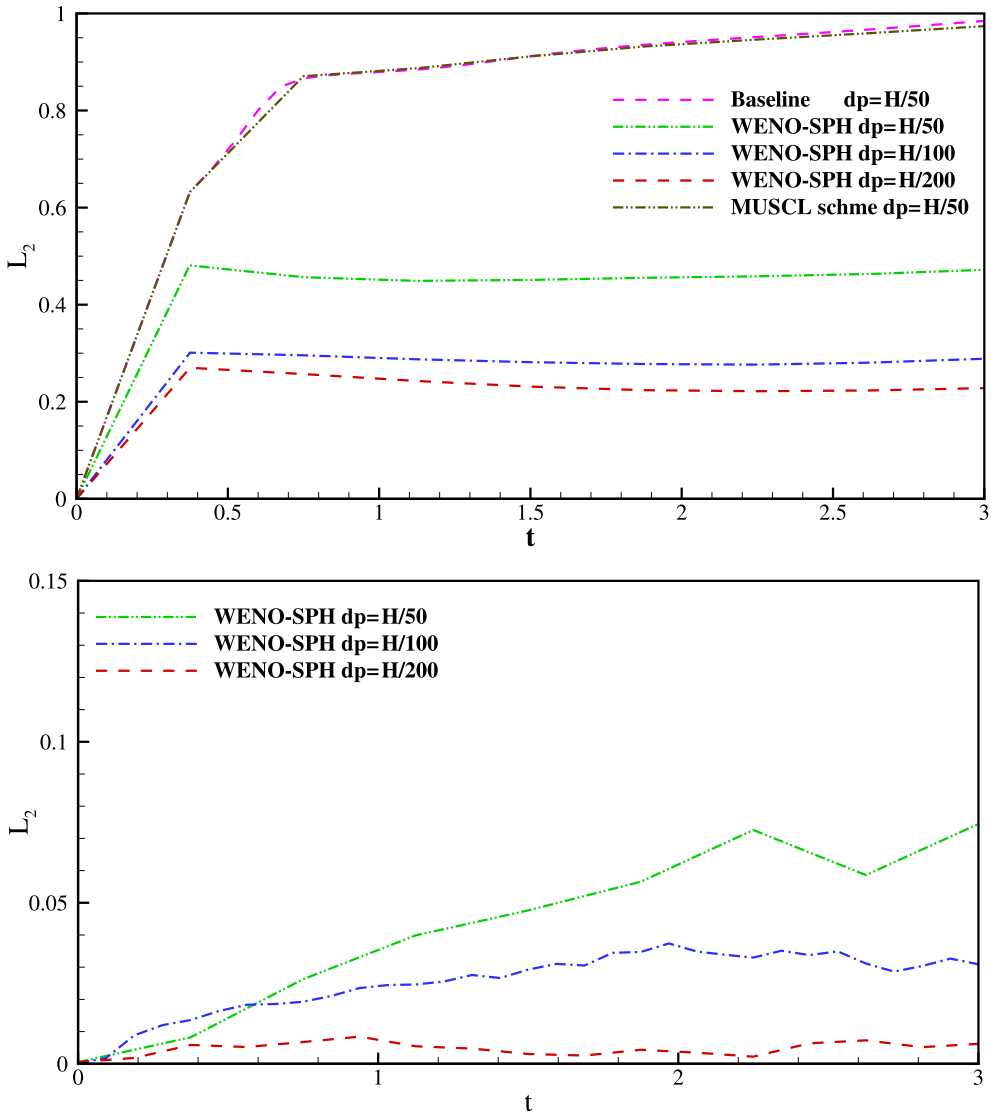

Fig. 19. The time history of L_2 errors of Taylor-Green vortex flow at $R_e = 100$. Particles initially on a Cartesian lattice (top panel) and relaxed distribution (bottom panel).

high Reynolds number, which leads to noisy pressure signal due to the very complex free-surface splashing and impact. Fig. 15 gives the evolution of relative total mechanical energy defined as $\Delta E = (E_{kin} + E_{pot} - E^0)/E^0$, where E^0 is the initial mechanical energy. WENO-SPH predicts considerably mechanical energy than Baseline and MUSCL due to less numerical damping.

3.5. Taylor-Green vortex flow

In the previous sections, we have shown that WENO-SPH improves the Baseline reconstruction on simulating violent free surface flows. Here, we show that it also improves the Baseline reconstruction on computing hydrodynamic problems without involving free surface. We consider a viscous two-dimensional Taylor-Green vortex flow, which is a periodic array of vortices with the velocity field given by

$$u(x, y, t) = -Ue^{bt}\cos(2\pi x)\sin(2\pi y),$$
$$v(x, y, t) = Ue^{bt}\sin(2\pi x)\cos(2\pi y), \tag{26}$$

where $b = -8\pi^2/R_e$, U is the maximum fluid velocity, R_e is the Reynolds number. The computation is performed on a square domain with unit length $L = 1$, and a periodic boundary condition is applied in both coordinate directions. The initial velocity distribution is obtained by setting $t = 0$ and $U = 1$ in Eq. (26), and the corresponding decay rate of the total kinetic energy is $-16\pi^2/R_e$.

We consider first the case with $R_e = 100$, and the simulation starts from a regular lattice particle distribution with a spatial resolution of $L/dp = 50$. The particle distributions at several time instants are shown in Fig. 16. At $t = 0.2$ s

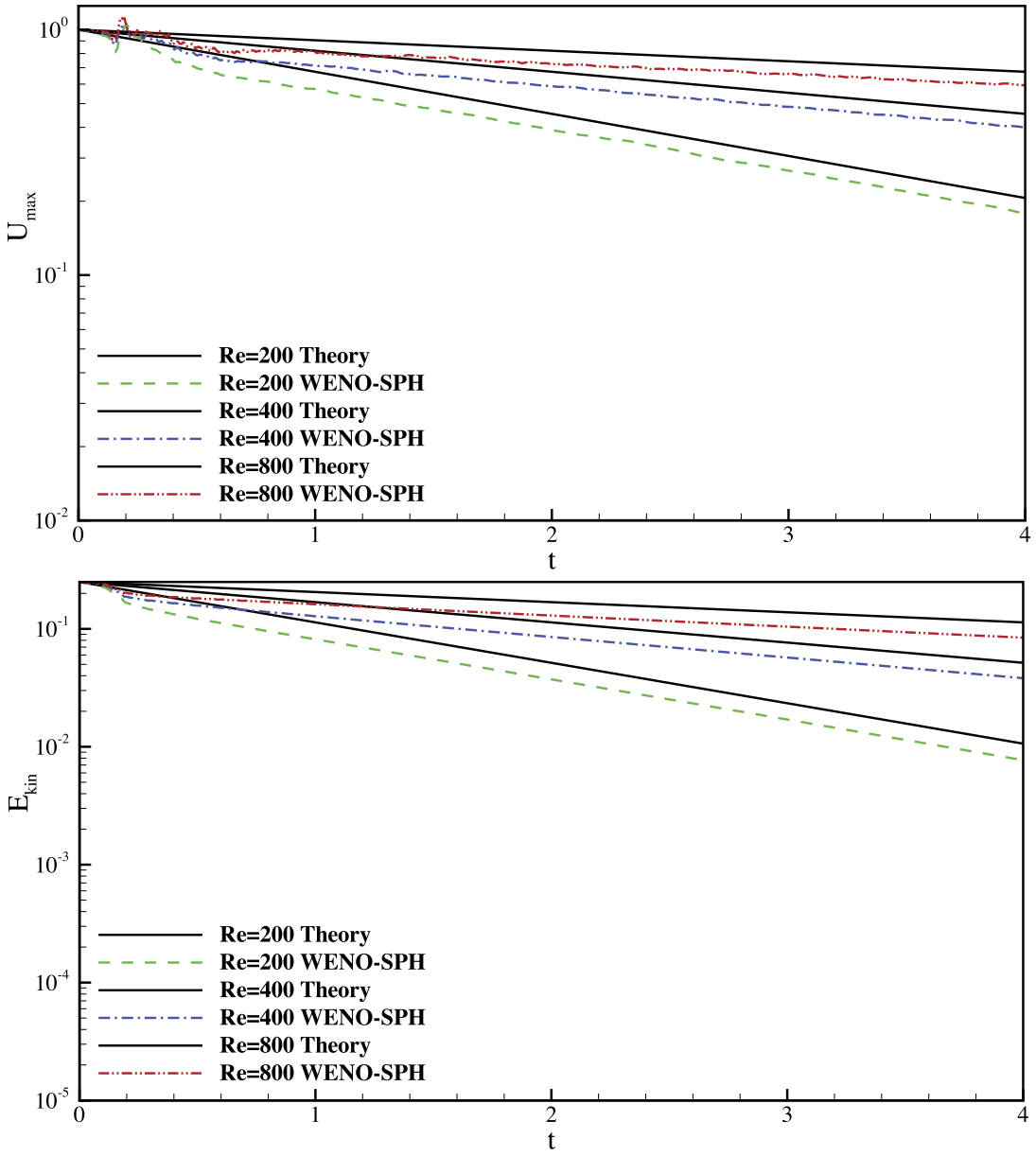

Fig. 20. Numerical results of the Taylor-Green vortex flow at different Reynolds number with a spatial resolution of $dp = L/100$: Decay of the maximum velocity and the kinetic energy.

both Baseline and WENO-SPH produce a particle distribution aligned with the stagnation lines of the flow as observed in the work of Adami et al. [47] where a transport-velocity formulation is proposed. At the later times, the ordered particle distribution is broken and WENO-SPH produces more uniform particle distribution than the Baseline (see the panels for $t = 0.6$ and 0.8 s in Fig. 16), similar to that obtained in the work of Refs. [47,63]. Fig. 17 gives the decay of maximum velocity and total kinetic energy over time. Similarly to Ref. [47], the decay rate is predicted correctly but with a shift. This shift is due to the rearrangement of the particle at early time, as shown in the panels for $t = 0.2$ s and 0.4 s in Fig. 16. Fig. 19 (top panel) gives the L_2 error defined as $L_2 = \sqrt{\sum_{i=1}^{N} \|u_i^{ext} - u_i\|^2} / \sqrt{\sum_{i=1}^{N} \|u_i^{ext}\|^2}$ where u_i^{ext} is the analytical fluid velocity at sampled at particle i. Compared with the Baseline and MUSCL, WENO-SPH generates relatively small errors of velocity at the same resolution. To avoid initial particle rearrangement, similarly to Ref. [47], we also simulate this test case by using a relaxed particle distribution generated by the final particle distribution from previous computation. As shown in Fig. 18, the initial overshoot in maximum velocity is eliminated and the results for three resolutions agree well with the analytical solution. From the error plot presented in Fig. 19 (bottom panel), it is observed that numerical results converge to the analytical solution.

To demonstrate the advantage of WENO-SPH, three more test cases at higher Reynolds numbers, i.e. $R_e = 200$, $R_e = 400$ and $R_e = 800$, are computed with a spatial resolution of $L/dp = 100$. Fig. 20 gives the time evolution of maximum velocity and total kinetic energy. Again, good agreements with analytical solutions is observed.

4. Conclusions

In this paper we have developed a WENO reconstruction scheme to improve a low-dissipation Riemann-solver based SPH method. We proposed a procedure utilizing the gradient of primitive variables to construct a 4-point stencil. This procedure is simple and easy to implement into existing SPH code for two and three-dimensions. Using the proposed WENO reconstruction, physical variables are reconstructed for the inter-particle Riemann problem which is used to determine the inter-particle interaction. A number of test cases have been computed with comparisons to previous numerical and experimental results. The proposed method exhibits considerably less numerical dissipation of mechanical energy while maintains robustness and efficiency. The present WENO reconstruction for the weakly-compressible simulation of free-surface flows can be extended for modeling fully compressible flows which is a subject of future work. Also other high resolution approximations, such as RKPM [38], can be incorporated into the WENO reconstruction by a MOOD-type approach [37] to increase the overall numerical accuracy.

Acknowledgements

CZ is partially supported by the China Scholarship Council (No. 2011623002), XYH is partially supported by Deutsche Forschungsgemeinschaft (HU 1527/6-1, HU 1527/10-1). We acknowledge the work of Sbalzarini et al. [64] who provides the Parallel Particle Mesh (PPM) Library that we use to implement our model and enables to perform large-scale simulations on parallel computer architectures.

References

[1] L.B. Lucy, A numerical approach to the testing of the fission hypothesis, Astron. J. 82 (1977) 1013–1024.
[2] R.A. Gingold, J.J. Monaghan, Smoothed particle hydrodynamics: theory and application to non-spherical stars, Mon. Not. R. Astron. Soc. 181 (3) (1977) 375–389.
[3] J.J. Monaghan, SPH without a tensile instability, J. Comput. Phys. 159 (2) (2000) 290–311.
[4] J.P. Gray, J.J. Monaghan, R.P. Swift, SPH elastic dynamics, Comput. Methods Appl. Mech. Eng. 190 (49) (2001) 6641–6662.
[5] P.W. Randles, L.D. Libersky, Smoothed particle hydrodynamics: some recent improvements and applications, Comput. Methods Appl. Mech. Eng. 139 (1) (1996) 375–408.
[6] J.J. Monaghan, Simulating free surface flows with SPH, J. Comput. Phys. 110 (2) (1994) 399–406.
[7] J.P. Morris, P.J. Fox, Y. Zhu, Modeling low Reynolds number incompressible flows using SPH, J. Comput. Phys. 136 (1) (1997) 214–226.
[8] X.Y. Hu, N.A. Adams, A multi-phase SPH method for macroscopic and mesoscopic flows, J. Comput. Phys. 213 (2) (2006) 844–861.
[9] X.Y. Hu, N.A. Adams, An incompressible multi-phase SPH method, J. Comput. Phys. 227 (1) (2007) 264–278.
[10] S. Adami, X.Y. Hu, N.A. Adams, A generalized wall boundary condition for smoothed particle hydrodynamics, J. Comput. Phys. 231 (21) (2012) 7057–7075.
[11] C. Antoci, M. Gallati, S. Sibilla, Numerical simulation of fluid–structure interaction by SPH, Comput. Struct. 85 (11) (2007) 879–890.
[12] M.B. Liu, G.R. Liu, Smoothed particle hydrodynamics (SPH): an overview and recent developments, Arch. Comput. Methods Eng. 17 (1) (2010) 25–76.
[13] J.J. Monaghan, Smoothed particle hydrodynamics and its diverse applications, Annu. Rev. Fluid Mech. 44 (2012) 323–346.
[14] T. Ye, D. Pan, C. Huang, M. Liu, Smoothed particle hydrodynamics (SPH) for complex fluid flows: recent developments in methodology and applications, Phys. Fluids 31 (1) (2019) 011301.
[15] J.J. Monaghan, R.A. Gingold, Shock simulation by the particle method SPH, J. Comput. Phys. 52 (2) (1983) 374–389.
[16] J.J. Monaghan, SPH and Riemann solvers, J. Comput. Phys. 136 (2) (1997) 298–307.
[17] E.F. Toro, Riemann Solvers and Numerical Methods for Fluid Dynamics: a Practical Introduction, Springer Science & Business Media, 2013.
[18] J.P. Vila, On particle weighted methods and smooth particle hydrodynamics, Math. Models Methods Appl. Sci. 9 (02) (1999) 161–209.
[19] S.I. Inutsuka, Reformulation of smoothed particle hydrodynamics with Riemann solver, J. Comput. Phys. 179 (1) (2002) 238–267.
[20] A.N. Parshikov, S.A. Medin, Smoothed particle hydrodynamics using interparticle contact algorithms, J. Comput. Phys. 180 (1) (2002) 358–382.
[21] N. Lanson, J.-P. Vila, Renormalized meshfree schemes I: consistency, stability, and hybrid methods for conservation laws, SIAM J. Numer. Anal. 46 (4) (2008) 1912–1934.
[22] N. Lanson, J.-P. Vila, Renormalized meshfree schemes II: convergence for scalar conservation laws, SIAM J. Numer. Anal. 46 (4) (2008) 1935–1964.
[23] S.-H. Cha, S.-i. Inutsuka, S. Nayakshin, Kelvin–Helmholtz instabilities with Godunov smoothed particle hydrodynamics, Mon. Not. R. Astron. Soc. 403 (3) (2010) 1165–1174.
[24] C. Zoppou, S. Roberts, Explicit schemes for dam-break simulations, J. Hydraul. Eng. 129 (1) (2003) 11–34.
[25] J.P. Vila, SPH renormalized hybrid methods for conservation laws: applications to free surface flows, in: Meshfree Methods for Partial Differential Equations II, Springer, 2005, pp. 207–229.
[26] V. Roubtsova, R. Kahawita, The SPH technique applied to free surface flows, Comput. Fluids 35 (10) (2006) 1359–1371.
[27] A. Ferrari, M. Dumbser, E.F. Toro, A. Armanini, A new 3D parallel SPH scheme for free surface flows, Comput. Fluids 38 (6) (2009) 1203–1217.
[28] A. Rafiee, S. Cummins, M. Rudman, K. Thiagarajan, Comparative study on the accuracy and stability of SPH schemes in simulating energetic free-surface flows, Eur. J. Mech. B, Fluids 36 (2012) 1–16.
[29] D. Molteni, A. Colagrossi, A simple procedure to improve the pressure evaluation in hydrodynamic context using the SPH, Comput. Phys. Commun. 180 (6) (2009) 861–872.
[30] C. Zhang, X. Hu, N. Adams, A weakly compressible SPH method based on a low-dissipation Riemann solver, J. Comput. Phys. 335 (2017) 605–620.
[31] M. Antuono, A. Colagrossi, S. Marrone, D. Molteni, Free-surface flows solved by means of SPH schemes with numerical diffusive terms, Comput. Phys. Commun. 181 (3) (2010) 532–549.
[32] S. Pirozzoli, Numerical methods for high-speed flows, Annu. Rev. Fluid Mech. 43 (2011) 163–194.
[33] K. Iwasaki, S.-i. Inutsuka, Smoothed particle magnetohydrodynamics with a Riemann solver and the method of characteristics, Mon. Not. R. Astron. Soc. 418 (3) (2011) 1668–1688.
[34] G. Murante, S. Borgani, R. Brunino, S.-H. Cha, Hydrodynamic simulations with the Godunov smoothed particle hydrodynamics, Mon. Not. R. Astron. Soc. 417 (1) (2011) 136–153.
[35] X. Zhang, H. Tian, L. Kuo, W. Chen, A contact SPH method with high-order limiters for simulation of inviscid compressible flows, Commun. Comput. Phys. 14 (02) (2013) 425–442.

[36] D. Avesani, M. Dumbser, A. Bellin, A new class of moving-least-squares WENO–SPH schemes, J. Comput. Phys. 270 (2014) 278–299.
[37] X. Nogueira, L. Ramírez, S. Clain, R. Loubère, L. Cueto-Felgueroso, I. Colominas, High-accurate SPH method with multidimensional optimal order detection limiting, Comput. Methods Appl. Mech. Eng. 310 (2016) 134–155.
[38] W.K. Liu, Y. Chen, S. Jun, J. Chen, T. Belytschko, C. Pan, R. Uras, C. Chang, Overview and applications of the reproducing kernel particle methods, Arch. Comput. Methods Eng. 3 (1) (1996) 3–80.
[39] J. Chen, J. Beraun, T. Carney, A corrective smoothed particle method for boundary value problems in heat conduction, Int. J. Numer. Methods Eng. 46 (2) (1999) 231–252.
[40] Z. Zhang, M. Liu, A decoupled finite particle method for modeling incompressible flows with free surfaces, Appl. Math. Model. 60 (2018) 606–633.
[41] J.J. Monaghan, Smoothed particle hydrodynamics, Annu. Rev. Astron. Astrophys. 30 (1) (1992) 543–574.
[42] S. Litvinov, X. Hu, N. Adams, Towards consistence and convergence of conservative SPH approximations, J. Comput. Phys. 301 (2015) 394–401.
[43] L. Fu, X.Y. Hu, N.A. Adams, A family of high-order targeted ENO schemes for compressible-fluid simulations, J. Comput. Phys. 305 (2016) 333–359.
[44] B. Wang, G. Xiang, X. Hu, An incremental-stencil WENO reconstruction for simulation of compressible two-phase flows, Int. J. Multiph. Flow 104 (2018) 20–31.
[45] G.-S. Jiang, C.-W. Shu, Efficient implementation of weighted ENO schemes, J. Comput. Phys. 126 (1) (1996) 202–228.
[46] J.J. Monaghan, Smoothed particle hydrodynamics, Rep. Prog. Phys. 68 (8) (2005) 1703.
[47] S. Adami, X.Y. Hu, N.A. Adams, A transport-velocity formulation for smoothed particle hydrodynamics, J. Comput. Phys. 241 (2013) 292–307.
[48] H. Wendland, Piecewise polynomial, positive definite and compactly supported radial functions of minimal degree, Adv. Comput. Math. 4 (1) (1995) 389–396.
[49] A. Ritter, Die fortpflanzung de wasserwellen, Z. Ver. Dtsch. Ing. 36 (33) (1892) 947–954.
[50] B.D. Roges, R. Dalrymple, P.K. Stansby, User guide for the SPHysics code v2.0, http://wiki.manchester.ac.uk/sphysics.
[51] J.M. Stone, T.A. Gardiner, P. Teuben, J.F. Hawley, J.B. Simon, Athena: a new code for astrophysical MHD, Astrophys. J. Suppl. Ser. 178 (1) (2008) 137.
[52] V. Springel, E pur si muove: Galilean-invariant cosmological hydrodynamical simulations on a moving mesh, Mon. Not. R. Astron. Soc. 401 (2) (2010) 791–851.
[53] W. Benz, Smooth particle hydrodynamics: a review, in: The Numerical Modelling of Nonlinear Stellar Pulsations, Springer, 1990, pp. 269–288.
[54] S. Litvinov, X. Hu, N. Adams, Towards consistence and convergence for conservative SPH approximations 301 (2015) 394–401.
[55] A. Colagrossi, M. Landrini, Numerical simulation of interfacial flows by smoothed particle hydrodynamics, J. Comput. Phys. 191 (2) (2003) 448–475.
[56] S. Marrone, M. Antuono, A. Colagrossi, G. Colicchio, D. Le Touzé, G. Graziani, δ-SPH model for simulating violent impact flows, Comput. Methods Appl. Mech. Eng. 200 (13) (2011) 1526–1542.
[57] L. Lobovskỳ, E. Botia Vera, F. Castellana, J. Mas-Soler, A. Souto Iglesias, Experimental investigation of dynamic pressure loads during dam break, J. Fluids Struct. 48 (2014) 407–434.
[58] P. Stansby, A. Chegini, T. Barnes, The initial stages of dam-break flow, J. Fluid Mech. 374 (1998) 407–424.
[59] X. Xu, An improved SPH approach for simulating 3D dam-break flows with breaking waves, Comput. Methods Appl. Mech. Eng. 311 (2016) 723–742.
[60] G. Colicchio, Violent Disturbance and Fragmentation of Free Surfaces, Ph.D. thesis, University of Southampton, 2004.
[61] A. Rafiee, F. Pistani, K. Thiagarajan, Study of liquid sloshing: numerical and experimental approach, Comput. Mech. 47 (1) (2011) 65–75.
[62] H. Akyildiz, E. Ünal, Experimental investigation of pressure distribution on a rectangular tank due to the liquid sloshing, Ocean Eng. 32 (11) (2005) 1503–1516.
[63] R. Xu, P. Stansby, D. Laurence, Accuracy and stability in incompressible SPH (ISPH) based on the projection method and a new approach, J. Comput. Phys. 228 (18) (2009) 6703–6725.
[64] I.F. Sbalzarini, J.H. Walther, M. Bergdorf, S.E. Hieber, E.M. Kotsalis, P. Koumoutsakos, PPM–a highly efficient parallel particle–mesh library for the simulation of continuum systems, J. Comput. Phys. 215 (2) (2006) 566–588.

A.3 Paper III

Chi Zhang, Xiangyu Y. Hu, Nikolaus A. Adams

A generalized transport-velocity formulation for smoothed particle hydrodynamics

In *Journal of Computational Physics*, Volume 337, 2017, pp. 216-232, DOI: `https://doi.org/10.1016/j.jcp.2017.02.016`.

Contribution: My contribution to this work was the development of the method and the corresponding computer code for its implementation. I performed simulations and analyzed the results, and wrote the manuscript for the publication.

Journal of Computational Physics 337 (2017) 216–232

Contents lists available at ScienceDirect

Journal of Computational Physics

www.elsevier.com/locate/jcp

A generalized transport-velocity formulation for smoothed particle hydrodynamics

Chi Zhang, Xiangyu Y. Hu *, Nikolaus A. Adams

Lehrstuhl für Aerodynamik und Strömungsmechanik, Technische Universität München, 85748 Garching, Germany

ARTICLE INFO

Article history:
Received 19 May 2015
Received in revised form 21 November 2016
Accepted 6 February 2017
Available online 21 February 2017

Keywords:
Weakly-compressible SPH
Transport-velocity formulation
Tensile instability

ABSTRACT

The standard smoothed particle hydrodynamics (SPH) method suffers from tensile instability. In fluid-dynamics simulations this instability leads to particle clumping and void regions when negative pressure occurs. In solid-dynamics simulations, it results in unphysical structure fragmentation. In this work the transport-velocity formulation of Adami et al. (2013) [14] is generalized for providing a solution of this long-standing problem. Other than imposing a global background pressure, a variable background pressure is used to modify the particle transport velocity and eliminate the tensile instability completely. Furthermore, such a modification is localized by defining a shortened smoothing length. The generalized formulation is suitable for fluid and solid materials with and without free surfaces. The results of extensive numerical tests on both fluid and solid dynamics problems indicate that the new method provides a unified approach for multi-physics SPH simulations.

1. Introduction

As a fully Lagrangian, mesh-less method, smoothed particle hydrodynamics (SPH) was proposed by Lucy [1], Gingold and Monaghan [2] independently. SPH was originally developed for simulating astrophysical problems and has been applied successfully to a wide range of solid and fluid dynamic problems. For the simulation of solid dynamics SPH offers significant advantages in terms of handling large deformations in a purely Lagrangian frame. SPH uses a kernel function to approximate field quantities at arbitrarily distributed Lagrangian discretization elements (particles) in the form of particle interactions. For example, the particles repel or attract each other under the action of compression or tension, respectively. Subjected to tension, the mutual attraction of particles may result in a so-called tensile instability which can lead to unphysical fractures [3]. For the simulation of fluid dynamics tensile instability occurs when the static pressure becomes negative and results in particle clumping or void regions.

Several attempts have been carried out to address this problem since its first observation. Schussler and Schmitt [4] proposed a new kernel function which can produce a repulsive force when negative pressure occurs. However, this function does not satisfy the requirement of continuous first-order derivatives. Jonson and Beissel [5] used a modified non-zero quadratic kernel function to reduce this instability. The problem of this kernel is that it does not have a continuous second-order derivative. Randles and Libersky [6] used a conservative smoothing approach to add stabilizing dissipation for removing the tensile instability. Mandell et al. [7] commented that this approach is good in some cases but only qualitatively correct in other cases. Dilts [8] proposed a moving-least-square particle hydrodynamics (MLSPH) method which

* Corresponding author.
E-mail address: xiangyu.hu@tum.de (X.Y. Hu).

http://dx.doi.org/10.1016/j.jcp.2017.02.016
0021-9991/

replaces the SPH approximation with moving-least-square formulation to reduce tensile instability. While MLSPH is not locally conservative, it increases substantially computational cost compared with standard SPH. Dyka et al. [9] developed a stress-point algorithm which uses stress points located in the mid-way between particles to calculate the stress and maps it to SPH particles. Randles and Libersky [10] showed that this algorithm is stable but complex and computationally inefficient. Since SPH is a particle-based numerical method, a straightforward concept is to eliminate tensile instability by mimicking atomic forces rather than changing the kernel function [11]. Monaghan [12] and Gray et al. [11] developed an artificial stress algorithm to prevent particle clumping and successfully simulated the cases of an oscillating plate and colliding rubber rings. However, as pointed out by Lobovsky and Kren [13], this algorithm fails when the material has comparably high Poisson ratio.

Adami et al. [14] proposed a transport-velocity formulation to address particle clumping and void-region problems in weakly-compressible SPH simulation of flow at high Reynolds number. With the original transport-velocity formulation [14], the momentum equation is reformulated by moving particles with a transport velocity [15,16]. Using a globally constant background pressure for regulation, the transport velocity leads to favorable particle distribution and reduces numerical error [17]. A problem of the original transport-velocity formulation is that there is no straightforward applicability to problems with free fluid or solid material surfaces. This is due to the fact that a constant correcting background pressure may introduce a large artificial velocity at such boundaries. We emphasis that the idea of moving particles with a transport velocity which may differ from the momentum velocity was first proposed with the XSPH scheme to prevent penetration in impact problems [18]. Hu and Adams [15] utilized the transport velocity obtained from an intermediate projection step to impose fluid incompressibility. Xu et al. [19] developed a shifting approach in the incompressible SPH method for homogenized particle distribution. Lind et al. [20] extended this approach to simulate free surface flow with a surface-identification algorithm. Very recently, Vacondio et al. [21] modified this approach for a variable-resolution SPH method. Monaghan [22] developed an SPH turbulence model in which the used smoothed transport velocity can be related to the Lagrangian averaged Navier Stokes equations (LANS) [23]. However, none of these approaches was used to address the tensile-instability issue in SPH simulation of solid dynamics to the best knowledge of the authors.

In this paper, we extend the original transport-velocity formulation to solve the tensile instability problem of SPH for solid and fluid dynamic problems. Instead of a globally constant background pressure the present method uses a variable background pressure for the transport velocity correction. According to this modification the correction is proportional to the local pressure and can be implemented to problems with free fluid or solid material surfaces. Additionally, due to a shortened smoothing length, the background pressure correction is localized by involving only nearest-neighbor particles. The numerical results show that the present method eliminates the tensile instability completely in simulations of both solid and fluid dynamics. The remainder of this paper is arranged as follows: in the Section 2 and 3, the details of the method are described. A wide range of classical problems is tested in Section 4 and brief concluding remarks are given in Section 5.

2. Governing equations

The governing equations for continuum mechanics in a Lagrangian reference frame include the equations for conservation for mass and momentum. The mass-conservation equation is

$$\frac{d\rho}{dt} = -\rho \nabla \cdot \mathbf{v} \tag{1}$$

and the momentum-conservation equation is

$$\frac{d\mathbf{v}}{dt} = \frac{1}{\rho}\nabla \cdot \boldsymbol{\sigma} + \mathbf{g} \tag{2}$$

Here, ρ is density, $\mathbf{v}$ is velocity, t is time, $\mathbf{g}$ is the body force, $\boldsymbol{\sigma}$ is the stress tensor and

$$\frac{d(\bullet)}{dt} = \frac{\partial(\bullet)}{\partial t} + \mathbf{v} \cdot \nabla(\bullet) \tag{3}$$

refers to the material derivative. Note that Eqs. (1) and (2) allow a common description of both fluid and solid dynamics.

For elastic solid materials, the stress tensor $\boldsymbol{\sigma}$ can be decomposed into isotropic and deviatoric parts

$$\boldsymbol{\sigma} = -p\mathbf{I} + \boldsymbol{\sigma}', \tag{4}$$

where p is the hydrostatic pressure, $\mathbf{I}$ is identity matrix and $\boldsymbol{\sigma}'$ is the deviatoric stress. Using Jaumann's formulation of the Hooke's law, the rate of change of the deviatoric stress can be described as

$$\frac{d\boldsymbol{\sigma}'}{dt} = 2G(\boldsymbol{\epsilon} - \frac{1}{3}Tr(\boldsymbol{\epsilon})\mathbf{I}) + \boldsymbol{\sigma}' \cdot \boldsymbol{\Omega}^T + \boldsymbol{\Omega} \cdot \boldsymbol{\sigma}', \tag{5}$$

where G is the shear modulus, $\boldsymbol{\epsilon}$ is the strain tensor

$$\boldsymbol{\epsilon} = \frac{1}{2}\left(\nabla \otimes \mathbf{v} + (\nabla \otimes \mathbf{v})^T\right), \tag{6}$$

and $\boldsymbol{\Omega}$ is the rotation tensor

$$\boldsymbol{\Omega} = \frac{1}{2}\left(\nabla \otimes \mathbf{v} - (\nabla \otimes \mathbf{v})^T\right). \tag{7}$$

For a weakly-compressible or incompressible fluid, the deviatoric stress vanishes and a viscous force is added to the stress tensor:

$$\boldsymbol{\sigma} = -p\mathbf{I} + 2\eta\boldsymbol{\epsilon}, \tag{8}$$

where η is the dynamic viscosity.

3. Numerical method

With the transport-velocity formulation [14] the momentum velocity for particle transport is modified, and we can redefine the material derivative of a particle moving with the transport velocity $\widetilde{\mathbf{v}}$ as

$$\frac{\widetilde{d}(\bullet)}{dt} = \frac{\partial(\bullet)}{\partial t} + \widetilde{\mathbf{v}} \cdot \nabla(\bullet). \tag{9}$$

The mass-conservation equation for a Lagrangian particle is modified accordingly to

$$\frac{\widetilde{d}\rho}{dt} = -\rho\nabla \cdot \widetilde{\mathbf{v}} \tag{10}$$

and the momentum equation to

$$\frac{\widetilde{d}\mathbf{v}}{dt} = \frac{1}{\rho}\nabla \cdot \boldsymbol{\sigma} + \frac{1}{\rho}\nabla \cdot \mathbf{A} + \mathbf{g}, \tag{11}$$

where the extra stress tensor $\mathbf{A} = \rho\mathbf{v} \otimes (\widetilde{\mathbf{v}} - \mathbf{v})$ is a consequence of the modified transport velocity.

3.1. Evolution of density

Following the standard SPH method, the density evolution equation is discretized as

$$\frac{\widetilde{d}\rho_a}{dt} = \rho_a \sum_b \frac{m_b}{\rho_b}\frac{\partial W_{ab}}{\partial r_{ab}}\mathbf{e}_{ab} \cdot \widetilde{\mathbf{v}}_{ab}, \tag{12}$$

where m is the particle mass, $\widetilde{\mathbf{v}}_{ab} = \widetilde{\mathbf{v}}_a - \widetilde{\mathbf{v}}_b$ is the relative transport velocity between particles a and b, $\frac{\partial W_{ab}}{\partial r_{ab}}\mathbf{e}_{ab}$ is gradient of the kernel function $W(\mathbf{r}_{ab}, h)$. Here, h is the smoothing length, $\mathbf{r}_{ab} = \mathbf{r}_a - \mathbf{r}_b = r_{ab}\mathbf{e}_{ab}$ and $\mathbf{e}_{ab}$ is a normalized vector pointing from particle b to particle a. Note that when density evolution equation is applied for the simulation of weakly-compressible or incompressible fluid dynamics, it may lead to large density errors when the Reynolds number of the flow is large [24]. Therefore, similarly to Colagrossi and Landrini [24], the density field in fluid-dynamics simulation is reinitialized at each time-step by

$$\rho_a = \frac{\sum_b m_b W_{ab}}{\min(1, \sum_b W_{ab}\frac{m_b}{\rho^*})}, \tag{13}$$

where ρ^* is the density before reinitialization. Note that, limiting of the denominator is due to the fact that $\sum_b W_{ab}\frac{m_b}{\rho^*} \approx \int W(\mathbf{r} - \mathbf{r}_a, h)d\mathbf{r} \leq 1$, e.g. when a free surface passes through the support of $W(\mathbf{r} - \mathbf{r}_a, h)$. To calculate the divergence of deviatoric stresses of elastic solid dynamics, the velocity gradient can be approximated as

$$\left(\nabla \otimes \widetilde{\mathbf{v}}\right)_a = \sum_b \frac{m_b}{\rho_b}\frac{\partial W_{ab}}{\partial r_{ab}}\widetilde{\mathbf{v}}_{ab} \otimes \mathbf{e}_{ab} \tag{14}$$

3.2. Momentum equation

The momentum-conservation equation for an elastic solid material can be written as [25,26]

$$\frac{\widetilde{d}\mathbf{v}_a}{dt} = -\sum_b m_b \frac{\partial W_{ab}}{\partial r_{ab}}\mathbf{e}_{ab}\cdot\left[\left(\frac{p_a}{\rho_a^2}+\frac{p_b}{\rho_b^2}\right)\mathbf{I}-\left(\frac{\boldsymbol{\sigma}'_a}{\rho_a^2}+\frac{\boldsymbol{\sigma}'_b}{\rho_b^2}\right)\right]+\mathbf{g}_a. \tag{15}$$

For fluid particles, the viscous force is obtained from the inter-particle-averaged shear viscosity in SPH form [27,15]

$$\eta_{ab} = \frac{2\eta_a\eta_b}{\eta_a+\eta_b}. \tag{16}$$

The discretized momentum-conservation equation for fluid particle is

$$\frac{\widetilde{d}\mathbf{v}_a}{dt} = -\sum_b m_b \frac{\partial W_{ab}}{\partial r_{ab}}\mathbf{e}_{ab}\cdot\left[\left(\frac{p_a}{\rho_a^2}+\frac{p_b}{\rho_b^2}\right)\mathbf{I}-\left(\frac{\mathbf{A}_a}{\rho_a^2}+\frac{\mathbf{A}_b}{\rho_b^2}\right)\right]+\sum_b m_b\frac{\eta_{ab}\mathbf{v}_{ab}}{\rho_a\rho_b r_{ab}}\frac{\partial W_{ab}}{\partial r_{ab}}+\mathbf{g}_a. \tag{17}$$

The extra-stress term $\mathbf{A}$ is not present in the momentum equation for solid dynamics as our numerical tests show that its influence is negligible due to the well resolved velocity field. This is consistent with the observation that, for flows up to moderate Reynolds numbers ($O(10^2)$), the influence of this term is negligible [16]. Actually, this correction term has notable influence only when the flow is at high Reynolds number [16] or is inviscid, see Sec. 4.7. Although the viscous term in Eq. (17) does not strictly conserve angular momentum, it is generally accurate even for rotational flow as shown in Refs. [27,15]. Similarly to the viscous force term the present form of the extra-stress term in Eq. (17) does not strictly conserve the angular momentum either. As will be shown in Sec. 4.5, the angular-momentum conservation errors generally are very small. Following the weakly-compressible SPH (WCSPH) approach [28,27], pressure is calculated from an artificial isothermal equation of state:

$$p = K\left(\frac{\rho}{\rho_0}-1\right), \tag{18}$$

where $K=\rho_0 c_0^2$ is the bulk modulus. Here, the constants c_0 and ρ_0 are the reference sound speed and density, respectively. Note that, since Eq. (18) gives zero pressure at reference density, negative pressure occurs when $\rho<\rho_0$.

3.3. Particle transport velocity

In Adami et al. [14], instead of the momentum velocity the transport velocity $\widetilde{\mathbf{v}}$ is used for particle transport

$$\frac{d\mathbf{r}_a}{dt} = \widetilde{\mathbf{v}}_a. \tag{19}$$

The transport velocity at every time step is obtained by modifying the momentum velocity, i.e.,

$$\widetilde{\mathbf{v}}_a(t+\delta t) = \mathbf{v}_a(t)+\delta t\left(\frac{\widetilde{d}\mathbf{v}_a}{dt}-\frac{1}{\rho_a}\nabla p^0\right), \tag{20}$$

where the term $\frac{1}{\rho_a}\nabla p^0$ is discretized as

$$\frac{1}{\rho_a}\nabla p^0 = p^0\sum_b m_b\left(\frac{1}{\rho_a^2}+\frac{1}{\rho_b^2}\right)\frac{\partial W_{ab}}{\partial r_{ab}}\mathbf{e}_{ab} = \left(\frac{d\mathbf{v}_a}{dt}\right)_c, \tag{21}$$

where p^0 in Adami et al. [14] is a globally constant background pressure whose exact gradient vanishes. In SPH, however, the conservative approximation of the gradient for constant background pressure results in a residual force due the lack of zero-order consistency. This residual force leads to a self-relaxation mechanism which regularizes the particle distribution such that it assumes approximately a configuration with low consistency error [17].

If we consider the right-hand-side of Eq. (21) as a general correction of the particle acceleration such that $\left(\frac{d\mathbf{v}_a}{dt}\right)_c$ is proportional to p^0, we are free to choose different p^0 for different particles, or a different influence radii of such a correction. In this paper, we propose to modify Eq. (21) as

$$\left(\frac{d\mathbf{v}_a}{dt}\right)_c = p_a^0\sum_b m_b\frac{1}{\rho_a^2}\frac{\partial\widetilde{W}_{ab}}{\partial r_{ab}}\mathbf{e}_{ab}, \tag{22}$$

where $\widetilde{W}_{ab} = W(\mathbf{r}_{ab}, \widetilde{h})$ and $\widetilde{h} = 0.5h$, which indicates that only the nearest-neighbor particles within the distance $2\widetilde{h}$ affect the correction. Here, p_a^0 is chosen as

$$p_a^0 = \min(10|p_a|, p_{ref}), \tag{23}$$

where p_{ref} is a reference pressure to avoid excessive time-step size limitation. For a weakly-compressible fluid or solid, a typical choice is $p_{ref} = K$. For compressible fluid or solid, $p_{ref} = \max(|p|_{\max}, K)$, where $|p|_{\max}$ is the maximum pressure magnitude in the entire domain. While Eq. (22) implies that the correction is proportional to the local particle pressure, it also implies that there is no, or only a very slight correction for a particle near a free fluid or solid material surface due to the surface boundary condition. Note that the factor of $|p_a|$ in Eq. (23) and the size of $\widetilde{h}$ in $\widetilde{W}_{ab}$ may affect the correction effectiveness. By preliminary numerical tests we found that the parameters of 10 and $0.5h$ are generally suitable. Therefore, we use the same values for all numerical tests of solid and fluid dynamics throughout this paper.

3.4. Time integration scheme

Similarly to Adami et al. [14], the kick-drift-kick scheme [29] is used for time integration. First the momentum velocity and transport velocity are calculated at the half time step,

$$\mathbf{v}_a^{n+\frac{1}{2}} = \mathbf{v}_a^n + \frac{\Delta t}{2}\left(\frac{\widetilde{d}\mathbf{v}_a}{dt}\right)^n, \tag{24}$$

$$\widetilde{\mathbf{v}}_a^{n+\frac{1}{2}} = \mathbf{v}_a^{n+\frac{1}{2}} + \frac{\Delta t}{2}\left(\frac{d\mathbf{v}_a}{dt}\right)_c^n. \tag{25}$$

Then the time derivatives of density and deviatoric stresses are calculated using the transport velocity by Eq. (12). The new time step density, deviatoric stresses and particle position are updated by

$$\rho_a^{n+1} = \rho_a^n + \Delta t\left(\frac{\widetilde{d}\rho_a}{dt}\right)^{n+\frac{1}{2}}, \tag{26}$$

$$\boldsymbol{\sigma}_a'^{n+1} = \boldsymbol{\sigma}_a'^{n} + \Delta t\left(\frac{\widetilde{d}\boldsymbol{\sigma}_a'}{dt}\right)^{n+\frac{1}{2}}, \tag{27}$$

$$\mathbf{r}_a^{n+1} = \mathbf{r}_a^n + \Delta t\widetilde{\mathbf{v}}_a^{n+\frac{1}{2}}. \tag{28}$$

Finally, at new time-step particle position, the momentum velocity is updated

$$\mathbf{v}_a^{n+1} = \mathbf{v}_a^{n+\frac{1}{2}} + \frac{\Delta t}{2}\left(\frac{\widetilde{d}\mathbf{v}_a}{dt}\right)^{n+1}. \tag{29}$$

For numerical stability several time step criteria should be satisfied, including the CFL condition

$$\Delta t \le 0.25\left(\frac{h}{c + |U|}\right), \tag{30}$$

where $|U|$ is the maximum velocity magnitude, the viscous condition

$$\Delta t \le 0.25\left(\frac{h^2}{\nu}\right), \tag{31}$$

and the body-force condition

$$\Delta t \le 0.25\sqrt{h/g}. \tag{32}$$

For solid dynamics, the elastic stress condition is

$$\Delta t \le 0.25\left(\frac{h}{\sqrt{\frac{E}{\rho_0}} + |U|}\right), \tag{33}$$

where E denotes the Young's modulus.

4. Numerical examples

A wide range of classical test problems, including free-surface flow, elastic–solid dynamics, high-velocity impact and Taylor–Green vortex flow, are studied. The Wendland C2 [30] kernel function and a constant smoothing length, $h = 1.3 \times \Delta x$, where Δx is the initial particle distance are used for all tests.

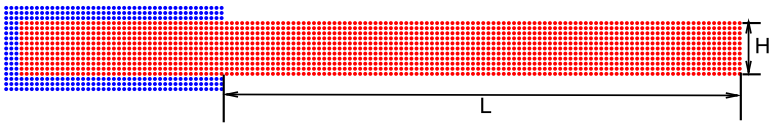

Fig. 1. Computational domain of the oscillating plate.

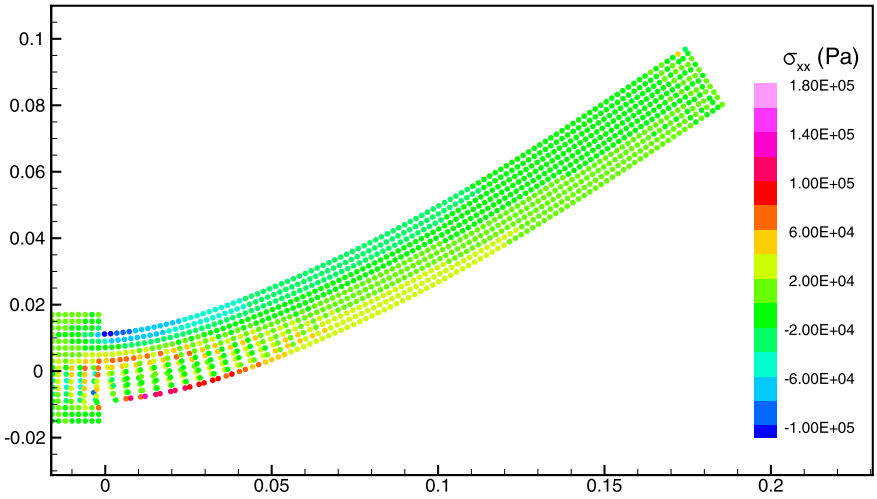

Fig. 2. Simulation of the oscillating plate using standard SPH method and particles are colored by σ_{xx} stress field ($L = 0.2$ m, $H = 0.02$ m and $V_f = 0.05$ m/s) at t = 0.03 s.

4.1. Oscillating plate

Landau and Lifshits [31] studied theoretically the oscillation of a thin plate with one edge fixed. Gray et al. [11] investigated the 2D model numerically using SPH method with artificial stresses for suppressing tensile instability. As shown in Fig. 1, the plate is clamped between layers of SPH particles which are not allowed to move and the motion of plate particles is initialized by a velocity profile, which is perpendicular to the plate and given by

$$v_y(x) = V_f c_0 \frac{F(x)}{F(L)}, \tag{34}$$

where, the constant of V_f varies for the different cases, L is the length of plate,

$$F(x) = (coskL + coshkL)(coshkx - coskx) + (sinkL - sinhkL)(sinhkx - sinkx), \tag{35}$$

where k is the wave number which can be derived from $kL = 1.875$. We set the plate properties as follows: Young's modulus $E = 2.0 \times 10^6$ Pa, density $\rho = 1000.0\ kg/m^3$ and Possion ratio $\nu = 0.3975$. In our simulation, the initial particle spacing is set as $\Delta x = 0.002$ m, and the reference sound speed $c_0 = \sqrt{\frac{E}{3(1-2\nu)\rho_0}}$. Because of the tensile instability of standard SPH unphysical fracture results, and the plate breaks where the maximum tensile stress appears, as shown in Fig. 2. With the present method the tensile instability is eliminated and the simulation is stable as shown in Fig. 3. A highly nonlinear case with large value of V_f is also simulated, as shown in Fig. 4. The results show that the simulation is stable even though the plate is strongly deformed. Note that these results are in good agreement with those obtained by the artificial stress algorithm in Gray et al. [11].

A convergence study and a comparison between numerical and analytical results are performed to demonstrate the accuracy of present method. For the convergence study, different resolutions are tested by varying initial particle spacing. The amplitude, as a function of time, of the mid-point in thickness direction at the end of plate is shown in Fig. 5. This study indicates that the period and amplitude of the oscillations converge rapidly with increasing resolution. The comparison of the first period of oscillations for a wide range of values of V_f obtained from numerical and analytical results is shown in the Table 1. The errors are around 13%, as the analytical results are based on a thin plate model, and in our simulation $H/L = 0.1$. Results of other cases at $H/L = 0.05$ are shown in the Table 2 and the errors decease to around 2.5% confirming previous numerical studies [11].

4.2. Colliding rubber rings

The collision of rubber rings was first investigated by Swegle et al. [3]. Our aim here is to show that, with the present method, the "numerical fracture" produced by the standard SPH the simulation does not occur. Monaghan [12] and Grey et al. [11] simulated this problem with artificial stresses to suppress tensile instability.

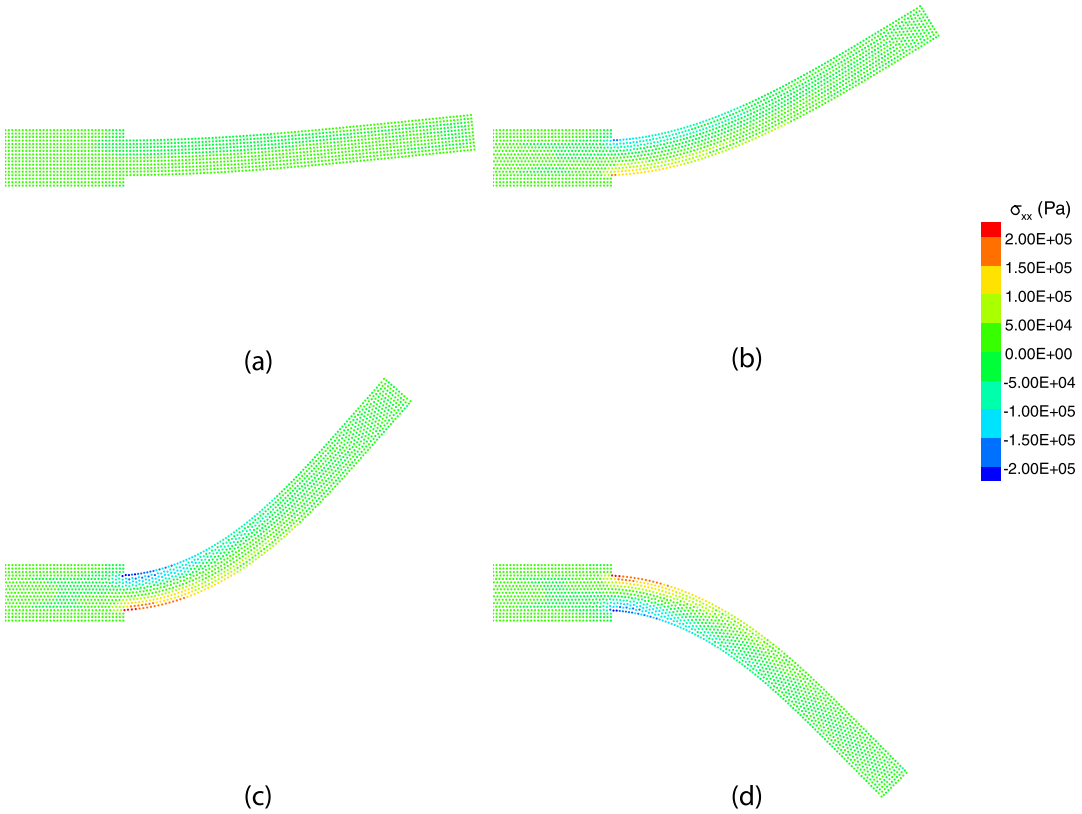

Fig. 3. Simulation of the oscillating plate using the present method and particles are colored by σ_{xx} stress field ($L = 0.2$ m, $H = 0.02$ m and $V_f = 0.05$ m/s): (a) $t = 0.01$ s, (b) $t = 0.05$ s, (c) $t = 0.07$ s, (d) $t = 0.22$ s.

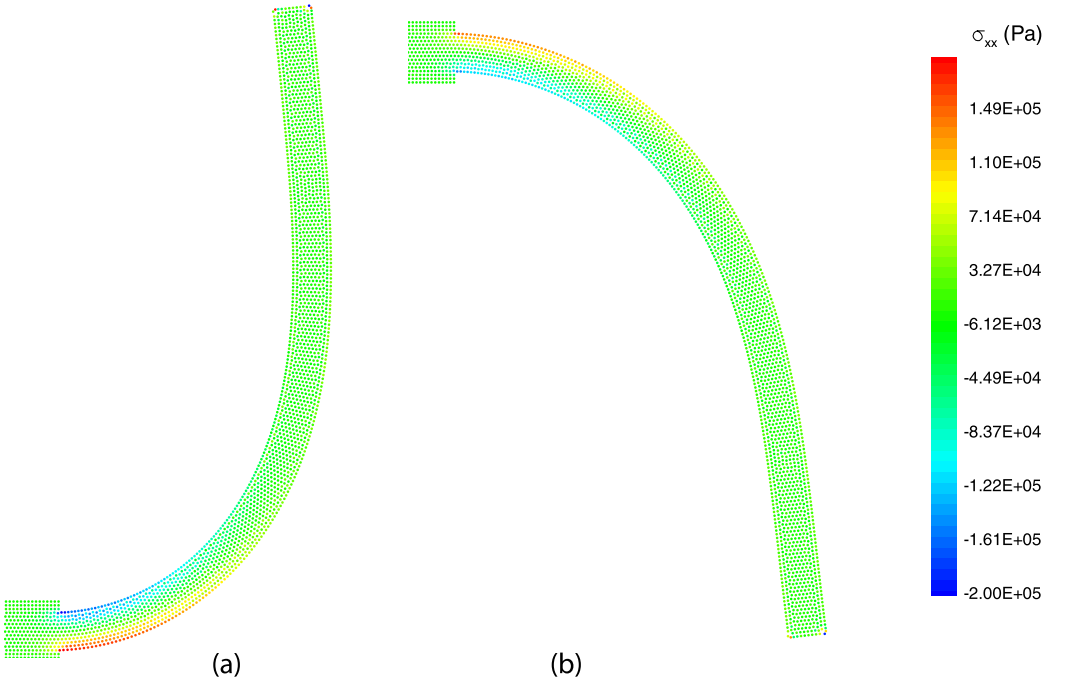

Fig. 4. Highly nonlinear case of an oscillating plate using the present method and particles are colored by σ_{xx} stress field ($L = 0.2$ m, $H = 0.01$ m and $V_f = 0.05$ m/s): (a) $t = 0.25$ s, (b) $t = 0.51$ s.

As shown in Fig. 6 (a) the inner ring radius is $r_{min} = 0.03$ m and the outer ring radius is $r_{max} = 0.04$ m. The rings have the same material properties: Young's modulus $E = 0.01$ GPa and density $\rho = 1.2 \times 10^3$ kg/m^3. We set the rubber ring relative velocity as $v_0 = 0.12c_0$ and the initial particle spacing as $\Delta x = 0.001$ m.

The first test is with a Poisson ratio $\nu = 0.3975$. The results are shown in Fig. 6, which are in agreement with those of Grey et al. [11]. To show the improvement due to the present method, a case with $\nu = 0.447$ is also simulated. The results,

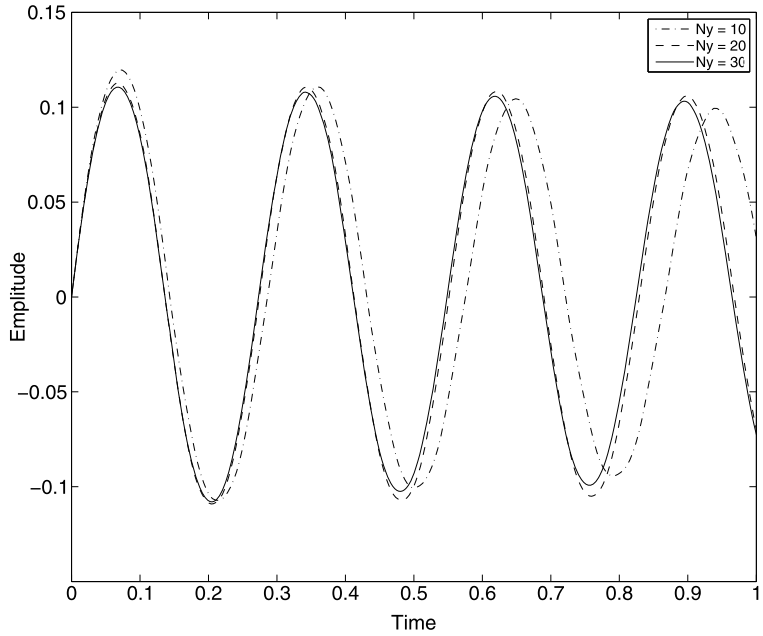

Fig. 5. Convergence study of the present method for the oscillating plate ($L = 0.2$ m, $H = 0.01$ m and $V_f = 0.05$ m/s).

Table 1
Comparison between analytical and numerical result for the first period of the oscillating plate at $L = 0.2$ m and $H = 0.02$ m for various V_f.

V_f	0.001	0.01	0.03	0.05
T_{SPH}	0.284	0.283	0.284	0.285
$T_{analytical}$	0.254	0.252	0.254	0.254

Table 2
Comparison between analytical and numerical result for the first period of the oscillating plate at $L = 0.2$ m and $H = 0.01$ m for various V_f.

V_f	0.001	0.01	0.03	0.05
T_{SPH}	0.521	0.520	0.522	0.520
$T_{analytical}$	0.508	0.508	0.508	0.508

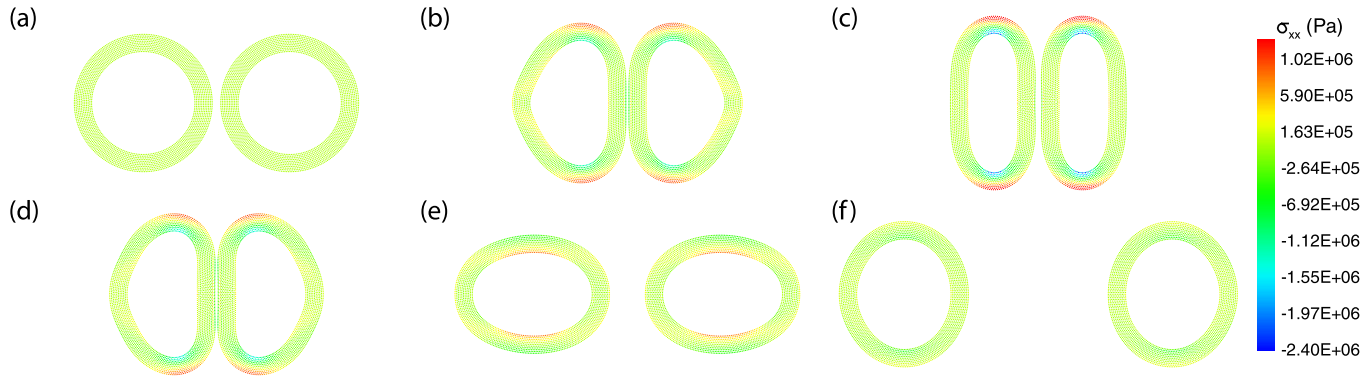

Fig. 6. Collision of rubber rings with $\nu = 0.3975$ using the present method and particles are colored by σ_{xx} stress field: (a) $t = 0.0$ s, (b) $t = 0.02$ s, (c) $t = 0.05$ s, (d) $t = 0.07$ s, (e) $t = 0.12$ s, (f) $t = 0.15$ s.

as shown in Fig. 7, exhibit no structure fragmentation. Note that Lobovsky and Kren [13] point out that the method of Grey et al. [11] produces "numerical fracture" for this case if the same parameters as for the case with $\nu = 0.3975$ are used.

Furthermore, a challenging case with Poisson ratio $\lambda = 0.49$, i.e. the value of real rubber, is simulated. The results, as shown in Fig. 8, indicate that no "numerical fracture" is produced. Note that, we have run this case with an even larger

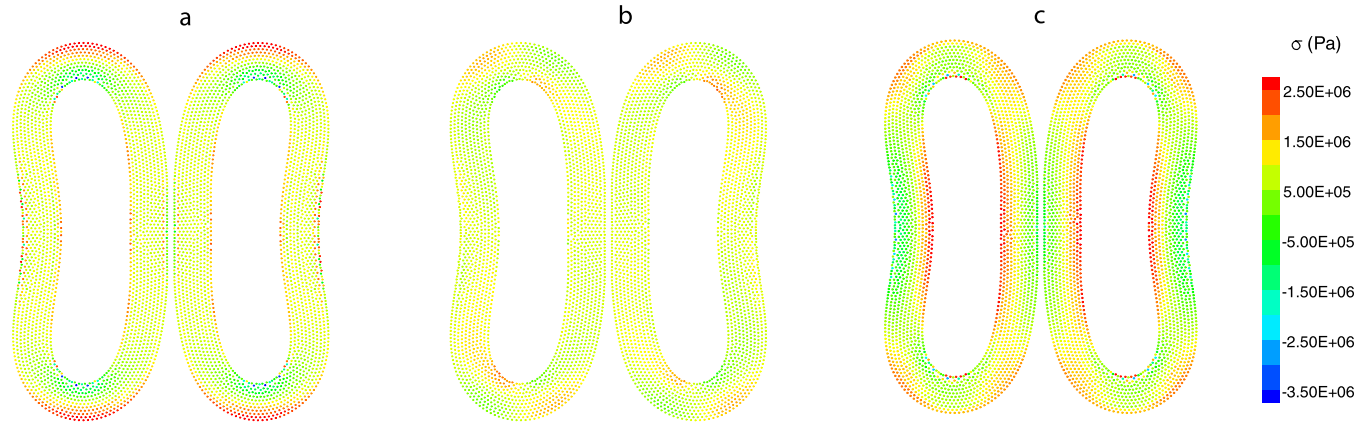

Fig. 7. Collision of rubber rings with $\nu = 0.47$ using the present method and stress field profile: (a) σ_{xx}, (b), σ_{xy}, (c) σ_{yy}.

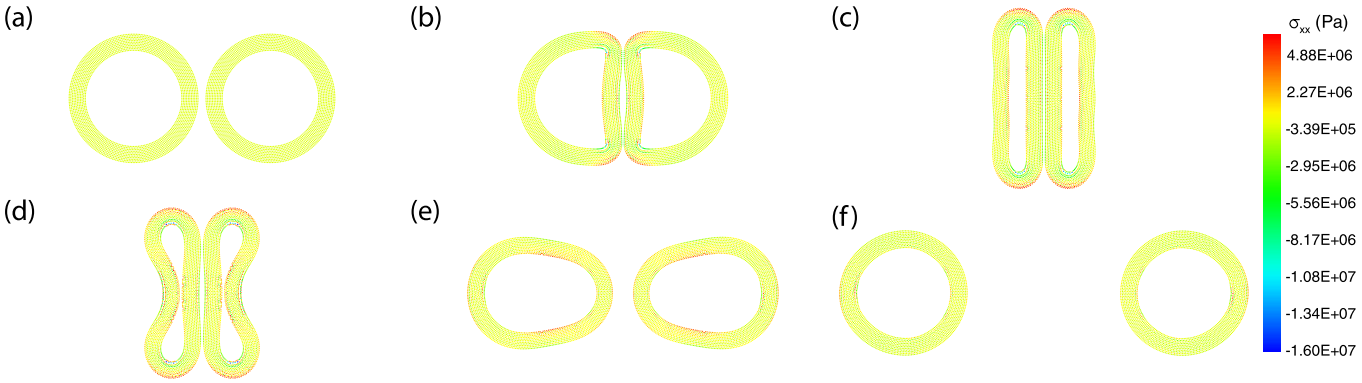

Fig. 8. Collision of rubber rings with $\nu = 0.49$ using the present method and particles are colored by σ_{xx} stress field: (a) $t = 0.0$ s, (b) $t = 0.03$ s, (c) $t = 0.12$ s, (d) $t = 0.19$ s, (e) $t = 0.25$ s, (f) $t = 0.34$ s.

Poisson ratio $\lambda = 0.499$ to demonstrate numerical stability. As the results do not exhibit visible difference from those at $\lambda = 0.49$ we refrain from showing them additionally.

4.3. Interaction involving realistic rubber material

Here, we consider another interesting problem, a low-velocity ball impact on a rubber target. Again, our aim here is to show that, with the present method, the "numerical fragmentation" does not occur. To simulate this problem in 2D, the ball is represented by a circular object with radius $r = 5$ mm and the target is modeled by a rubber filament with two ends fixed and has size of 2×50 mm, as shown in Fig. 9 (a). Ball and target have the same material property, Young's modulus $E = 0.01$ GPa, density $\rho = 1.2 \times 10^3$ kg/m^3 and Poisson ratio $\nu = 0.49$. In this simulation, the initial velocity of the ball is set as $v_0 = 0.15c_0$, and the initial particle spacing is $\Delta x = 0.5$ mm.

Fig. 9 shows the process of the impact. As expected, the target experiences a significant tensile deformation during the impact and then rebounds the ball as the elastic force increases. During the impact a wave propagating from the impact point can be observed and results in a bow-shaped deformation, as shown in Fig. 9 (b), (d). The simulation reproduces the complex impact dynamics, and tensile instability is completely eliminated. To our knowledge, this is the first successful SPH simulation of ball-target impact involving realistic rubber materials.

4.4. High-velocity impact (HVI)

High-velocity impact on a structure is a challenge for spacecraft design [32,33]. The HVI problem results in large deformation of structures [34,35], thus a robust and accurate numerical method is required for prediction.

Here, we consider a high-velocity aluminum projectile impacting on a thin target of the same material. The computational domain is shown in Fig. 10. The projectile is 10 mm in diameter, and the rectangular target has a size of 2×50 mm. The projectile and the target both have the following material properties: density $\rho = 2785$ kg/m^3, sound speed $c_0 = 5328$ m/s, shear modulus $G = 2.76 \times 10^7$ kPa, yield modulus $Y_0 = 3.0 \times 10^5$ kPa. The impact velocity is set as $V_0 = 3100.0$ m/s. The initial particle spacing is $\Delta x = 0.5$ mm, and the simulation is started at the moment of impact. By using an elastic-perfectly plastic constitutive model [36,37], the deviatoric stress $\boldsymbol{\sigma}'$ in Eq. (10) is bounded by a factor

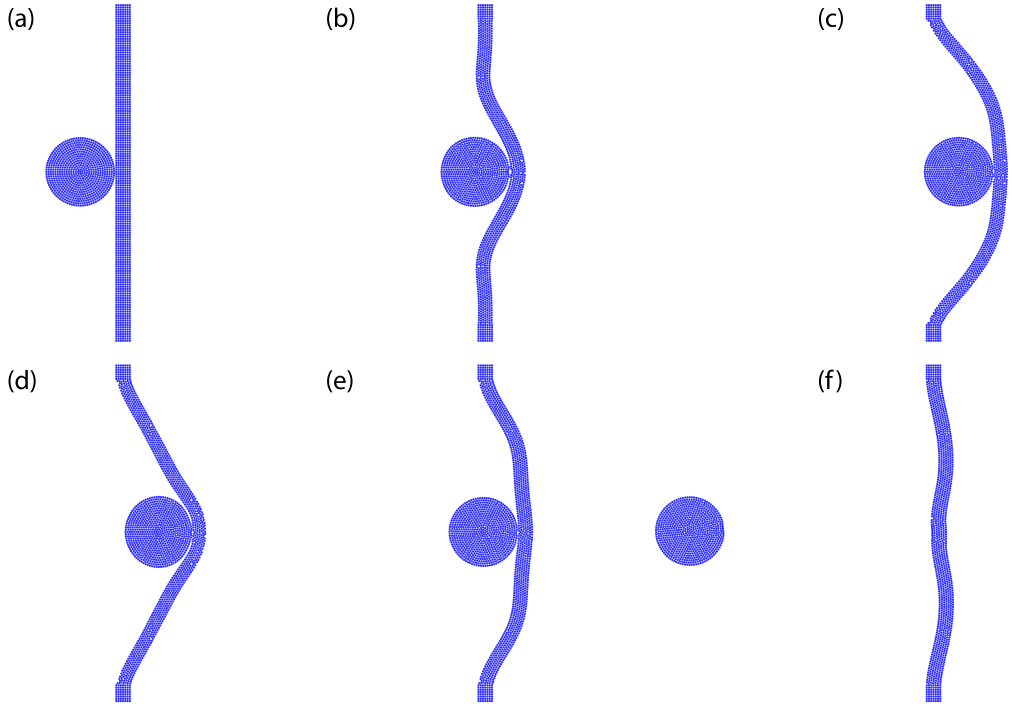

Fig. 9. Rubber projectile impact on target using the present method: (a) $t = 0.0$ ms, (b) $t = 0.33$ ms, (c) $t = 0.88$ ms, (d) $t = 1.20$ ms, (e) $t = 1.88$ ms, (f) $t = 4.08$ ms.

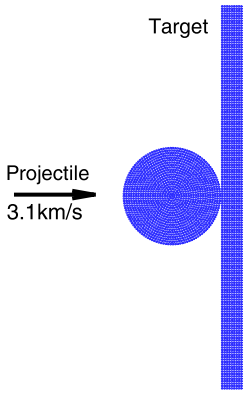

Fig. 10. Computational domain of the high velocity impact problem.

$\alpha = min(\frac{Y_0^2}{3J_2}, 1)$, where J_2 is calculated from $J_2 = \frac{1}{2}\boldsymbol{\sigma}' : \boldsymbol{\sigma}'$. As the pressure generated by the high-velocity impacting is much larger than the yield stress of aluminum, a highly localized plastic deformation is expected.

Fig. 11 shows the material geometry at several time instances after initial impact as predicted by the present method. As expected, the strong compression generated by the impact produces extreme pressures. A shock wave of about 1.0×10^7 kPa is observed to travel leftward to the projectile, closely followed by a rarefaction formed at the rear face of the target. As consequence, a large tensile force is produced. While the tensile force can lead to "numerical fracture" for the standard SPH method due to tensile instability [38,39] the present method does not produce such an artifact. Also note that, although using a much simpler material model, the target deformation is in qualitative agreement with previous SPH and free-Lagrangian simulations [38]. Furthermore, the progress of the projectile through the target, about 20.9 mm, and the width of the hole, about 19.8 mm, at $t = 8$ μs are also close to those obtained by Ref. [38], as the evolution is dominated by inertial effects and much less effected by details of the material model [38].

4.5. Circular patch

We consider the evolution of a circular patch of an inviscid fluid with a nonuniform initial vorticity distribution. A very similar case has been studied by Antuono et al. [40]. The configuration is considered as a circular cylinder with radius $R = 1$ rotating with an angular velocity $\omega = \omega(r)$ as shown in Fig. 12 (a). The circular patch is subjected to a radial force given by $\mathbf{g} = -\beta^2 r\mathbf{r}$ where β is a constant parameter, r is the radial coordinate and $\mathbf{r}$ is the radial unit vector. The initial profiles of angular velocity and pressure are given by

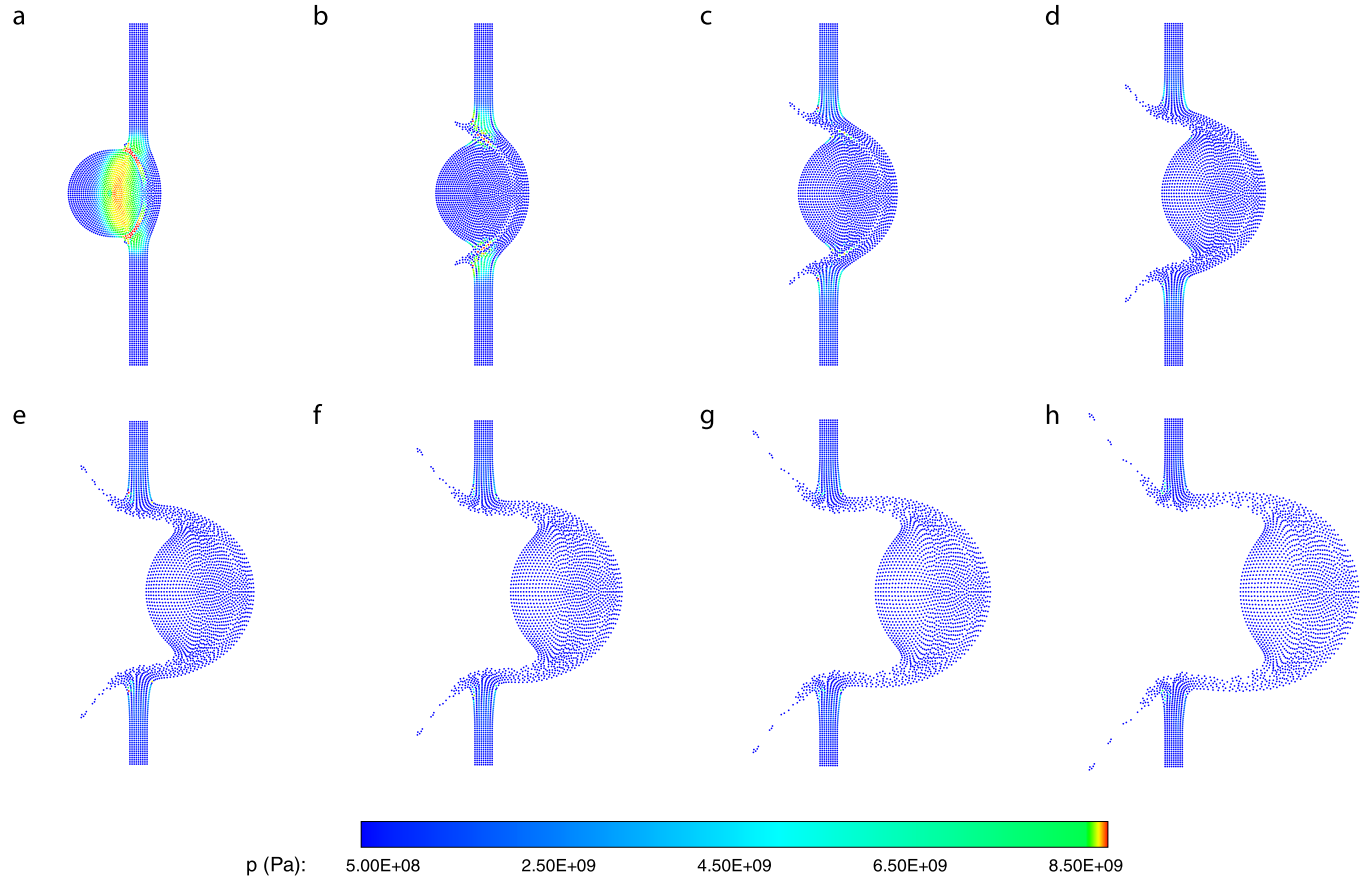

Fig. 11. Instantaneous results illustrating the deformation of structures in a HVI problem simulated by the present method: (a) $t = 1$ μs, (b) $t = 2$ μs, (c) $t = 3$ μs, (d) $t = 4$ μs, (e) $t = 5$ μs, (f) $t = 6$ μs, (g) $t = 7$ μs, (h) $t = 8$ μs.

$$\begin{cases} r\omega^2(r,0) = \frac{1}{\rho_0}\frac{\partial p}{\partial r} + \beta^2 r \\ \omega(r,0) = \omega_0\left\{\frac{l^2}{l^2+r^2} + 2\frac{l^2 R}{(l^2+R^2)^2}r\right\}. \end{cases} \tag{36}$$

The constant parameters are $l^2 = 0.2$ m^2, $\omega_0 = 1$ s^{-1} and $\beta = \frac{\pi}{8}$ s^{-1}, and the computational setup follows Ref. [40].

Fig. 12 shows the numerical results obtained with the present method and with standard SPH with and without artificial viscosity. While the present method and the standard SPH without artificial viscosity dissipate less kinetic energy, $\sum \frac{1}{2}v_i^2$, at the early times, the standard SPH with artificial viscosity dissipates less kinetic energy at longer times, as shown Fig. 12 (b). This may be related to the fact that artificial viscosity supports solid-body rotation behavior. The kinetic energy decays obtained by the present method with and without the extra-stress term **A**, as shown in Fig. 12 (b), differ only slightly.

Fig. 12 (c) gives the evolution of the angular momentum obtained by different methods. Standard SPH with or without artificial viscosity conserves the angular momentum while the present method loses conservation because particles move with the transport velocity other than the momentum velocity. However, the conservation errors are very small as shown in Fig. 12 (c).

Fig. 12 (d) gives the evolution of circulation along the ring $r = 0.5$ and the circulation Γ is calculated through $\Gamma = 0.5\sum \mathbf{v}_i \cdot (\mathbf{x}_{i+1} - \mathbf{x}_{i-1})$, where i denotes the label of a particle on the ring and $\mathbf{x}_{i-1}$, and $\mathbf{x}_{i+1}$ represent the positions of the two nearest particles on the same ring. It is observed that the present method and the standard SPH with artificial viscosity conserve circulation better than the latter without artificial viscosity. None of the three methods conserves the circulation exactly. As particles move with the transport velocity in the present method one may rather approximate the circulation as $\Gamma_{tv} = 0.5\sum \tilde{\mathbf{v}}_i \cdot (\mathbf{x}_{i+1} - \mathbf{x}_{i-1})$, which is damped considerably less compared with the circulation obtained by momentum velocity. Note that more demanding tests are also discussed in Antuono et al. [40], and further investigation of the circulation conservation of the present method with such tests is subject of future work.

4.6. Dam-break problem

The dam-break problem is taken from Ref. [41]. A liquid column of height $H = 1$ and length $L = 2H$ is located at the left side of a tank which has a length $l = 5.366H$ and height $h = 2H$. The liquid has a density $\rho = 1$ and the gravity is set as $g = 1$. A wall boundary condition proposed by Adami et al. [41] is implemented.

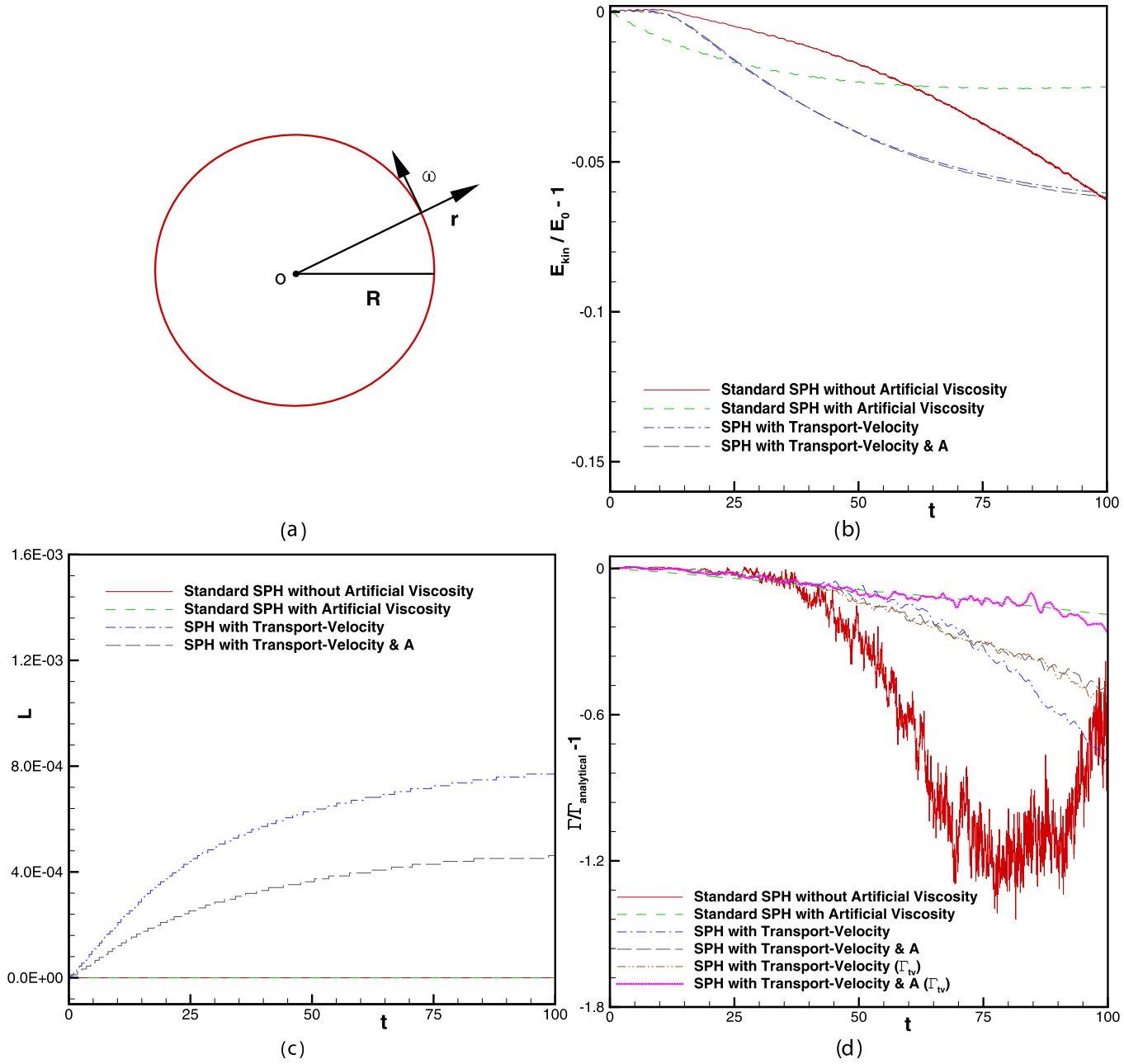

Fig. 12. Evolution of a circular patch of an inviscid fluid: (a) Configuration of circular patch; (b) Evolution of kinetic energy; (c) Evolution of angular momentum; (d) Evolution of circulation.

We consider the liquid as viscous and inviscid, respectively. For viscous flow the Reynolds number is set as $Re = \frac{U_{max}H}{\nu} = 400$, where $U_{max} = 2\sqrt{gH}$, reproducing the same case as in Adami et al. [41]. If the liquid is considered as inviscid this problem is very challenging, and the standard SPH requires artificial viscosity or diffusion to stabilize the simulation. The problem was simulated previously by Colagrossi and Landrini [24] with several stabilization approaches, such as moving-least-square density re-normalization, artificial viscosity and the XSPH method for transporting particles [18].

Fig. 13 (a) presents snapshots of the particle distribution and pressure profiles at different time instances for the viscous flow. Note that these results are in good agreement with those (their Fig. 14) of Adami et al. [41]. Quite similar run-up along the downstream wall after impact and reflected jet following the re-entry of backward wave can be observed in both simulations. Fig. 13 (b) shows the evolution of the particle distribution for the inviscid flow. The enlarged views of the fluid particles at $t = 6.2$, as shown in Fig. 14, suggest very regular pressure distribution is obtained by both viscid and inviscid simulations. It can be observed that the present results for the inviscid flow share several typical features with those in Ref. [24], such as a high run-up along the downstream wall, a large reflected jet and a large void in the downstream flow due to the re-entry of backward wave. A different feature obtained for the inviscid flow by the present method is the more intense splashing which agrees with experimental observations, such as in Lobovsky et al. [42] and other simulations such as that of Ferrari et al. [43].

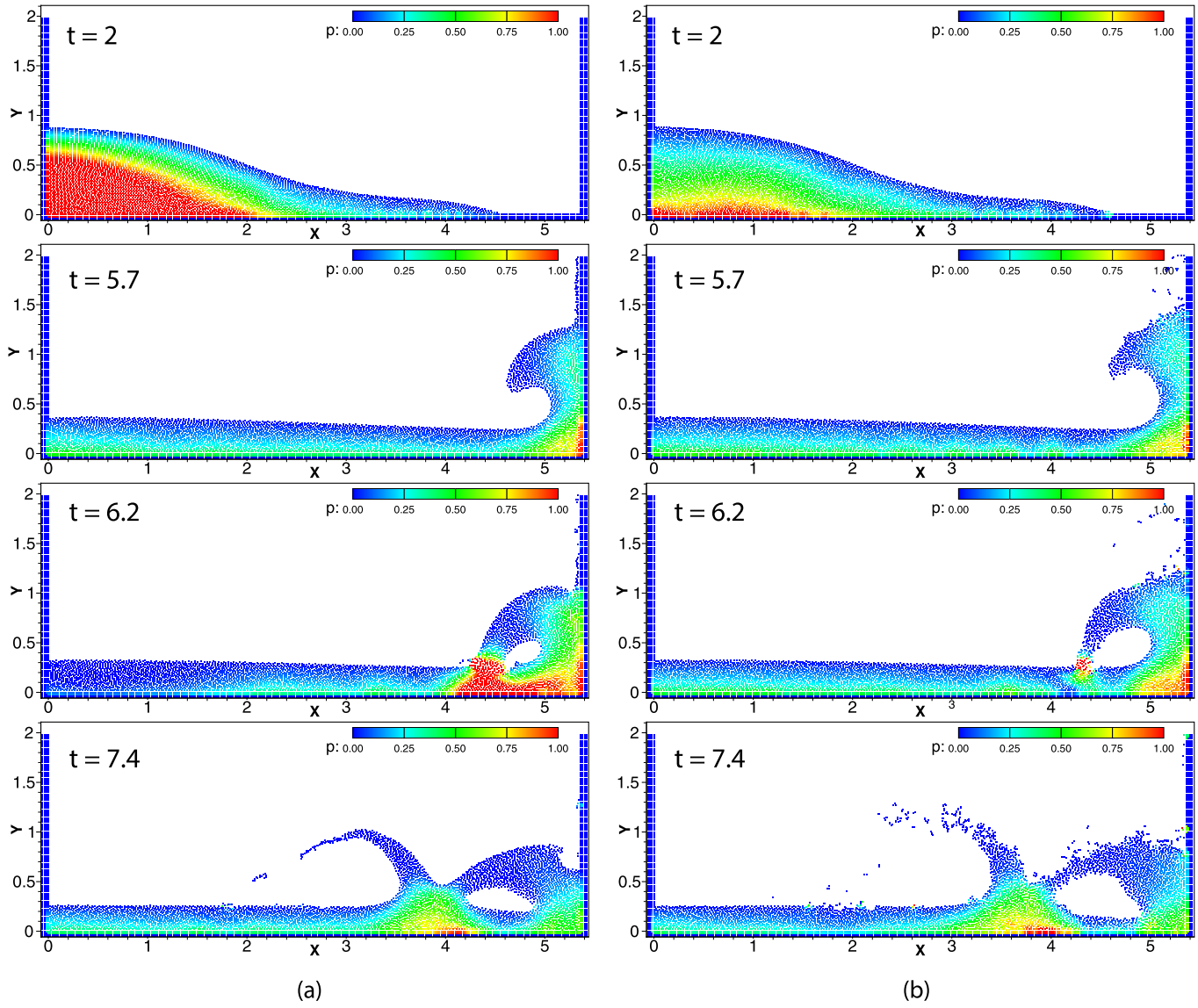

Fig. 13. Several snapshots of the particle distribution and pressure profile (colored by the pressure field) in the simulation of the dam-break problem with 5000 fluid particles: (a) Viscous flow solution; (b) Inviscid flow solution.

Fig. 15 (a) shows the water front location compared with experimental data [44,45] and theoretical result [46]. The inviscid solution, while overestimating the velocity of the liquid-front obtained from experiment, converges to the theoretical result. The viscous solution, similar to that of Adami et al. [41], achieves a better agreement with the experiment. We should point out that the present Reynolds number is much smaller than that (estimated as 5×10^5) in the experiment. Fig. 15 (b) shows the pressure profile on the right wall at $y_0 = 0.2H$ obtained from both the inviscid and viscous solutions. Note that the probe position is the same as in Adami et al. [41] and Greco [47], not exact match the setup as in experiment. Similarly to Adami et al. [41] and Greco [47], the jump is well predicted and the numerical impact peak (around $t = 6.5$) is slightly delayed due to the fact that the air cushion is not considered here. Note that, compared with the viscid simulation, the inviscid simulation shows strong pressure fluctuations, e.g. spikes during the flow impact at the downstream wall.

4.7. Taylor–Green vortex

The 2D viscous Taylor–Green vortex flow has been simulated by SPH with the original transport-velocity formulation. As the standard SPH method leads to over-dissipation in simulation of Taylor–Green flow problems, and the original transport-velocity formulation solved this difficulty, we show that the present method recovers the original formulation for flows without free surface. Taylor–Green flow is a periodic array of vortices with the velocity of analytical solution given by

$$u(x, y, t) = -Ue^{bt}cos(2\pi x)sin(2\pi y),$$
$$v(x, y, t) = Ue^{bt}sin(2\pi x)cos(2\pi y), \tag{37}$$

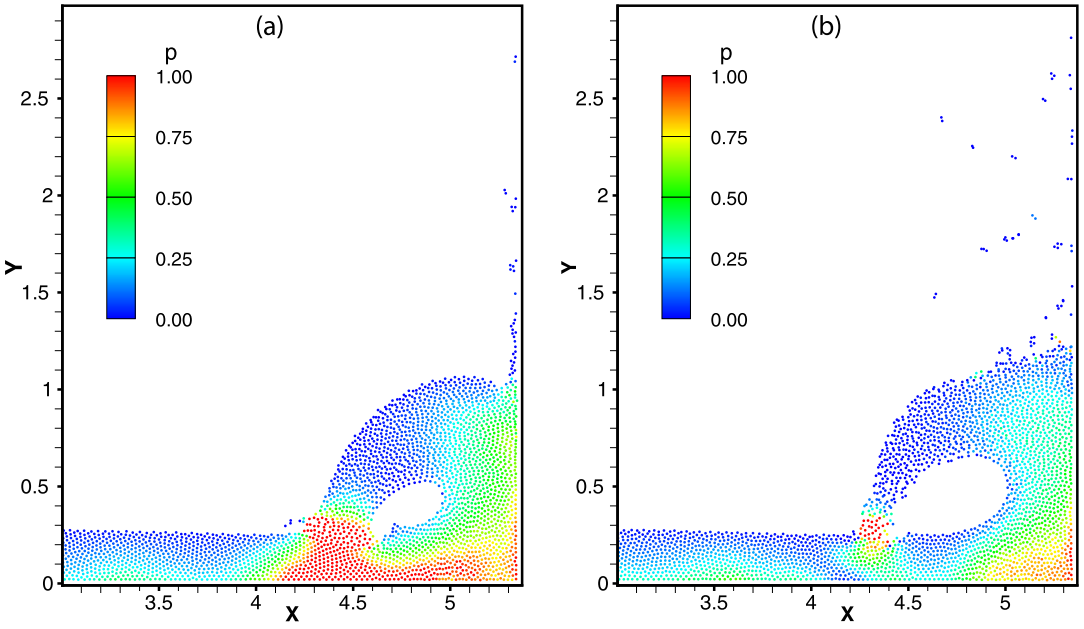

Fig. 14. Enlarged view of the impact of dam break flow at $t = 6.2$: (a) Viscous flow solution; (b) Inviscid flow solution.

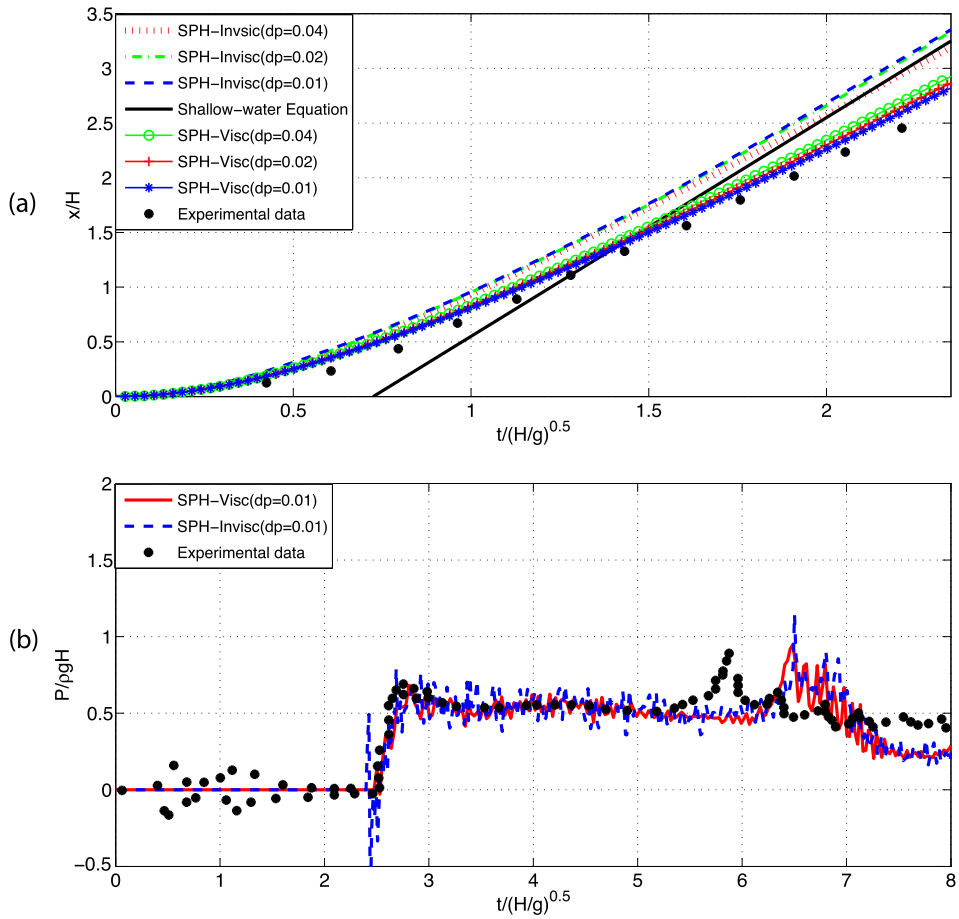

Fig. 15. Results for the dam-break problem: (a) Time evolution of the liquid-front from inviscid and viscous solutions compared with theoretical and experimental data [44]; (b) Comparison of pressure profile between numerical simulations and experimental data [45].

where $b = -8\pi^2/R_e$ is the decay rate of the velocity field, U is the maximum velocity, R_e is the Reynolds number and here we set $R_e = 100$ corresponding to the work of Adami et al. [14].

In this simulation, the computation is performed on a square domain with unit length $L = 1$, and a periodic boundary condition is applied in both coordinate directions. The initial velocity distribution is given by setting $t = 0$ and $U = 1$. The

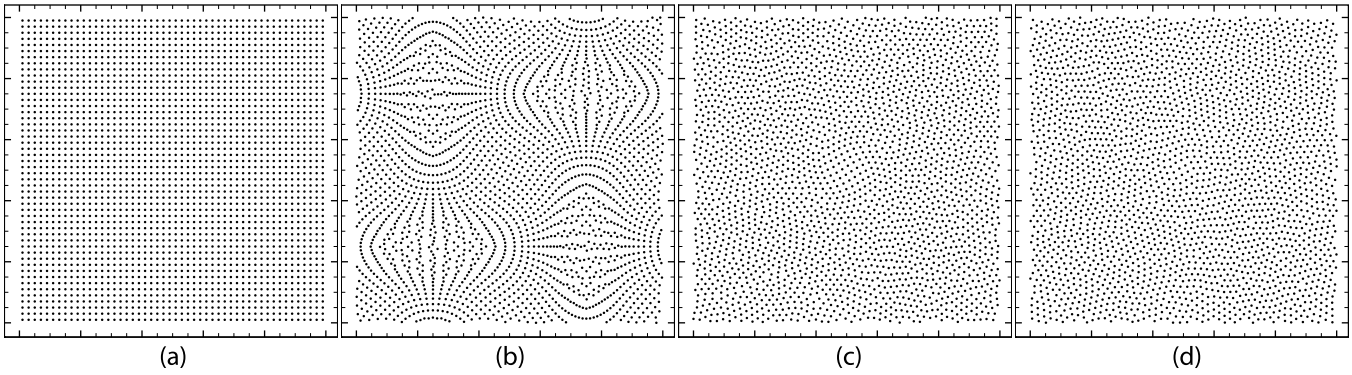

Fig. 16. Particle snapshots for the Taylor–Green problem at $R_e = 100$ with a resolution of 50×50 particles: (a) $t = 0.0$ s, (b) $t = 0.2$ s, (c) $t = 0.4$, (d) $t = 0.8$ s.

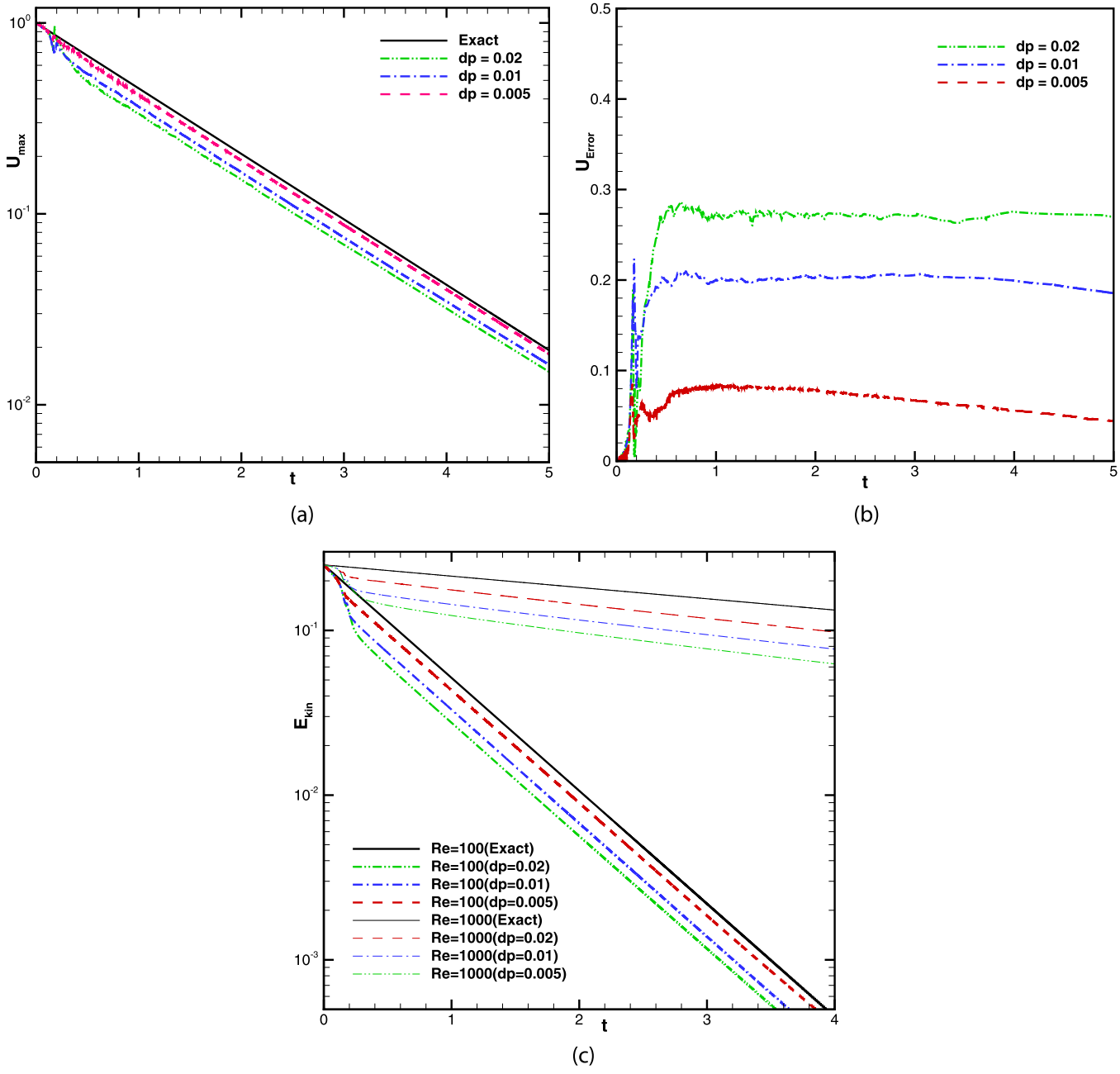

Fig. 17. Numerical results of the Taylor–Green problem: (a) Decay of the maximum velocity ($R_e = 100$); (b) Relative error of the maximum velocity ($R_e = 100$); (c) Decay of the kinetic energy ($R_e = 100$ and $R_e = 1000$).

convergence study is performed by three different resolutions, $\Delta x = 0.02$ (50×50 particles), $\Delta x = 0.01$ (100×100 particles) and $\Delta x = 0.005$ (200×200 particles).

The particle distributions at several time instants with a resolution of 50×50 particles are shown in Fig. 16. It can be observed that a homogeneous particle distribution without clustering is produced. As the simulation starts from a regular lattice particle distribution, particles assume a relaxed configuration at $t = 0.2$ s, as also observed in Adami et al. [14].

Figs. 17 (a) and 17 (c) give the time evolution of the maximum velocity and the total kinetic energy with three resolutions and the analytical solutions. Fig. 17 (b) shows the relative error defined by $L_\infty = |\frac{\max(\mathbf{v_i}(t) - Ue^{bt})}{Ue^{bt}}|$. It can be observed that these results are in quite good agreement with that (see their Fig. 5) obtained by the original transport-velocity formulation [14]. Figs. 17 (c) also gives the evolution of the total kinetic energy for the flow with $Re = 1000$ suggesting correct decay rate with increasing resolution.

5. Conclusions

While many approaches have been proposed to address the well-known tensile instability of the SPH method, none of them is generally effective. In this work, we propose such a method as simple generalization of the previously proposed transport-velocity formulation. The generalization leads to transport-velocity correction which is proportional to the magnitude of the particle pressure, and a restriction of the correction so that it is only affected by the nearest neighbors. By reproducing the simulation of the Taylor–Green vortex, the present method preserves the accuracy of the original transport-velocity formulation. Furthermore, numerical results for a range of fluid and solid dynamics problems show that the present method generally eliminates the tensile instability. Generality and stability of the present method suggest that it has the potential to supersede current standard SPH.

Acknowledgement

The first author is partially supported by China Scholarship Council (No. 2011623002).

References

[1] L.B. Lucy, A numerical approach to the testing of the fission hypothesis, Astron. J. 82 (1977) 1013–1024.
[2] R.A. Gingold, J.J. Monaghan, Smoothed particle hydrodynamics: theory and application to non-spherical stars, Mon. Not. R. Astron. Soc. 181 (3) (1977) 375–389.
[3] J.W. Swegle, D.L. Hicks, S.W. Attaway, Smoothed particle hydrodynamics stability analysis, J. Comput. Phys. 116 (1) (1995) 123–134.
[4] I. Schuessler, D. Schmitt, Comments on smoothed particle hydrodynamics, Astron. Astrophys. 97 (1981) 373–379.
[5] G.R. Johnson, S.R. Beissel, Normalized smoothing functions for SPH impact computations, Int. J. Numer. Methods Eng. 39 (16) (1996) 2725–2741.
[6] P.W. Randles, L.D. Libersky, Smoothed particle hydrodynamics: some recent improvements and applications, Comput. Methods Appl. Mech. Eng. 139 (1) (1996) 375–408.
[7] D.A. Mandell, C.A. Wingate, L.A. Schwalbe, Computational Brittle Fracture Using Smooth Particle Hydrodynamics, Tech. Rep., Los Alamos National Lab., NM, United States, 1996.
[8] G.A. Dilts, Moving-least-squares-particle hydrodynamics—I. Consistency and stability, Int. J. Numer. Methods Eng. 44 (8) (1999) 1115–1155.
[9] C.T. Dyka, P.W. Randles, R.P. Ingel, Stress points for tension instability in SPH, Int. J. Numer. Methods Eng. 40 (13) (1997) 2325–2341.
[10] P.W. Randles, L.D. Libersky, Normalized SPH with stress points, Int. J. Numer. Methods Eng. 48 (10) (2000) 1445–1462.
[11] J.P. Gray, J.J. Monaghan, R.P. Swift, SPH elastic dynamics, Comput. Methods Appl. Mech. Eng. 190 (49) (2001) 6641–6662.
[12] J.J. Monaghan, SPH without a tensile instability, J. Comput. Phys. 159 (2) (2000) 290–311.
[13] L. Lobovskỳ, J. Křen, Smoothed particle hydrodynamics modelling of fluids and solids, Appl. Comput. Mech. 1 (49) (2007) 521–530.
[14] S. Adami, X.Y. Hu, N.A. Adams, A transport-velocity formulation for smoothed particle hydrodynamics, J. Comput. Phys. 241 (2013) 292–307.
[15] X.Y. Hu, N.A. Adams, An incompressible multi-phase SPH method, J. Comput. Phys. 227 (1) (2007) 264–278.
[16] X. Hu, N. Adams, A SPH model for incompressible turbulence, Proc. IUTAM 18 (2015) 66–75.
[17] S. Litvinov, X.Y. Hu, N.A. Adams, Towards consistence and convergence of conservative SPH approximations, J. Comput. Phys. 301 (2015) 394–401.
[18] J. Monaghan, On the problem of penetration in particle methods, J. Comput. Phys. 82 (1) (1989) 1–15.
[19] R. Xu, P. Stansby, D. Laurence, Accuracy and stability in incompressible sph (isph) based on the projection method and a new approach, J. Comput. Phys. 228 (18) (2009) 6703–6725.
[20] S. Lind, R. Xu, P. Stansby, B. Rogers, Incompressible smoothed particle hydrodynamics for free-surface flows: a generalised diffusion-based algorithm for stability and validations for impulsive flows and propagating waves, J. Comput. Phys. 231 (4) (2012) 1499–1523.
[21] R. Vacondio, B. Rogers, P. Stansby, P. Mignosa, J. Feldman, Variable resolution for sph: a dynamic particle coalescing and splitting scheme, Comput. Methods Appl. Mech. Eng. 256 (2013) 132–148.
[22] J. Monaghan, A turbulence model for smoothed particle hydrodynamics, Eur. J. Mech. B, Fluids 30 (4) (2011) 360–370.
[23] D.D. Holm, Fluctuation effects on 3d lagrangian mean and eulerian mean fluid motion, Physica D 133 (1) (1999) 215–269.
[24] A. Colagrossi, M. Landrini, Numerical simulation of interfacial flows by smoothed particle hydrodynamics, J. Comput. Phys. 191 (2) (2003) 448–475.
[25] W. Benz, E. Asphaug, Impact simulations with fracture. i. method and tests, Icarus 107 (1) (1994) 98–116.
[26] W. Benz, E. Asphaug, Simulations of brittle solids using smooth particle hydrodynamics, Comput. Phys. Commun. 87 (1) (1995) 253–265.
[27] J.P. Morris, P.J. Fox, Y. Zhu, Modeling low Reynolds number incompressible flows using SPH, J. Comput. Phys. 136 (1) (1997) 214–226.
[28] J.J. Monaghan, Simulating free surface flows with SPH, J. Comput. Phys. 110 (2) (1994) 399–406.
[29] J.J. Monaghan, Smoothed particle hydrodynamics, Rep. Prog. Phys. 68 (8) (2005) 1703.
[30] H. Wendland, Piecewise polynomial, positive definite and compactly supported radial functions of minimal degree, Adv. Comput. Math. 4 (1) (1995) 389–396.
[31] L.D. Landau, E.M. Lifchits, Course of Theoretical Physics: Theory of Elasticity, Butterworth–Heinemann, 1986.
[32] A.J. Piekutowski, Effects of scale on debris cloud properties, Int. J. Impact Eng. 20 (6) (1997) 639–650.

[33] A.J. Piekutowski, M.J. Forrestal, K.L. Poormon, T.L. Warren, Penetration of 6061-t6511 aluminum targets by ogive-nose steel projectiles with striking velocities between 0.5 and 3.0 km/s, Int. J. Impact Eng. 23 (1) (1999) 723–734.
[34] H.F. Swift, Hypervelocity impact mechanics, in: Impact Dynamics, 1982, pp. 215–239.
[35] J.A. Zukas, High Velocity Impact Dynamics, Wiley–Interscience, 1990.
[36] M.L. Wilkins, Calculation of Elastic–Plastic Flow, Tech. rep., DTIC Document, 1963.
[37] L.D. Libersky, A.G. Petschek, Smooth particle hydrodynamics with strength of materials, in: Advances in the Free-Lagrange Method Including Contributions on Adaptive Gridding and the Smooth Particle Hydrodynamics Method, Springer, 1991, pp. 248–257.
[38] B. Howell, G. Ball, A free-Lagrange augmented Godunov method for the simulation of elastic–plastic solids, J. Comput. Phys. 175 (1) (2002) 128–167.
[39] V. Mehra, S. Chaturvedi, High velocity impact of metal sphere on thin metallic plates: a comparative smooth particle hydrodynamics study, J. Comput. Phys. 212 (1) (2006) 318–337.
[40] M. Antuono, A. Colagrossi, D. Le Touzé, J. Monaghan, Conservation of circulation in SPH for 2D free-surface flows, Int. J. Numer. Methods Fluids 72 (5) (2013) 583–606.
[41] S. Adami, X. Hu, N. Adams, A generalized wall boundary condition for smoothed particle hydrodynamics, J. Comput. Phys. 231 (21) (2012) 7057–7075.
[42] L. Lobovskỳ, E. Botia-Vera, F. Castellana, J. Mas-Soler, A. Souto-Iglesias, Experimental investigation of dynamic pressure loads during dam break, J. Fluids Struct. 48 (2014) 407–434.
[43] A. Ferrari, M. Dumbser, E.F. Toro, A. Armanini, A new 3d parallel SPH scheme for free surface flows, Comput. Fluids 38 (6) (2009) 1203–1217.
[44] J.C. Martin, W.J. Moyce, Part IV. An experimental study of the collapse of liquid columns on a rigid horizontal plane, Philos. Trans. R. Soc. Lond. Ser. A, Math. Phys. Sci. 244 (882) (1952) 312–324.
[45] B. Buchner, Green Water on Ship-Type Offshore Structures, PhD thesis, TU Delft, Delft University of Technology, 2002.
[46] A. Ritter, Die fortpflanzung de wasserwellen, Z. Ver. Dtsch. Ing. 36 (33) (1892) 947–954.
[47] M. Greco, A two-dimensional study of green-water loading.